Leptonic Two-Photon Events Measured with L3 at the Large Electron Positron Collider (LEP)

by
Klaus Dehmelt

Diplom-Physiker
University of Hamburg, Germany
1999

A dissertation
submitted to
Florida Institute of Technology
in partial fulfillment of the requirements
for the degree of

Doctor of Philosophy
in
Physics

Melbourne, Florida
December 2006

© Copyright 2006 Klaus Dehmelt
All Rights Reserved

The author grants permission to make single copies

We the undersigned committee hereby recommends that the attached document be accepted as fulfilling in part the requirements for the degree of Doctor of Philosophy in Physics.

"Leptonic Two-Photon Events Measured with L3 at the Large Electron Positron Collider (LEP)"
A Dissertation by Klaus Dehmelt

Laszlo A. Baksay, Dr. rer. nat.
Professor
Physics and Space Sciences
Major Advisor

Marcus Hohlmann, Ph.D.
Assistant Professor
Physics and Space Sciences
Committee Member

Fredric M. Ham, Ph.D., P.E.
Harris Professor
Electrical and Computer Engineering
Committee Member

James G. Mantovani, Ph.D.
Adjunct Professor
Physics and Space Sciences
Committee Member

Gabor David, Ph.D.
Senior Physicist
Brookhaven National Laboratory, Upton, NY
Committee Member

Hamid K. Rassoul, Ph.D.
Professor
Physics and Space Sciences
Committee Member

Terry D. Oswalt, Ph.D.
Professor
Physics and Space Sciences
Department Head

ABSTRACT

Leptonic Two-Photon Events Measured with L3 at the Large Electron Positron Collider (LEP)

by

Klaus Dehmelt

Dissertation Advisor: Laszlo A. Baksay, Dr. rer. nat.

Virtual photons can fluctuate into diverse final states and among other processes, such fluctuations can yield muon-pairs. The fluctuation is a statistical process and can be described in terms of structure functions for photons. Apart from supplying another test of QED, purely leptonic processes provide a calibration for the hadronic processes. We report on a measurement of dimuon events with single-tagged two-photon events from the LEP experiment L3, at c.m.s. energies between 189 GeV and 206 GeV, with an integrated luminosity of $\mathcal{L} = 600\ \mathrm{pb}^{-1}$. An overview of the fundamental physical processes, the detector and the analytical tools, used for measuring dimuon events, and a discussion of the structure of dimuon events will be presented.

Acknowledgements

I would like to express my gratitude to my advisor, Professor Laszlo Baksay. He was giving me the opportunity to work on a research topic that is very exciting and challenging in equal measure. I would also like to thank him for giving me all the support and advice which was necessary to make this work a success.

This work was based on data taken with the L3 experiment at the Large Electron Positron Collider LEP at CERN/Switzerland. The analysis was performed at Florida Tech and CERN. I would like to thank the L3 collaboration for the fine work of data collection and processing which allowed me performing this analysis. In particular, I would like to thank Professor Maria Kienzle from the University of Geneva, who is the leader of the Two-Gamma Analysis group of L3. She gave me all needed advice, both, for physics and technical aspects. The discussions with her were crucial to successfully perform this analysis.

Many thanks also to Professor John Field from the University of Geneva who gave me deep insight in the theoretical description of Two-Gamma physics.

I would like to thank Professor Marcus Hohlmann from Florida Tech for his sedulous dedication for all kind of questions which were arising from this analysis.

I would like to thank my committee members, Dr. Gabor David, Professor Fredric Ham, Professor James Mantovani, and Professor Hamid Rassoul for their commitment and the work they spent.

Thank you to the Florida Institute of Technology which gave me the opportunity to perform my graduate studies.

Contents

1 Introduction **1**

2 Two-Photon Physics **6**

2.1 Quantum-Electrodynamics: Introduction 6

2.2 QED in Two-Photon Processes 10

2.3 Two-Photon Scattering, Cross-Section 12

2.3.1 Two-Photon Scattering 12

2.3.2 Cross-Section, Theoretical Framework 17

2.3.3 Lepton Pair Production in Single Tag Configuration . . . 22

2.4 Structure Functions 26

2.4.1 The Differential Cross-Section 27

2.4.2 The Structure Function F_2^γ 28

3 Monte Carlo Techniques **31**

3.1 The Vermaseren Generator 35
3.2 The BDK Generator: DIAG36 36
3.3 Radiative Corrections with RADCOR 37
3.4 VEGAS 38
3.5 L3 Detector Simulation: `GEANT, GEISHA` 39

4 The Large Electron Positron Collider (LEP) 42

5 The LEP experiment L3 47

5.1 The Central Tracking Detector 52
5.1.1 Silicon Microvertex Detector SMD 52
5.1.2 Time Expansion Chamber TEC 53
5.2 Electromagnetic Calorimeter BGO 58
5.3 Scintillator Counter 59
5.4 Hadronic Calorimeter HCAL 60
5.5 Very Small Angle Tagger VSAT 62
5.6 Luminosity Monitor LUMI 63
5.7 The Trigger System 66

6 Data Analysis 70

6.1 Event Selection 75
6.1.1 VSAT Selections, Single Tag Events 76

6.1.2 Dimuon Events 78
6.2 Trigger Efficiency 91
6.3 Background in Selected Events 98
6.4 Radiative Corrections 103
6.5 Systematic Error Estimation 110
6.6 Summary 117

7 Results **122**

7.1 The Differential Cross-Section $d\sigma/dQ^2$ 123
7.2 The Structure Function F_2^γ 128

8 Conclusion **134**

List of Figures

1.1 Quantum fluctuation of a photon into pairs of charged particles. 2

1.2 Elastic two-photon scattering. 3

1.3 Inelastic $\gamma\gamma$-scattering with production of lepton pairs. 4

2.1 Symbols, which are used in Feynman graphs. 8

2.2 Inelastic $\gamma\gamma$-scattering with production of lepton pairs (left), hadrons (right). 10

2.3 Cross-sections for dominant processes for the various LEP phases [9]. 11

2.4 Two-photon production and scattering [11]. 13

2.5 The helicity states for a single-tag configuration in two-photon collisions. The arrow depict the transverse helicity state, the circle the longitudinal helicity state of the probe photon [9] (see text). 15

2.6 Kinematics for two-photon processes [14]. 17

3.1 Feynman diagrams of $\mathcal{O}(\alpha^4)$, describing $e^+e^- \to e^+e^-l^+l^-$, where l stands for leptons. 34

3.2 (a,b) Self-energy and vertex diagrams. (b,e) Vacuum polarization diagrams. (c,f) Bremsstrahlung diagrams [27]. 41

4.1 Schematic sketch of the LEP accelerator [9]. 45

4.2 Schematic sketch of injection and acceleration processes for LEP [9]. 46

5.1 Perspective view of the L3 detector [9]. 48

5.2 The L3 detector, as seen in the $r - \phi$ plane [9]. 49

5.3 Definition of the polar coordinate system, as used with L3. The x-axis is pointing towards the center of LEP [9]. 51

5.4 The tracking device of L3 [9]. 52

5.5 The silicon microvertex detector [9]. 55

5.6 View in the $r - \phi$ plane of the SMD [9]. 55

5.7 Wire configuration of a TEC cell geometry [9]. 56

5.8 Perspective view of the L3 TEC [9]. 57

5.9 The barrels and endcaps of the L3 BGO in longitudinal cut view [9]. 59

5.10 The BGO crystal with its main components [9]. 60
5.11 Perspective view of the HCAL modules [9]. 61
5.12 Top view of the distribution of the VSAT boxes along the beam-line and its coordinate system [43]. 62
5.13 Vertical cut of the VSAT detector at one side of the vertex point [43]. 63
5.14 VSAT acceptance for charged particles [43]. 64
5.15 Side view of the central region of the L3 experiment on the $+z$ side, showing the beam pipe and the positions of the LUMI and SLUM detector [9]. 65
5.16 Schematic view of the LUMI detector arrangement. Upper: transverse sketch; Lower: longitudinal sketch, showing the LUMI detector around the beampipe with SLUM in front of it [9]. 66

6.1 Schematic sketch of the data flow procedures in L3 [9]. 72
6.2 Cross-sectional view of an event display from L3. The left plot shows energy deposits in the TEC, BGO, and HCAL (from inner to outer), released by a muon. The right plot shows the same, but for a pion [9]. 79

6.3 Correlation between the momentum measured with TEC and deposited energy in the BGO calorimeter. Upper left: for electrons; upper right: for muons; lower: for the data sample, which contains both, electrons and muons. 84
6.4 Ratio of the transverse energy, released in the BGO to the transverse momentum, measured with TEC. 85
6.5 Probability of being an MIP, measured with the HCAL detector. Upper left: for pions; upper right: for muons; lower: superposition of pions and muons, normalized to the generated luminosity. 86
6.6 Acoplanarity angle, measured with VSAT and TEC. 87
6.7 Azimuthal distribution as measured with the VSAT. (a) before selection cuts; (b) selection of $W_{\gamma\gamma} \geq 1.7\,GeV$; (c) selection of $\phi_{aco} \leq 0.5\,rad$. 88
6.8 Polar angular distribution of tracks, measured with TEC. 89
6.9 Polar angular distribution of tracks, after selection cuts. 90
6.10 The contribution of simultaneous trigger hits for recorded events. 95
6.11 The contribution of various trigger combinations for recorded events. 96
6.12 The effect of selection cuts for the background due to $e^+e^- \rightarrow e^+e^-\tau^+\tau^-$. 100

6.13 Background contribution due to $e^+e^- \rightarrow e^+e^-\tau^+\tau^-$. The τ-sample is normalized to the data luminosity. 102

6.14 Radiative corrections for beam energy $\sqrt{s} = 189$ GeV. 105

6.15 Radiative corrections for beam energy $\sqrt{s} = 196$ GeV. 106

6.16 Radiative corrections for beam energy $\sqrt{s} = 200$ GeV. 107

6.17 Radiative corrections for beam energy $\sqrt{s} = 204$ GeV. 108

6.18 Radiative corrections for beam energy $\sqrt{s} = 206$ GeV. 109

6.19 Variation of the invariant mass W and its influence on the number of selected events. 113

6.20 Upper: Variation of the tag-energy for VSAT, relative to the beam energy; lower: variation of the acoplanarity angle, and their influence on the number of selected events. 114

6.21 Variation of the squared four-momentum transfer and its influence on the number of selected events. 115

6.22 Invariant mass of the two muons in the final state. 118

6.23 Squared four-momentum transfer to the highly virtual photon. . 119

6.24 Fraction of momentum of the highly virtual photon. 120

7.1 The differential cross-section as a function of Q^2 from the reaction $e^+e^- \rightarrow e^+e^-\mu^+\mu^-$. The QED curve has been obtained with the generator `GALUGA`. Only statistical errors are drawn. 127

7.2 The differential cross-section as a function of x, generated with the `VERMASEREN` and the `GALUGA` generator. 129

7.3 Least-mean-square fit for obtaining the average P^2 for the structure function F_2^γ. The value at the vertical axis depicts the reduced χ^2, i.e. χ^2/n_{dof}. 131

7.4 The structure function F_2^γ as a function of x from the reaction $e^+e^- \rightarrow e^+e^-\mu^+\mu^-$. The QED curves have been obtained with Eq. (2.7) and a mean virtuality of $P^2 = 0\,GeV^2$ (dashed line), $P^2 = 0.019\,GeV^2$ (solid line, MC), and $P^2 = 0.031\,GeV^2$ (dotted line, fit) for the target photon, respectively. The data suggest that a non-zero virtuality should be used. Only statistical errors are drawn. 133

8.1 Compilation of measurements of the leptonic structure function $F_{2,QED}^\gamma$ as a function of x, for different Q^2 ranges [55]. 136

List of Tables

2.1 1. Definitions for Eq. (2.5). 21

2.2 2. Definitions for Eq. (2.5). 21

6.1 The various triggers, which were used to record data with L3 and their corresponding code. 92

6.2 Fraction of events that were recorded due to the various triggers. All other triggers had negligible contributions to the event recording. The most abundant triggers, Bit 2, 6, 8 were used to estimate the trigger efficiency. 94

6.3 Sources of systematic uncertainties for the estimation of cross-sections and their contribution to the total systematic error. . . 116

6.4 Selection results after all applied cuts. The trigger efficiency $\varepsilon =$ 96.5% was taken into account for data. 117

7.1 Measured differential cross-section as a function of Q^2 and estimated uncertainties. 126

7.2 Measured leptonic structure function as a function of x with a mean squared four momentum transfer of the untagged electron $< P^2 >= 0.019\, GeV^2$, and estimated uncertainties. 132

Chapter 1

Introduction

Photons have structure and may interact with each other. This statement seems to be in contradiction with the statements made from nowadays experience and from classical electromagnetic theory (EM). On one hand it is said that photons are point-like particles, without further substructure. In addition, EM states that due to the linearity of the Maxwell equations, there is no scattering between electromagnetic waves. This contradiction can be solved if one considers Quantum Mechanics (QM). Photons can fluctuate into states of particles, which might be charged. Heisenberg's uncertainty relation $\Delta t \simeq \frac{2E_\gamma}{m_{pair}^2}$ "allows" photons to fluctuate into intermediate states, where m_{pair} represents the mass of such a state (Fig. 1.1). If E_γ becomes large, Δt, i.e. the lifetime of the intermediate states can also become quite large. These intermediate states will then be

responsible for the interaction of the photons and also for giving a structure to photons.

Since the fluctuation is a statistical process, the probability of the fluctuation into a particular state is described in terms of structure functions.

"Two-Photon-Physics" is the field of research, which describes the interaction between photons. The interest and research in this field started in the 1930's, after the discovery of the positron by Anderson (1932). Of particular interest was the process, how the positron was created. Landau and Lifshitz [1] were performing the pioneering calculations for the total cross-section for two-photon production of lepton pairs, using the Equivalent Photon Approximation (EPA).

One considers the simplest mechanism for elastic scattering of two-photons as

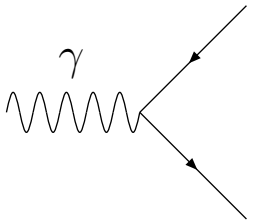

Figure 1.1: Quantum fluctuation of a photon into pairs of charged particles.

described by the box-diagram in Fig. 1.2. Two-photon physics nowadays is of interest, since it allows to test Quantum-Chromodynamics (QCD), the theory of strong interactions: the intermediate states might be strongly interacting

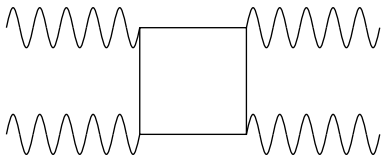

Figure 1.2: Elastic two-photon scattering.

particles.

Experimentally, it is very difficult to collide high energy photon beams. A very elegant way of avoiding this difficulty is the usage of virtual photons, e.g. the quantum fluctuation of an electron into an electron-photon state. Thus, high energy e^+e^--storage rings like the Large-Electron-Positron collider (LEP) are an ideal tool for producing photons. Such accelerators can be considered as Photon-Photon colliders, since a portion of the incoming electrons (positrons) around collision points will be scattered into relatively large angles. Because of this scattering highly virtual photons will be radiated and can be interacting with photons which are emitted by the other beam particle. The increase of the photon emission probability with the increase of the beam-particle's energy makes LEP a source of γ's with continuous energy. Its cross-section is much higher than in any previous e^+e^--storage ring. Altogether, this fact allows to obtain photon fluxes of high intensity; however, the "beam-energies" of such

photons can not be controlled.

The investigation of lepton pair production is a Quantum-Electrodynamics (QED) process (Fig. 1.3), of the order $\mathcal{O}(\alpha^4)$, where α is the Fine-Structure Constant. The information of the kinematics of this process can be obtained

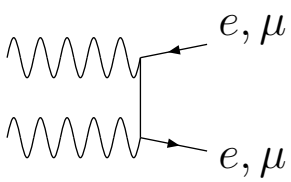

Figure 1.3: Inelastic $\gamma\gamma$-scattering with production of lepton pairs.

by experimental observation, since the final state particles can be completely detected, in contrast to many QCD processes. Thus, the study of lepton pair production from $\gamma\gamma$-collisions will, besides supplying another test of QED, provide important tools for the application in QCD studies. Two-photon processes can also be used to calibrate hadron-hadron colliders, such as the Large-Hadron-Collider (LHC), which is being built at CERN, in Geneva, Switzerland. Most of the methods to obtain the luminosity for such colliders have to use models for strong interactions. This in turn would lead to a not very accurate determination of the luminosity. Budnev et al. have shown [2], that under certain circumstances the process $pp \to pp\mu^+\mu^-(e^+e^-)$ can be completely calculated in

the framework of QED, with an accuracy not worse than 0.1%. The circumstances are basically that the hadrons should not be fragmenting due to the collisions. The verification of the process $e^+e^- \rightarrow e^+e^-\mu^+\mu^-(e^+e^-)$ according to QED will provide the confidence to use a similar process in the determination of the luminosity in $p\bar{p}$-colliders.

The production of lepton pairs due to photon-photon collisions might constitute a significant background where leptons or hadrons appear in the final state. It needs to be recognized and subtracted. Therefore one needs to verify the production of lepton pairs in the framework of QED.

The following work will be describing the investigation of the lepton pair production. This dissertation is subdivided into the following parts: a more detailed description of the theoretical background, which includes the production mechanism of lepton pairs due to $\gamma\gamma$-collisions (Ch. 2), is followed by the description of the LEP accelerator and L3 detector (Ch. 4 and Ch. 5), used for this analysis. In Ch. 6 the tools and selection criteria for acquiring the wanted properties of lepton pair production are described. The results of this analysis will be discussed in Ch. 7, and a conclusion (Ch. 8) will finalize this dissertation.

Chapter 2

Two-Photon Physics

The following sections have the aim of introducing the concepts of two-photon concepts. It is rather an overview of the logical steps, which will eventually lead to quantities, which might be interpretable and comparable to experimental findings. Those results will be used to perform the data analysis.

2.1 Quantum-Electrodynamics: Introduction

Quantum-Electrodynamics (QED) is the theoretical background for the description of the interaction between charged particles. Emerged in the early 1930's, this theory encompassed the desired features to describe the interaction of electrons: it was quantized and relativistically invariant. Feynman diagrams, as

depicted in Fig. 2.2, and the application of Feynman rules are the tools to set up equations, which allow to calculate important properties of these interactions. One of the most important quantities, which describe QED-interactions, is the cross-section[1]. The cross-section is a measure of probability of how likely a certain interaction will happen. It is described with the unit *barn*. The equivalent of 1 *barn* is $10^{-28}\,m^2$. In the early years of particle physics, the cross-section referred to an effective interaction area, that a particle could "see" from other particles.

The cross-section connects two important requirements: a theoretical description of certain interactions has to be calculable in manageable way, and it has to be provable, i.e. it has to be approved by experiments. Since a cross-section can be measured by counting particles, the latter requirement is fulfilled. With a lot of effort from physicist and other scientists, the calculation for the cross-sections is an established fact. Feynman diagrams are sketches of particle's interactions and provide a more intuitive way to set up the equations for cross-sections. The diagrams consist of symbols, which depict different particles (Fig. 2.1). Basically, one can describe all interactions with fermions and bosons. Fermions are spin-$\frac{1}{2}$ particles, whereas bosons are spin-1 particles. Bosons describe the mediators of the different kinds of interactions:

[1]This applies to all kind of interactions.

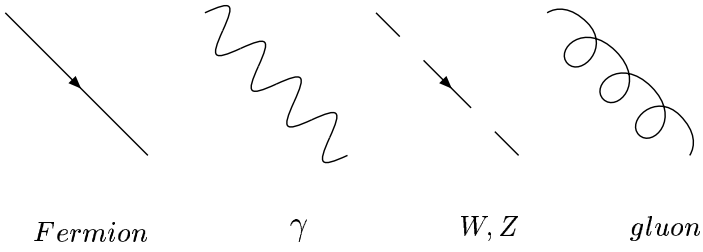

Figure 2.1: Symbols, which are used in Feynman graphs.

- Electromagnetic interaction: γ
- Weak interaction: W, Z
- Strong interaction: gluon

Interactions can be now sketched with Feynman diagrams by assembling all wanted particles and connecting the symbols. The connection points are called *vertices*. At the vertices the mediators are coupling with a strength, according to the type of interaction. For QED, the coupling is proportional to the Fine-Structure constant[2] $\alpha = \frac{e^2}{4\pi\hbar c}$. The expression "constant" is not a very correct one, since $\alpha = \alpha(t)$; it varies with the energy in the interaction as $\alpha(t) = \frac{\alpha_0}{1-\Delta\alpha(t)}$, with $\alpha_0 \approx \frac{1}{137}$ and t being the momentum transfer. It can be significantly different at higher energies, e.g. $\alpha(M_Z) \approx \frac{1}{128}$ [3, 4]. However, the variation for the

[2]It is convenient to use $\hbar \equiv c \equiv 1$. This simplifies calculations and it is straightforward to implement the missing units after calculations, simply with unit considerations.

energy range within this work is relatively small, so that in all practical cases α_0 is used.

Particles, which do not have an open beginning/end in the Feynman diagrams are considered being virtual particles. These particles do not have any right to exist. However, in the framework of QM they are allowed to exist for a time, determined by Heisenberg's uncertainty relation. This concept turned out to be reasonable and is an established fact.

In the vertices the interaction takes place, which is then subject of calculations. There are conventions to be followed, and the compilation of simple processes, like electron-scattering can be calculated in a straightforward way. However, the calculations can become quite tedious when considering more complex interactions. A more detailed description can be found in the excellent textbooks [5, 6, 7].

2.2 QED in Two-Photon Processes

The basic processes in $\gamma\gamma$ collisions, which lead to production of final state particles can be described with inelastic reactions (Fig. 2.2). The very first

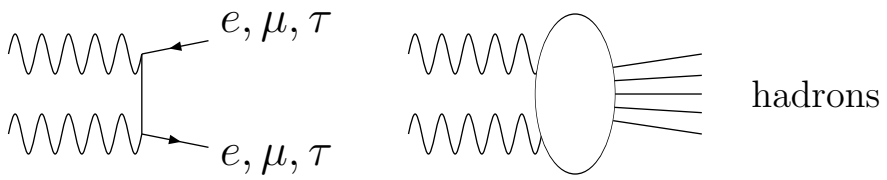

Figure 2.2: Inelastic $\gamma\gamma$-scattering with production of lepton pairs (left), hadrons (right).

photon-photon process, which was observed in e^+e^-−storage ring experiments, was electron pair production $e^+e^- \rightarrow e^+e^-e^+e^-$, performed at VEPPII in 1971, by Balakin et al. [8]. The electron pairs were detected almost coplanar with the colliding beams, at a rate that agreed, within an error of 30%, with an EPA of the cross section.

As mentioned in Ch. 1, Landau and Lifshitz were the first, performing calculations of these processes with EPA. However, almost all practical calculations can use straight forward trace calculations of the relevant Feynman diagrams, in conjunction with sophisticated multi-dimensional Monte Carlo integration. The dominant processes at LEP are $e^+e^- \rightarrow e^+e^- X$, where X describes the

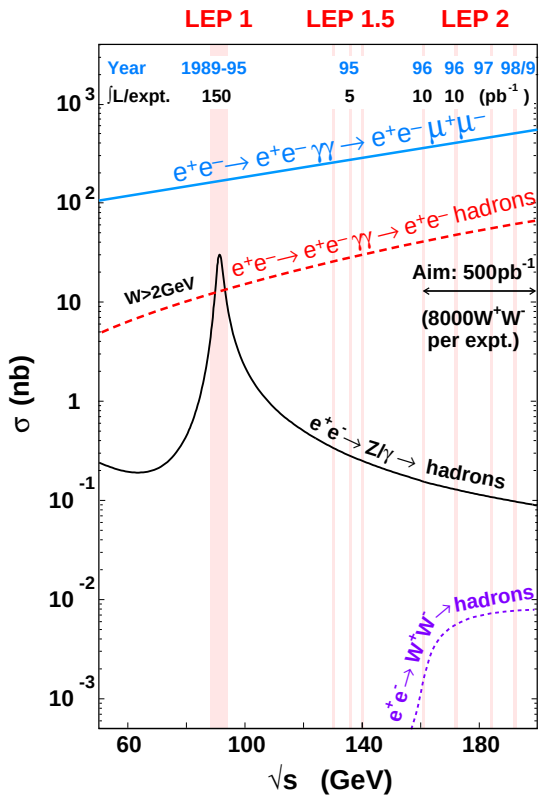

Figure 2.3: Cross-sections for dominant processes for the various LEP phases [9].

system, which is produced in two-photon collisions. The final state X can be hadrons or leptons. As can be seen in Fig. 2.3, the process $e^+e^- \rightarrow e^+e^-\,\mu^+\mu^-$ dominates all other processes at LEP by at least one order in magnitude.

The relevant Feynman diagrams for lepton pair production in two-photon processes can be seen in Fig. 3.1.

2.3 Two-Photon Scattering, Cross-Section

2.3.1 Two-Photon Scattering

The measurements of the structure functions of photons can be performed for three special cases due to experimental constraints [10]. The theoretical description as well as the measurements for these cases will be quite different. One distinguishes between

1. Single tagging
2. Anti-tagging
3. Double tagging

The differences for the cases are incumbent upon the measurement of the so called tagged electrons[3]. The measurements for the different cases define the "virtuality" of the radiated photons. The virtuality is a measure for the magnitude of the negative invariant masses squared of the photons and thus a measure how far the photon is off its mass-shell. This quantity is calculated from the squared four-momentum transfers of the electrons to the radiated photons, which are described by Q^2 respectively P^2, see Fig. 2.4. For case 1., one of the

[3]In the following, the distinction between electrons and positron does not play a role, since they behave identical in terms of two-photon physics.

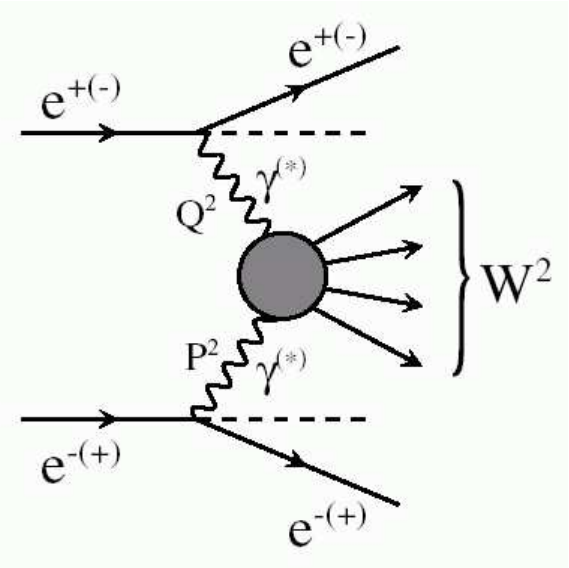

Figure 2.4: Two-photon production and scattering [11].

scattered electrons is observed within an angular range $\theta_{low} < \theta_1 < \theta_{up}$, while the other electron is not observed over the angular range $\theta_{max} < \theta_2 < \pi - \theta_{max}$. This means, that the first electron is detected and precisely measured within a detector system with limited acceptance, whereas the second electron is considered being scattered into the cone with $\theta_2 < \theta_{max}$ or $\theta_2 > \pi - \theta_{max}$. If the angle θ_{max} is sufficiently small, the second electron will not be detected. One considers the second electron being escaped close to the beam line, i.e. outside the detector acceptance. This describes a $\gamma\gamma^*$ collision, since the four-momentum transfer to one photon will vanish, e.g. $P^2 \sim 0$ (quasi-real), whereas Q^2 is mea-

sured. The asterisk is used for virtual photons.

For case 2., neither electron is detected. This is a process with high statistics: both electrons are considered to escape along the beam line, hence this process is a $\gamma\gamma$ process, since $P^2 \sim Q^2 \sim 0$.

Case 3. includes both electrons in the measurement. As a consequence, $P^2 > 0$ and $Q^2 > 0$, the process is a $\gamma^*\gamma^*$ interaction.

The aim of the analysis, described in this work, is to use the single tagging case. Therefore, the discussion of the cross-section and derivable parameters is restricted to the first case.

The study of $e^+e^- \rightarrow e^+e^-\gamma\gamma \rightarrow e^+e^-\, l^+l^-$ ($l = e, \mu, \tau$) allows to establish procedures to be adopted to studies in hadronic photon structure functions. However, although the production of final states with $e^{\pm}$, $\mu^{\pm}$, and $\tau^{\pm}$ have been measured, only the muonic case is feasible to extract the structure function from data [12]. In the case of $e^{\pm}$, theoretical difficulties arise from the ambiguity of scattered and produced leptons. The measurement of $\tau^{\pm}$ becomes difficult because of the short lifetime ($\approx 0.3 \times 10^{-12} s$) of these leptons and subsequent many-particle decay.

The important variables for the extraction of the structure functions, the invariant mass $W_{\mu\mu}$ of the muon-pair and hence the Bjorken-variable x_{Bj} can be determined very accurately. The measurement of the muonic structure function

$F_2^{\gamma,QED}$ is therefore only limited in statistics, in contrast to the hadronic structure function.

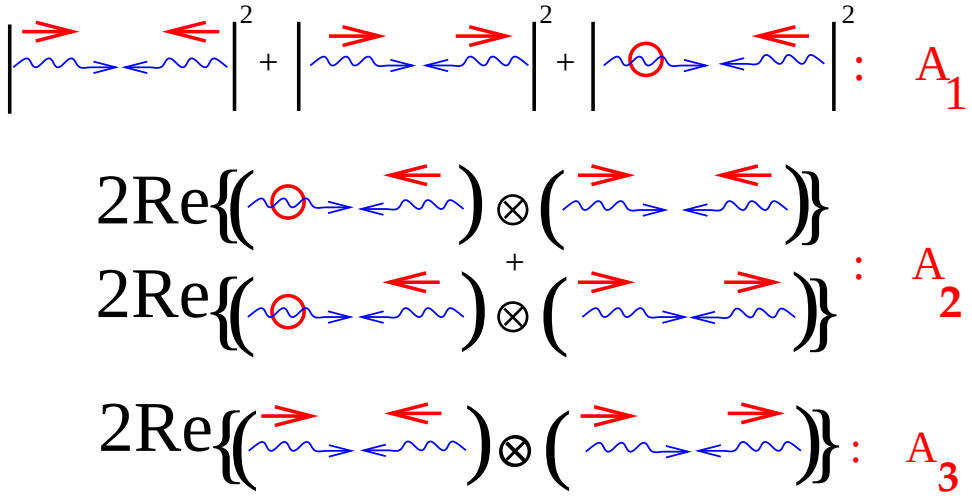

Figure 2.5: The helicity states for a single-tag configuration in two-photon collisions. The arrow depict the transverse helicity state, the circle the longitudinal helicity state of the probe photon [9] (see text).

In addition to $F_2^{\gamma,QED}$, corresponding to scalar and transverse photons, one can also measure other structure functions, $F_A^{\gamma,QED}$ and $F_B^{\gamma,QED}$, which correspond to transitions of photons with spin-flip (Fig. 2.5). The helicity is defined by the spin component in the direction of motion. Since real photons are massless, they cannot have a component parallel to their motion, i.e. they do not have a longitudinal, but only a transversal component. Virtual photons are off the

mass-shell. This means, they can have a longitudinal polarization and therefore a non-zero helicity.

Since one photon is quasi-real, i.e. $m_\gamma \equiv 0$ in the case of single tagging, it does not have a longitudinal polarization. This photon is considered to be the target photon, whereas the other is the photon, which probes the structure of the target photon. Thus, the three amplitudes A_1, A_2, and A_3 are the only ones, which are independent from each other. In Fig. 2.5 one can schematically see the construction of the parameters A_i out of the total photon helicity states λ. A_1 is described with the terms, (Fig. 2.5 from left to right) for $\lambda = 0, 2, 1$. A_2 and A_3 are made up by interference terms. These coefficients are related to $F_2^{\gamma,QED}$, $F_A^{\gamma,QED}$ and $F_B^{\gamma,QED}$ (Sec. 2.3.3).

2.3.2 Cross-Section, Theoretical Framework

The following remarks will be giving an overview of calculational methods in two-photon physics. Details can be found in the comprehensive and elaborated works of [13] and [14].

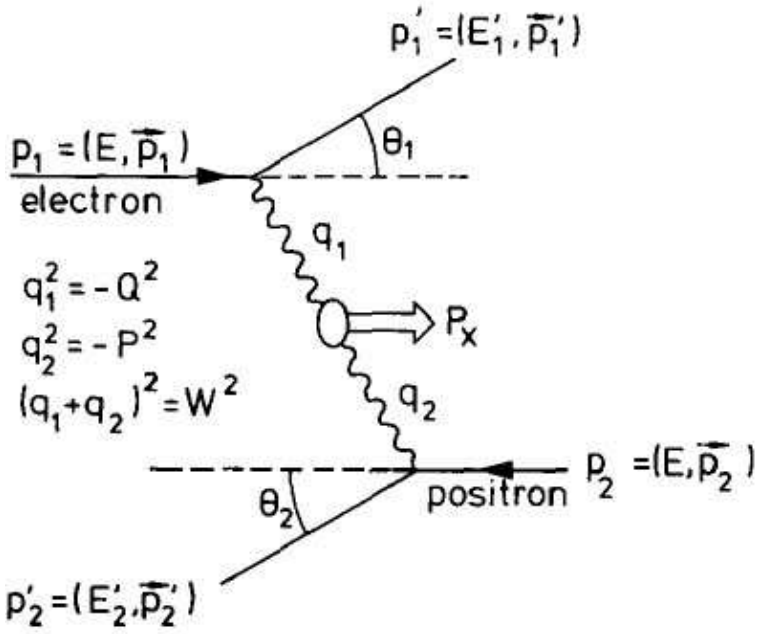

Figure 2.6: Kinematics for two-photon processes [14].

The reaction in Fig. 2.6 depicts the kinematical variables, which are used to describe two-photon processes.

It follows a compilation of the symbols, which will be used in the further discussion:

p_i : colliding particle four-momenta, i=1,2

$s = (p_1 + p_2)^2$: $\sqrt{s} = 2E$, total c.m.s. energy

p'_i : scattered particle four-momenta

$E'_i \equiv p'^0_i$: scattered particle energies

$m_i^2 = p_i^2 = p_I'^2$: rest mass of the colliding/scattered particle

$q_i = p_i - p'_i$: virtual photon four-momenta, $q_i^2 < 0$

k_j : four-momentum of the j-th produced particle

$\epsilon_j \equiv k_j^0$: energy of the j-th produced particle

$k = \Sigma_i k_i = q_1 + q_2$: total four-momentum of the produced system

$\epsilon = k^0 = \Sigma_i \epsilon_i$: total energy of the produced system

$W = \sqrt{k^2}$: effective mass of the produced system

Since the squared four-momenta of the virtual photons are negative, it is convenient to use $q_1^2 = -Q^2$ and $q_2^2 = -P^2$.

As denoted in Ch. 1, Feynman rules are constituting the calculations of the cross-section for two-photon processes. One component of the Feynman rules is the amplitude for the reaction under consideration. The square of the amplitude describes the probability of a process to occur. The amplitude for the

process shown in Fig. 2.6 is given by

$$T = \frac{e^2}{q_1^2 q_2^2} j_\mu j_\nu R^{\mu\nu} \tag{2.1}$$

with

e : electric charge

$j_{\mu,\alpha}$: electromagnetic current of the leptons

$R^{\mu\alpha}$ is connected to the the helicity amplitude $R_{\lambda_1\lambda_2}$ as

$$R_{\lambda_1\lambda_2} = \hat{e}_\mu(\lambda_1)\hat{e}_\nu(\lambda_2)R^{\mu\nu} \tag{2.2}$$

The $\hat{e}_{\mu,\alpha}(\lambda_{1,2})$ are the polarization four-vectors for the photons with helicity $\lambda = \pm 1, 0$. For final leptonic states, e.g. muon-pair production, one can calculate from (2.1) by means of squaring the amplitude T and integrating over the final states. This is a straightforward, but tedious QED calculation. The differential cross-section for two-photon production can be written as

$$d\sigma = \frac{(4\pi\alpha)^2}{q_1^2 q_2^2} \rho_1^{\mu\mu'} \rho_2^{\nu\nu'} (R^{\mu'\nu'})^* R^{\mu\nu} \frac{(2\pi)^4 \delta(q_1 + q_2 - k)}{4\sqrt{(p_1 p_2)^2 - (m_1 m_2)^2}} d\Gamma \frac{d^3 p_1' d^3 p_2'}{2E_1 2E_2 (2\pi)^6} \tag{2.3}$$

In (2.3), $d\Gamma = \Pi_j d^3 k_j / \epsilon_j (2\pi)^3$ is the phase space volume. Integration over the phase space volume yields an expression that includes

$$W^{\mu'\nu'\mu\nu} = \frac{1}{2} \int (R^{\mu\nu})^* R^{\mu\nu} (2\pi)^4 \delta(q_1 + q_2 - k) d\Gamma \tag{2.4}$$

The quantity $W^{\mu'\nu'\mu\nu}$ is the absorptive part[4] of the $\gamma\gamma$-forward amplitude. $W^{\mu'\nu'\mu\nu}$ can be expressed by a sum of combinations of several tensors. The equation for this expression is rather lengthy and can be found as Eq. (5.7) in [13].

The choice of using these particular tensors is given by their simple physical interpretation. They are simply connected with the $\gamma\gamma$-helicity amplitudes in the $\gamma\gamma$ c.m.s. (see Fig. 2.5). The differential cross-section can be then written in terms of cross-sections σ_{ab} and for transition amplitudes τ_{ab}:

$$\begin{aligned} d\sigma &= K(4\rho_1^{++}\rho_2^{++}\sigma_{TT} + 2\rho_1^{00}\rho_2^{++}\sigma_{LT} + 2\rho_1^{++}\rho_2^{00}\sigma_{TL} + \rho_1^{00}\rho_2^{00}\sigma_{LL} \\ &\quad +2|\rho_1^{+-}\rho_2^{+-}|\tau_{TT}\cos 2\tilde{\phi} - 8|\rho_1^{+0}\rho_2^{+0}|\tau_{TL}\cos\tilde{\phi})\frac{d^3p_1' d^3p_2'}{E_1 E_2} \end{aligned} \tag{2.5}$$

The factors K and ρ_i depend on measurable quantities p_i and q_i only (see Table 2.1), and the index T, L correspond to transversal and longitudinal polarization, respectively (see Table 2.2).

Eq. (2.5) applies in its form to unpolarized beam particles. It should be noted, that in the case of polarized beam particles, there will be two more interference terms. However, there have been no experiments, which used polarized electron beams, so the terms are of no interest so far.

If one is interested in differential cross-sections, the outcome of such calculations

[4] Also known as the imaginary part of the two-photon exchange amplitude, which is a complex number.

$$\nu = q_1 \cdot q_2$$

$$K = \frac{\alpha^2}{16\pi^4 q_1^2 q_2^2}\sqrt{\frac{\nu^2 - q_1^2 q_2^2}{(p_1 p_2)^2 - m^4}}$$

$$2\rho^{++} = \frac{(2p_1 q_2 - q_1 q_2)^2}{\nu^2 - q_1^2 q_2^2} + 1 + \frac{4m^2}{q_1^2}$$

$$\rho_1^{00} = 2\rho_1^{++} - 2 - \frac{4m^2}{q_1^2}$$

$$\rho_2^{++} = \rho_1^{++}(1 \leftrightarrow 2)$$

$$\rho_2^{00} = \rho_1^{00}(1 \leftrightarrow 2)$$

$$|\rho_i^{+-}| = \rho_i^{++} - 1$$

$$|\rho_i^{+0}| = \sqrt{(\rho_i^{00} + 1)|\rho_i^{+-}|}$$

Table 2.1: 1. Definitions for Eq. (2.5).

$$\sigma_{TT} = A \cdot \frac{1}{2}(W_{++,++} + W+-,+-)$$

$$\sigma_{TL} = A \cdot W_{+0,+0}$$

$$\sigma_{LT} = A \cdot W_{0+,0+}$$

$$\sigma_{LL} = A \cdot W_{00,00}$$

$$\tau_{LL} = A \cdot W_{++,--}$$

$$\tau_{TL} = A \cdot \frac{1}{2}(W_{++,00} + W_{0,+,-0})$$

$$A = \frac{1}{2\sqrt{\nu^2 - q_1^2 q_2^2}}$$

Table 2.2: 2. Definitions for Eq. (2.5).

can become rather cumbersome. For that it is easier to use Monte Carlo event generators, which will be discussed in Section 3.

2.3.3 Lepton Pair Production in Single Tag Configuration

Taking photon 1 as the probing photon and photon 2 as the target photons, the tensor $W^{\mu'\nu'\mu\nu}$ from (2.4) can be averaged over the target polarization states. The resulting tensor $W^{\mu\nu}$ can be decomposed into the following form:

$$\begin{aligned} W^{\mu\nu} &= -\frac{g_{\alpha\beta}}{2} W^{\nu\beta\mu\alpha} \\ &= 8\pi^2\alpha \left\{ \left(-g^{\nu\mu} + \frac{q_1^\nu q_1^\mu}{q_1^2} \right) W_1 + \left(q_2^\nu - q_1^\nu \frac{q_1 q_2}{q_1^2} \right) \left(q_2^\mu - q_1^\mu \frac{q_1 q_2}{q_2^2} \right) W_2 \right\} \end{aligned} \tag{2.6}$$

where $g_{\alpha\beta}$ is the metric tensor.

If one sets[5] $F_1 \equiv W_1$ and $F_2 \equiv W_2$ ([13, 14]), one obtains the two structure functions

$$\begin{aligned} F_1 &= \frac{\sqrt{\nu^2 - q_1^2 q_2^2}}{4\pi^2\alpha} (\sigma_{TT} - \frac{1}{2}\sigma_{TL}) \\ F_2 &= \frac{\nu |q_1^2|}{4\pi^2\alpha\sqrt{\nu^2 - q_1^2 q_2^2}} \left(\sigma_{TT} + \sigma_{LT} - \frac{1}{2}(\sigma_{LL} + \sigma_{TL}) \right). \end{aligned} \tag{2.7}$$

The single tag case consists of a scattered beam particle, which emits a photon of high virtuality, which can be expressed as Q^2. The magnitude of Q^2 can be

[5] In the following the discussion will be restricted to QED structure functions. Hence the index QED will be neglected.

measured by the four-momentum transfer of the tagged electron:

$$Q^2 \simeq 4E_{beam}E_{tag}\sin^2\frac{\theta_{tag}}{2} \tag{2.8}$$

The other beam particle will be scattered at very small angles, most often very close to the beam line. The latter will emit a photon, which receives a very low four-momentum transfer ($q_2^2 \to 0$), i.e. it will be almost real. These photons are called *quasi-real* and can be interpreted as photons, which are emitted and absorbed by a charged particle, as the electron is. Hence, one can interpret the single tag configuration as deep inelastic electron-photon scattering $e\gamma \to eX$. The calculation of the cross-section simplifies in that case. The terms of (2.5) with index L at second place will vanish, since the target photon does not have a longitudinal polarization. The necessary integration of (2.5) over the polar and azimuthal angle of the outgoing, low-angle scattered electron yields a form similar to electroproduction:

$$d\sigma_{ee\to eeX} = \int_{\Omega_2} L_{TT}(\sigma_{TT} + \varepsilon\sigma_{LT})\frac{d^3p_1'}{E_1'}\frac{d^3p_2'}{E_2'} \tag{2.9}$$

with the variables $L_{TT} \equiv 4K\rho_1^{++}\rho_2^{++}$ and $\varepsilon = \frac{2(1-y)}{1+(1-y)^2}$. The scaling variables y and z are defined as

$$\begin{aligned} y &= \frac{q_1\cdot q_2}{p_1\cdot p_2} = 1 - \frac{E_1'}{E}\cos^2\frac{\theta_1}{2} \approx \frac{E-E_1'}{E} \\ z &= \frac{E_{\gamma,2}}{E} \end{aligned} \tag{2.10}$$

As the name implies, the latter variables describe a scaling behavior, i.e. they are independent of the magnitudes of individual quantities and only the ratio is of interest. Another scaling variable, which will be used very often is the Bjorken-x variable [15]:

$$x = \frac{Q^2}{Q^2 + P^2 + W^2} \tag{2.11}$$

All these variables are dimensionless and the physical meaning of those variables are straightforward:

- $\star$ x: fraction of beam particle's four-momentum, submitted to the radiated photon.
- $\star$ y: fraction of energy-loss of the beam-particle due to radiation of a photon, also called *inelasticity*.
- $\star$ z: fraction of energy relative to $\frac{1}{2}$ of c.m.s.-energy carried by the photon.

When integrating (2.9), one obtains

$$d\sigma_{ee\to eeX} = \Gamma_t(\sigma_{TT} + \varepsilon\sigma_{LT}) f_{\gamma/e} d\Omega_1 dE_1' dz \tag{2.12}$$

with

$$\begin{aligned} \Gamma_t &= \frac{\alpha}{2\pi^2}\frac{E_1'}{Q^2}\frac{1+(1-y)^2}{y} \\ \varepsilon &= 2\frac{1-y}{1+(1-y)^2} \\ f_{\gamma/e}(z;\theta_{2,max}) &= \frac{\alpha}{\pi z}\left[(1+(1-z)^2)\cdot\ln\left(\frac{E(1-z)}{mz}\theta_{2,max}\right) - 1 + z\right] \end{aligned} \tag{2.13}$$

For comparison with experimental observables it is more convenient to rewrite the cross-section with variables, which are easier accessible and interpretable. Eq. (2.9) can be written as a differential cross-section with respect to x and Q^2, as well as the fraction of the energy of the target photon x_2 with respect to the beam energy[6] [13, 16]:

$$\begin{aligned} \frac{d^3\sigma_{e\gamma\to e\mu^+\mu^-}}{dxdQ^2dx_2} &= \frac{2\pi\alpha^2}{xQ^4}\frac{dN_{\gamma,2}}{dx_2}\times \\ &\quad \left\{[1+(1-y)^2]F_2^\gamma(x,Q^2,P^2) - y^2F_L^\gamma(x,Q^2,P^2)\right\} \end{aligned} \tag{2.14}$$

Herein, the longitudinal and transversal structure functions

$$F_L = F_2 - 2xF_T \propto \sigma_{TL} \text{ with } F_T \equiv F_1 \propto \sigma_{TT} \tag{2.15}$$

were introduced.

The term

$$\frac{dN_{\gamma,2}}{dx_2} = \frac{\alpha}{\pi x_2}\left\{[1+(1-x_2)^2]ln\left(\frac{2E_{beam}(1-x_2)}{m_e x_2}\sin\frac{\theta_2^{max}}{2}\right) - 1 + x_2\right\} \tag{2.16}$$

corresponds to the flux of the target photons, i.e. the number of photons expected in the range dx_2. This is also called the luminosity function.

Eventually, one can write (2.14) as

$$\frac{d^3\sigma}{dxdQ^2dx_2} = \frac{d^2\sigma}{dxdQ^2}\frac{dN_{\gamma,2}}{dx_2} \tag{2.17}$$

[6]Similarly, x_1 corresponds to the probe photon.

2.4 Structure Functions

Eq. (2.14) includes quantities that can be measured. Since the variable x_2 is not directly accessible, one has to integrate (2.14) over x_2. The measurable quantities are then the differential cross-section $d^2\sigma/dxdQ^2\,, x$ and Q^2. This allows to measure the structure function F_2^γ. The measurement of $d^2\sigma/dxdQ^2$, however, is practically limited to the measurement of F_2. Because of the smallness of y and hence the sensitivity in y^2, the measurement of F_L becomes a very difficult task.

The aim of this work is to make a measurement of the differential cross-section w.r.t. the virtuality Q^2 of the probing photon in the very low kinematical region, $0.2\,GeV^2 \leq Q^2 \leq 0.85\,GeV^2$. In addition, the leptonic structure function F_2 was investigated. These measurements present the first of its kind in the very low Q^2-region as mentioned above in conjunction with the very high beam energies of LEP. The measurements allow to gain detailed insight for $0.2\,GeV^2 \leq Q^2 \leq 0.85\,GeV^2$ and for $0 \leq x \leq 0.2$. The following describes the procedure, how to extract the structure function from an experimental data sample.

2.4.1 The Differential Cross-Section

The cross-section is the product of the structure function and the luminosity function of the target photon. In order to calculate the luminosity function, one has to integrate over the phase space of the untagged electron, since no direct information is available.

Due to the discrete nature of measurements, the differential cross-section (2.17) cannot be physically measured in a continuous way. It has to be expressed in a discrete form:

$$\frac{d^2\sigma}{dxdQ^2} \simeq \frac{\Delta^2 N}{\Delta x \Delta Q^2} \frac{1}{\mathcal{L}} \tag{2.18}$$

where N corresponds to the number of events, measured in the respective bins, and $\mathcal{L}$ being the integrated luminosity of the data sample.

The integrated luminosity is a measure of how many interactions of the beam particles is taking place, normalized to a cross section. This quantity is a parameter, which directly gives a measure of the performance of an accelerator machine [17]:

$$\mathcal{L} = \frac{1}{4\pi} \frac{f_u N_1 N_2}{\sigma_x \sigma_y} \tag{2.19}$$

One can immediately see, that the performance will increase with the number of beam particles N_i in each beam, and with the decrease of spatial extensions $\sigma_{x,y}$ in the $x-$ and $y-$direction, respectively. Furthermore, the performance is

enhanced, the higher the collision frequency f_u, with which the beams will be allowed to collide.

In practice, it is difficult to measure the luminosity from these parameters, since one has to rely on a precise measurement of all quantities. One way to overcome this problem is to use a reaction, whose cross-section is well known. If one now "counts" the number N_{σ_k} of events of this particular reaction with the known cross-section σ_k, one can deduce very accurately the luminosity in a particular collision point[7]:

$$\mathcal{L} = \frac{N_{\sigma_k}}{\sigma_k} \tag{2.20}$$

For e^+e^-–collider, one of the best known and very well established cross-sections are for the reaction $e^+e^- \to e^+e^-$, which is known as Bhabha-Scattering. It can be measured with a very high precision ($< 0.1\%$), and is dominated by its theoretical uncertainty [18].

2.4.2 The Structure Function F_2^γ

The structure function F_2^γ can be accessed with a Monte-Carlo generator, which produces events according to (2.5). The addends can be expressed in terms of structure functions, as in (2.7). The basic idea of extracting F_2^γ is to set this parameter as a fixed value in the program and compare the measured differen-

[7] Also called *vertex*.

tial cross-section with it. In other words, one normalizes the structure function to a fixed differential cross-section, say, $1\,nb$, and refers to the measured cross-section. The ratio of the differential cross-section and the normalized differential cross-section uncovers F_2^γ.

This can in principle be done with MC generators, like `VERMASEREN`, by means of modifying the program such, that it generates events according to $F_2 = 1\,nb$. However, there exists a Monte Carlo program, `GALUGA` [19], which can be used in a very convenient way.

Mainly developed to handle hadronic events in the final state, the `GALUGA` program incorporates the five structure functions[8] σ_{AB} and τ_{AB} as of (2.5), where $A = (T, L), B = (T, L)$. It calculates the differential cross-section for $e^+e^- \to e^+e^-X$ at given two-photon invariant mass W, or integrated over W. This cross-section is rewritten in terms of the photon virtualities q_i as the outermost integration variables (next to W), in order to simultaneously cope with anti-tagged and tagged electron modes. Cuts on the scattered electrons are to a large extent incorporated analytically and suitable mappings introduced to deal with the peaking structure of the differential cross-section. `VEGAS` (Sec. 3.4) can be optionally invoked to obtain an accurate estimate of the integrated cross-section and to improve the event generation efficiency through additional

[8] $\sigma_{TL}(W, q_1^2, q_2^2) = \sigma_{LT}(W, q_1^2, q_2^2)$.

variable mappings provided by the grid information of `VEGAS`.

The program allows to easily add/modify additional hadronic or leptonic reactions. For this work the program was modified such, that a calculation according to (2.5) could be performed, as well as according to the differential cross-section, expressed in terms of the structure functions

$$\begin{aligned} d\sigma &= K\Big(2|\rho_1^{+-}\rho_2^{+-}|\tau_{TT}\cos 2\tilde{\phi} - 8|\rho_1^{+0}\rho_2^{+0}|\tau_{TL}\cos\tilde{\phi} \\ &\quad +2\rho_1^{++}\rho_2^{00}\big\{F_2(W,q_1^2,q_2^2)/D - F_1(W,q_1^2,q_2^2)/C\big\} \\ &\quad +4\rho_1^{++}\rho_2^{++}F_1(W,q_1^2,q_2^2)/C\Big)\frac{d^3p_1' d^3p_2'}{E_1 E_2} \end{aligned} \tag{2.21}$$

where C, D are the corresponding factors to the structure functions in (2.7). For (2.21) the first index of the cross-sections σ_{AB} and τ_{AB} corresponds to the target photon, and the second index corresponds to the probe photon [9].

In (2.21) one can now set $F_2(W, q_1^2, q_2^2) \equiv 1$ and compare $d\sigma(F_2)$ with $d\sigma(F_2 = 1)$[10]:

$$F_2^\gamma/\alpha = \frac{d\sigma_{measured}}{d\sigma_{Galuga,F_2=1}} \tag{2.22}$$

[9] The cross-sections with the first index L do not appear, since the assumption was made, that the target photon is quasi-real, hence it cannot have a longitudinal polarization.

[10] It is convenient and has been accustomed to depict the structure function divided by the fine-structure constant α.

Chapter 3

Monte Carlo Techniques

QED evaluations can be performed with analytical calculations. These evaluations allow the comparison with experimental distributions. In general, integrals will be evaluated, but can become most often an impossible task due to its complexity. In this case, numerical methods must be used. However, even the simplest first-order numerical integration can become quite tedious for a multidimensional integral. A one-dimensional integral of a function can be determined efficiently by evaluating the function N times on a regular grid, where the number of samples N depends on the structure of the function and the required accuracy. A two-dimensional integral requires sampling in two dimensions and, for accuracy comparable to that of the one-dimensional problem, requires something like N^2 sample. This game can be continued and the number

of samples increases by a factor of something like N for each additional dimension. Such calculations can become quickly excessively large and will meet, even with nowadays high computing power resources a problem.

A way to overcome this problem is the usage of Monte Carlo methods. Instead of performing calculations for each regular grid-point, one uses random sampling from probability distributions. Practically this is done by means of calculating probabilities and related quantities by using sequences of random numbers.

The Monte Carlo method can be applied whenever the solution to a problem can be related to a parameter of a probability distribution. This could be either an explicit parameter in a probability distribution function, or the integral of the distribution over some region. A sequence of Monte Carlo generated values is used to evaluate an estimator for the parameter (or integral), just as is done with real data.

The Monte Carlo method is often used to simulate experimental data. In particle physics, this is usually done in two stages: event generation and detector simulation. The program for the former is called an *event generator*. It generates events according to a certain distribution, which is dependent on the cross-section, including necessary kinematic variables, e.g. momentum or angles. Its output serves as the input for the *detector simulation* program, see Sec. 3.5. Details can be found in [20, 21, 22].

The traditional method for generating events with a limited experimental acceptance is to generate events according to the total cross-section and applying cuts hereafter. This in turn means, that a number of events will be dismissed after generation, if they will not survive the cut. The efficiency of generation could thus drop significantly. Such a program is called an event generator of first kind.

A more practical method is to implement cuts during the integration or during event generation. One idea, how this should be done is rewriting the phase-space integral such, that the cuts, which reduce the event rates most, can be expressed in a single integration variable. With that one can remove most the appearing discontinuities by readjusting the integration boundaries. Event generation according to this method will be called event generation of second kind. The following sections will briefly discuss the event generators, which were used for the present analysis. These generators will basically deal with reactions as depicted in Fig. 3.1.

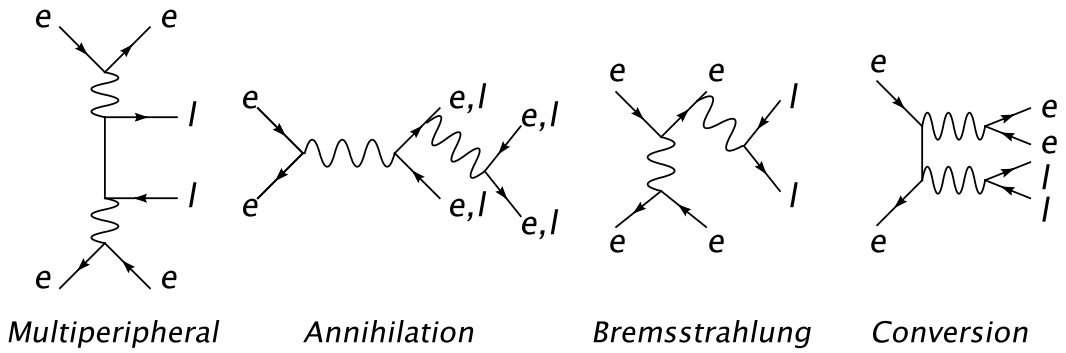

Figure 3.1: Feynman diagrams of $\mathcal{O}(\alpha^4)$, describing $e^+e^- \to e^+e^-l^+l^-$, where l stands for leptons.

3.1 The Vermaseren Generator

The `Vermaseren` Monte Carlo generator has become the *de facto* standard calculation for $\gamma\gamma$-collisions through the process $e^+e^- \rightarrow e^+e^- f\bar{f}$, where f and $\bar{f}$ are fermions and anti-fermions in the final states, respectively [23].

This generator takes only the first diagram from Fig. 3.1 into account. The *Multiperipheral* is indeed the interesting diagram, that this analysis is aiming for. The other diagrams, *Annihilation, Bremsstrahlung*, and *Conversion* are considered as background and will be evaluated with the Monte Carlo generator `BDK` (Ch. 3.2).

Generators of second kind can exhibit correlations between several variables in the peaks of the matrix elements, which might complicate the integration. In addition, there could be more cuts than variables, so it might be impossible to remove all discontinuities.

The `Vermaseren` generator overcomes these problems by means of complete reformulation of the basic phase-space integrals. The integral is rewritten so that the denominators of the propagators, which are responsible for severe peaks of the matrix element, are used directly as integration variables. However, this method introduces the dependency of nearly all cuts of more then one variable. But this will not constitute a severe problem, since good automatic integration

programs like VEGAS [24] are available (see Ch. 3.4).

3.2 The BDK Generator: DIAG36

The DIAG36 generator is an event generator for a full set of QED diagrams for the reaction $e^+e^- \rightarrow e^+e^- f\bar{f}$, including all fermion masses [25]. It emanates from the BDK generator-family, which also has extended versions for the treatment of radiative corrections and large angle tagging cases [26, 27]. This generator can be used to generate events according to all diagrams from Fig. 3.1, but also for individual or combinations of individual diagrams. For that it is divided in a series of sub-generators.

DIAG36 can cover the whole kinematically allowed phase space by means of phase-space generation, or cuts can be applied for typical single- or double-tagged configurations.

The calculation of 12 Feynman diagrams for the $e^+e^- \rightarrow e^+e^-\mu^+\mu^-$ case (36 for $e^+e^- \rightarrow e^+e^-e^+e^-$) is performed at the amplitude level using a suitable set of spinor definitions. This approach avoids the complete calculation of the matrix elements, which cannot be deduced from standard spin summing and trace evaluations.

The event generation poses some problems of itself. In the $e^+e^- \rightarrow e^+e^-e^+e^-$

case the multi-differential cross section has 657 different peaks in a seven dimensional phase-space, which all have to be carefully accounted for. Moreover in order to ensure numerical stability different sets of integration variables have to be used to describe the structure of the occurring peaks. The cross section is treated as a square of an amplitude, which consists of a sum of specifically chosen sub-amplitudes. Each sub-amplitude squared is generated by a (sub)generator in which the phase-space variables have been chosen such that the peaking structure is properly taken into account. The interference between the sub-amplitudes is taken care of by imposing a weight on the events.

Although the `BDK` is the most complete generator for $\gamma\gamma$-reactions in QED, this generator was used in this analysis for background estimations only. The `Vermaseren` generator was used for generating events to be compared with experimental data. The reason is mainly due to the fast event generation compared to `BDK`, which is generator of first kind, i.e. it treats cuts with the hit-or-miss technique.

3.3 Radiative Corrections with RADCOR

The `RADCOR` generator emanates from the `BDK`-generator family [27]. It generates events of the order $\mathcal{O}(\alpha^5)$ and one can consider the radiative corrections to

the electron lines in the multiperipheral diagrams (Fig. 3.2).

Experimentally, it is hard to distinguish such cases, in particular when the radiated (real) photon is close by the tagged electron. Detectors most often do not have the capability to separate those photons from the electron and the measured energy will be falsely assigned only to the electron.

`RADCOR` is an event generator which gives sets of momenta of the outgoing particles, distributed according to the exact cross section. Every time the program is called, one event is returned. On the basis of the total approximate cross sections for soft (this includes the virtual corrections) and hard bremsstrahlung it is decided in the program which kind of event will be produced. In either case the event is first generated according to an approximate distribution. The approximations used are accounted for by the assignment of a weight to the events.

The effect of radiative corrections on the cross-section is usually on the percent level, but increases under stricter cuts like large angle, single tagging.

3.4 VEGAS

`VEGAS` performs the integration of a given function f over a n-dimensional unit-cube. `VEGAS` works basically as follows: it starts with dividing all axes into

a number of bins. Now it throws a number of points around, which leads to an estimate of the integral, its error and the behavior of the function over the integration region. This information about the behavior is obtained by adding the result of a function evaluation only to the n bins, one in each direction, that correspond to the n values of x(i) (the x(i) are the n integration variables). Using this information it now changes the sizes of the bins in such a way that some combination of bin contents and bin contributions to the error is expected to be as evenly distributed over the bins as possible. Now it starts the next iteration by throwing points around, evenly distributed over the new bins. By doing this, the error per iteration can go down considerably during the first few iterations. After a number of iterations an optimal bin distribution has been reached, and the error per iteration stays roughly constant.

3.5 L3 Detector Simulation: GEANT, GEISHA

The L3 detector response was simulated with the GEANT [28] and GEISHA [29] packages.

The GEANT program simulates the passage of elementary particles through matter. The principal applications of GEANT in High-Energy Physics are the transport of particles, i.e. tracking through an experimental setup for the simulation

of detector response, and the graphical representation of the setup and of particle trajectories.

GEISHA is a hadronic shower generator and is the interface to GEANT.

For effects, which cause non ideal detector operations, one needs to correct accordingly. Thus, detector inefficiencies, as monitored during the data taking period, are included in the GEANT-L3 setup.

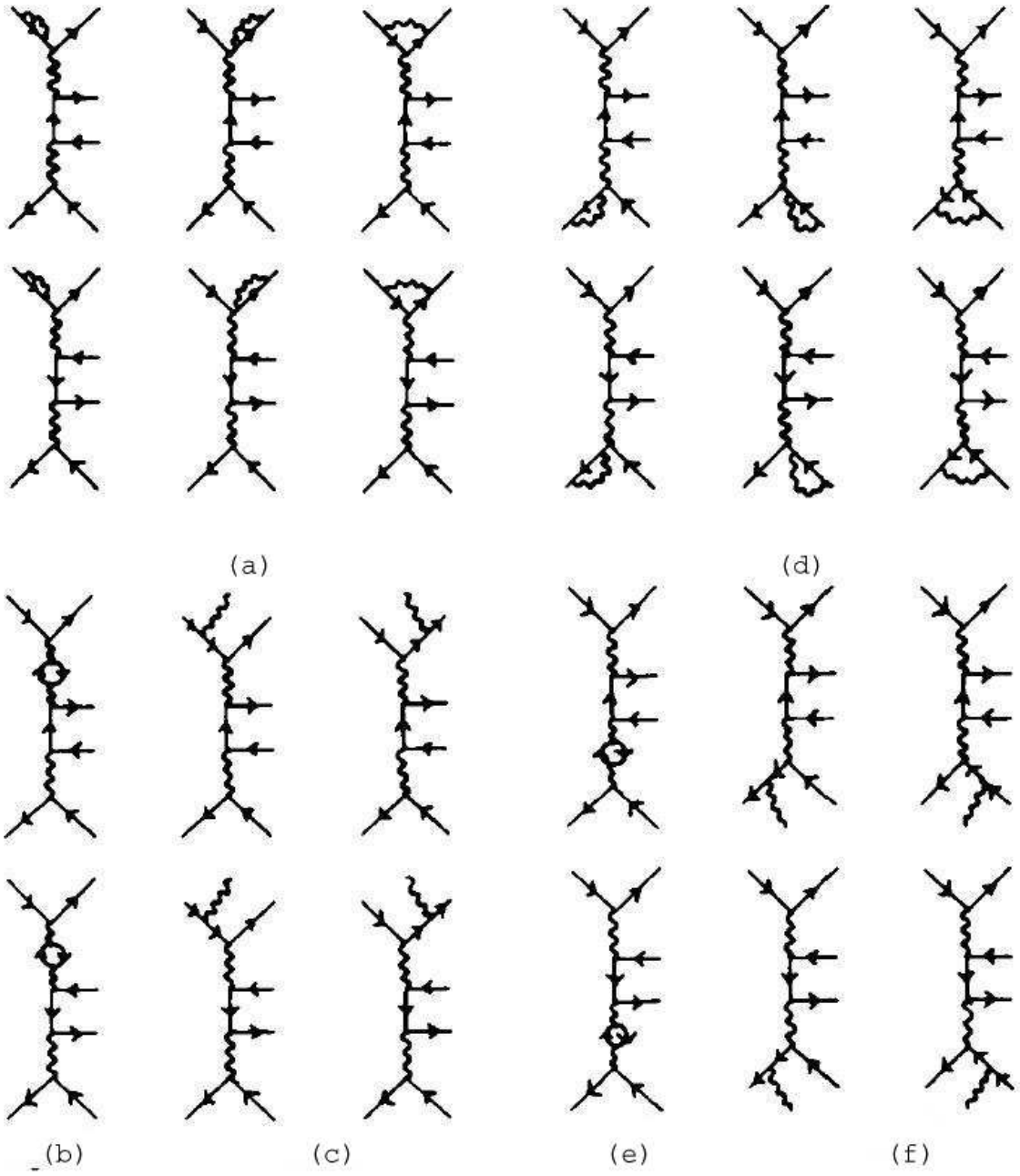

Figure 3.2: (a,b) Self-energy and vertex diagrams. (b,e) Vacuum polarization diagrams. (c,f) Bremsstrahlung diagrams [27].

Chapter 4

The Large Electron Positron Collider (LEP)

The Large Electron Positron Collider (LEP) [30], with a circumference of 26.7km and an elevation between 50m and 150m below ground, straddled the French-Swiss border west of Geneva, Switzerland. It was the largest accelerator complex at the European Nuclear Research Center (CERN) and started its operation in 1989, and from its size, it was even the largest acceleration complex in the world. LEP terminated its operation in late 2000 and is being replaced by the Large Hadron Collider (LHC), which is expected to start its operation in 2007.

As the name implies, LEP stored electrons and positrons, for collisions at four distinguished points along the beam line (Fig. 4.1). These four interaction points

were surrounded by sophisticated detector complexes: ALEPH [31], DELPHI [32], L3 [33], and OPAL [34]. All these detectors were general purpose detectors and designed to precisely measure parameters of the Standard Model. They differed from each other in terms of sensitivity with respect to different approaches of collecting events and were optimized differently to study various physics aspects.

The positrons were obtained by accelerating electrons in a LINAC[1] to 200 MeV and have them collided with a tungsten target. Due to photo-conversion positrons were created and further accelerated in a second LINAC, up to energies of 600 MeV. Likewise, the electrons were accelerated up to 600 MeV, and both, electrons and positrons were accumulated in the EPA[2]. The electrons and positrons were then injected into the PS[3] and accelerated up to 3.5 GeV, subsequently experienced an injection into the SPS[4], where they reached energies up to 20 GeV. Eventually the electrons and positrons were injected into LEP and accelerated up to their final energy (Fig. 4.2). Eight equidistant bunches of electrons and positrons were to travel in opposite directions, in the same accelerator tube, for colliding in the four collision points with a rate of about

[1]LINear ACcelerator

[2]Electron Positron Accumulator

[3]Proton Synchrotron, operating as an e^+e^- synchrotron

[4]Super Proton Synchrotron, operating as an e^+e^- synchrotron

88 kHz.

The LEP collider's initial c.m.s. energy was chosen to be around 91 GeV, so that these collisions could produce Z^0 bosons (LEP1 phase). Since the end of 1995, LEP has moved on from LEP1 and entered a phase (LEP 1.5), where the energy of the colliding particles was steadily increased. In its last years (1998-2000), the LEP2 phase was reached, starting with energies of 189 GeV, and ultimately reaching 209 GeV. This allowed to produce W^+W^- pairs.

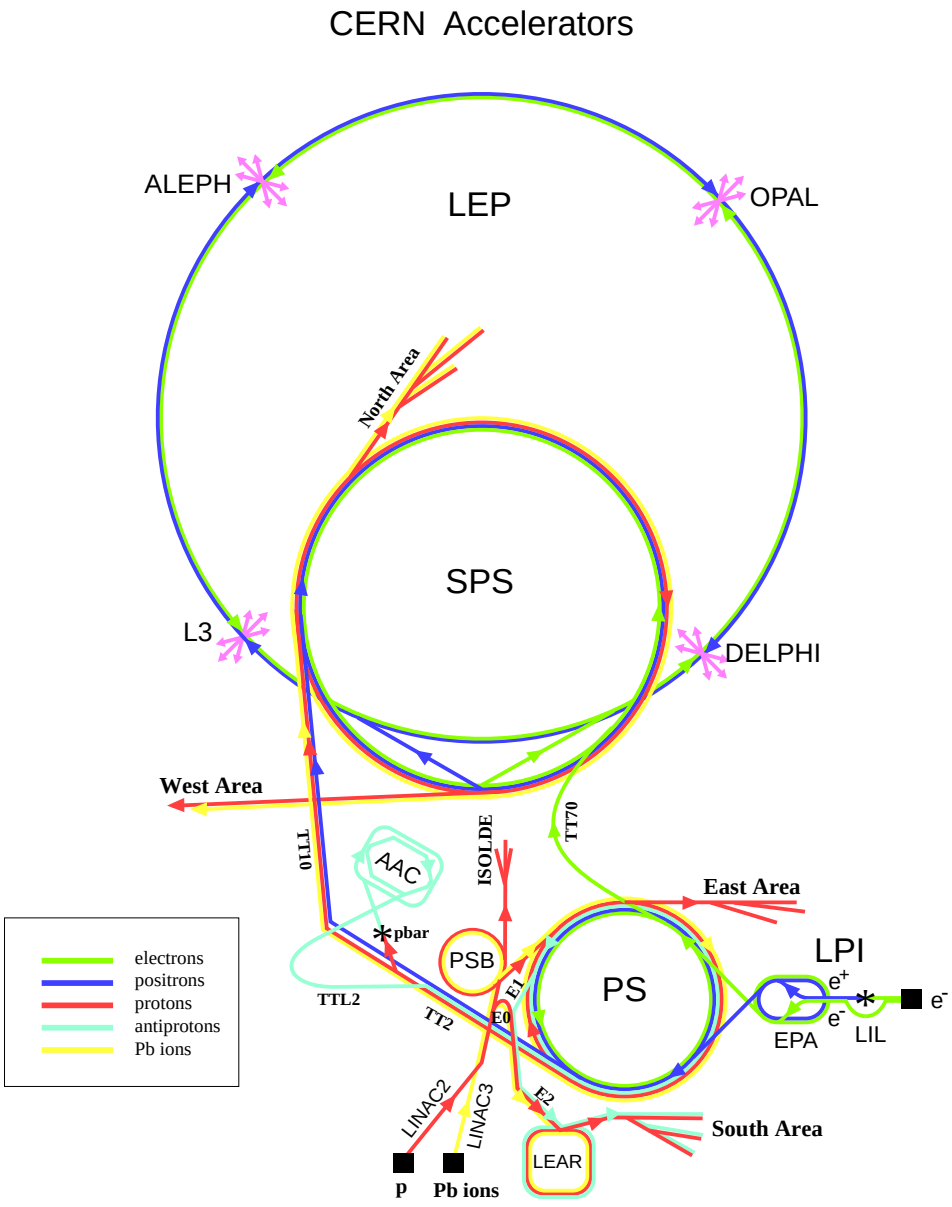

LEP: Large Electron Positron collider
SPS: Super Proton Synchrotron
AAC: Antiproton Accumulator Complex
ISOLDE: Isotope Separator OnLine DEvice
PSB: Proton Synchrotron Booster
PS: Proton Synchrotron
LPI: Lep Pre-Injector
EPA: Electron Positron Accumulator
LIL: Lep Injector Linac
LINAC: LINear ACcelerator
LEAR: Low Energy Antiproton Ring

Figure 4.1: Schematic sketch of the LEP accelerator [9].

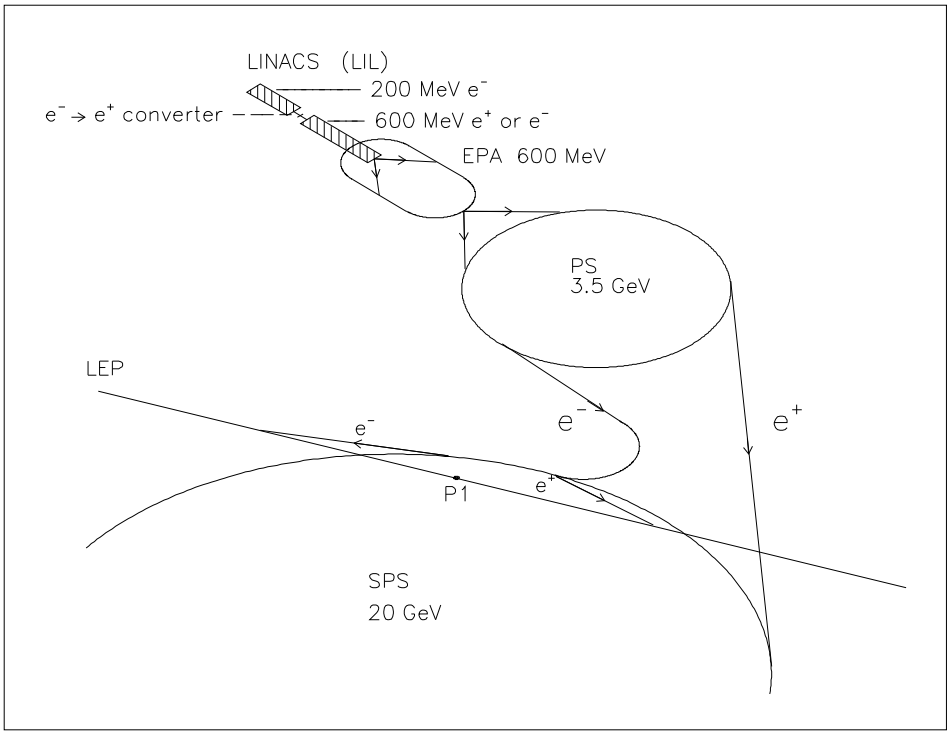

Figure 4.2: Schematic sketch of injection and acceleration processes for LEP [9].

Chapter 5

The LEP experiment L3

L3 [33] was one of the four experiments at LEP, installed 50 m below ground around the beam-line of LEP at the collision point P2. L3 was a symmetric detector of cylindrical shape around the primary vertex point and consisted of a series of sandwiched sub-detectors, optimized to detect particles according to their physical nature. It was a hermetic detector, covering about 99% of the 4π solid angle. The detectors have been optimized for the energy resolution on electrons, photons, muons, and jets. It was surrounded by a 7800 tons octagonally shaped solenoid coil magnet. The magnet was of conventional nature, i.e. not super conductive, with a maximum magnetic flux of 0.5 T. Within a volume of 12 m diameter and 12 m length, the 30 kA current provided a uniform field parallel to the beam direction. The magnetic field allowed, in conjunction with

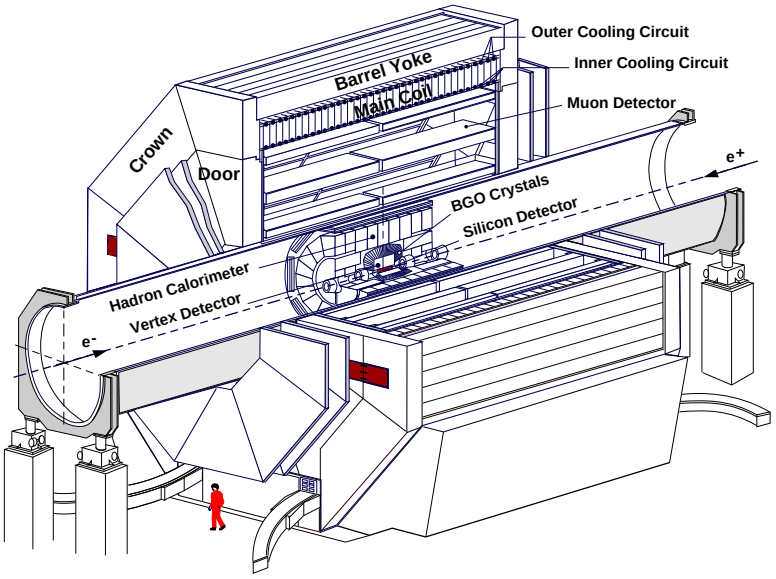

Figure 5.1: Perspective view of the L3 detector [9].

tracking devices to deduce the momentum of a charged particle, which traverses the detector volume. At the endcaps, the endcap muon detectors were exposed to a toroidal 1.5 T magnetic field. The detector complex was supported by a 32 m long and 4.45 m in diameter steel tube, which was concentrically arranged around the beam tube. Alignment for the support was assured by a feedback system, that continuously monitored and corrected for deviations. The basic components of L3 were radially arranged, from the inner to the outer part of the detector:

- The central tracking device, consisting of a Silicon Microvertex Detector (SMD) and a Time Expansion Chamber (TEC) for determining the

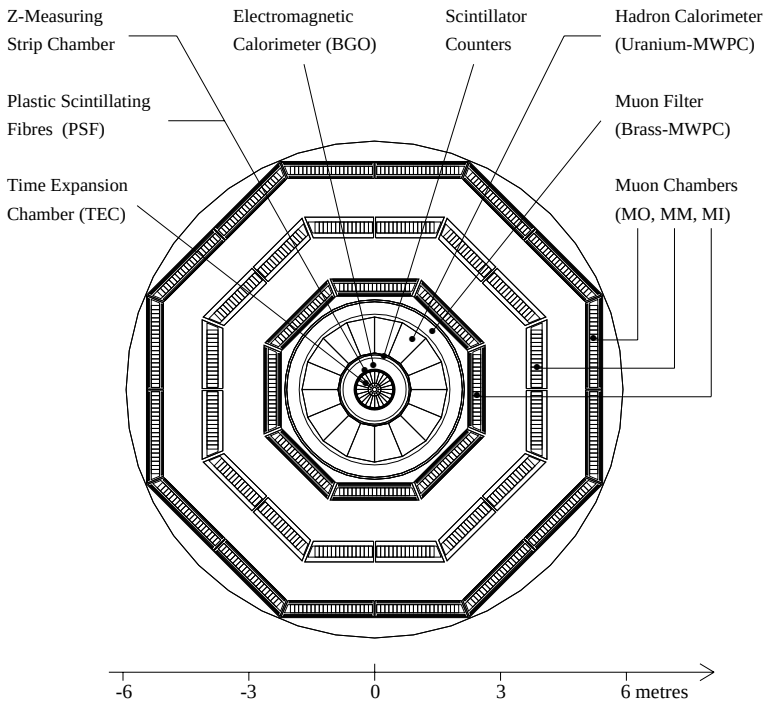

Figure 5.2: The L3 detector, as seen in the $r - \phi$ plane [9].

primary vertex position and tracks.

- Electromagnetic Calorimeter (EC) for detecting particles, which were interacting due to electromagnetic forces.

- Scintillator counters of cylindrical shape.

- Hadronic CALorimeter (HCAL) for detecting particles that are interacting via strong forces.

- Three layers of muon chambers, to detect particles, which were traversing

the tracking device, EC, and ECAL without being stopped. In many cases this particle will be identified as a muon.

At the endcaps of the detector, additional EC were installed in order to detect particles in the (very) forward regions. These detector were the

- Very Small Angle Tagger (VSAT)
- LUMInosity detector (LUMI)
- Active Lead Ring (ALR)

LUMI was used to precisely determine the luminosity at L3 (see Sec. 2.4.1). In addition, all three forward EC could be used to perform tagging studies. This work made use of the VSAT detector, for detecting the electrons from single tagged events. The sub-detectors with emphasis to the ones that were involved for the analysis of this work will be discussed in the following.

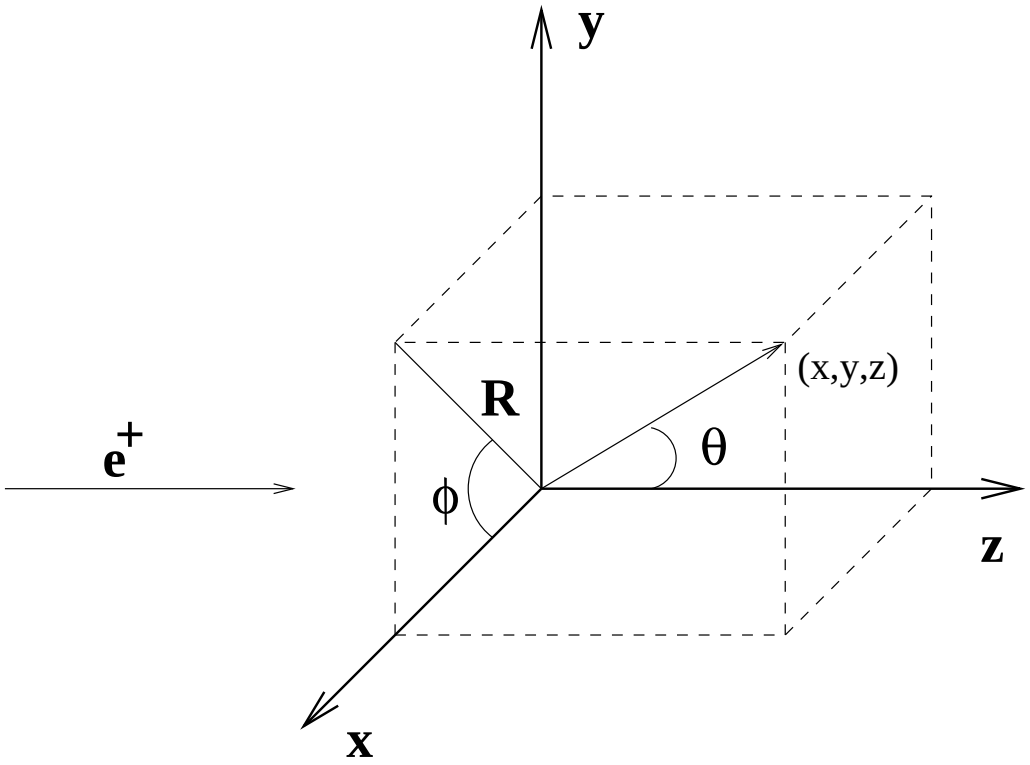

Figure 5.3: Definition of the polar coordinate system, as used with L3. The x-axis is pointing towards the center of LEP [9].

5.1 The Central Tracking Detector

The central tracking device consisted of two independently operating detectors.

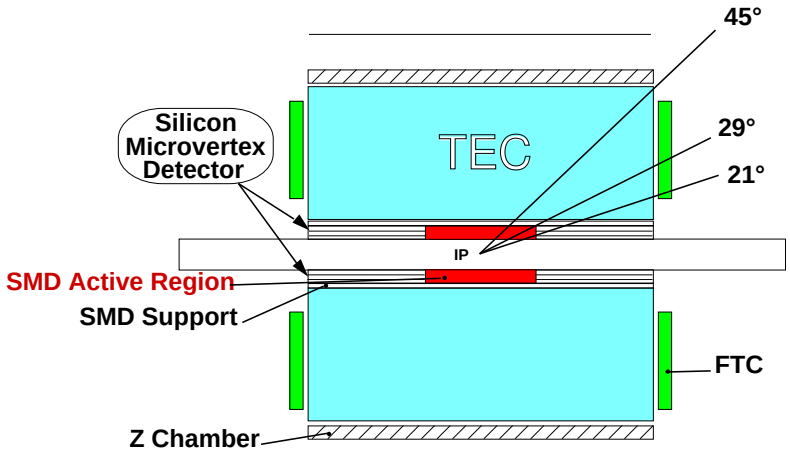

Figure 5.4: The tracking device of L3 [9].

5.1.1 Silicon Microvertex Detector SMD

The SMD was built from 2 radial layers of double-sided silicon strip detectors [35, 36] and was capable of providing $r-\phi$ and $r-z$ coordinate measurements over the polar angle range $|cos\phi| \leq 0.93$ and full azimuthal coverage. Its principal components were 0.25 cm^2 of double-sided silicon strip sensors, front end readout electronics utilizing an Application Specific Integrated Circuit (ASIC) with about 73k readout channels, a low mass mechanical support structure,

dual displacement monitoring systems, and a radiation monitoring system for detector safety. The spatial resolution for single tracks in the $r - \phi$ plane was $7\,\mu m$, and $14\,\mu m$ in the $r - z$ plane.

5.1.2 Time Expansion Chamber TEC

The TEC [37] is a gaseous drift chamber, whose drift volume is separated into two distinct parts. The parts are a drift region of relatively low electric field, with consequently reduced drift velocity, and a higher-field amplification region close to the wire, which is necessary to obtain a signal whose amplitude is large enough to be recognized by the attached readout electronics. In practice, this separation is achieved by inserting a grid of defined potential between the drift region and the sense wires [38]. The configuration of the TEC cell geometry is shown in Fig. 5.7. The anodes are alternated with focus wires, which allow for the adjustment of the track lengths, sampled by the anodes. The symmetric configuration of the TEC minimizes the electric field differences between the two drift regions. This symmetry, however, results in a left-right ambiguity for the track reconstruction. Since there are half as many sectors in the inner chamber as in the outer chamber of the TEC (Fig. 5.8), the left-right ambiguity can be resolved by matching the tracks between the inner and outer sectors. A second technique to resolve the ambiguity is to use the difference between the signals

induced by the positive ions from the gas amplification in the detection region on two grid planes on either side of the anode to determine the initial position of the avalanche.

The radial extension is 8.5 cm for the inner TEC, and 14.3 cm for the outer TEC. Each inner sector has an azimuthal coverage of 30°, a single outer sector covers 15°.

The relatively low drift velocity ($\approx 6\,\mu m/ns$) in the drift region allows for precise determination of the centroid of the time distribution of the ionized particles. An accuracy for a single wire of $56\,\mu m$ (inner), respectively $46\,\mu m$ (outer) has been achieved.

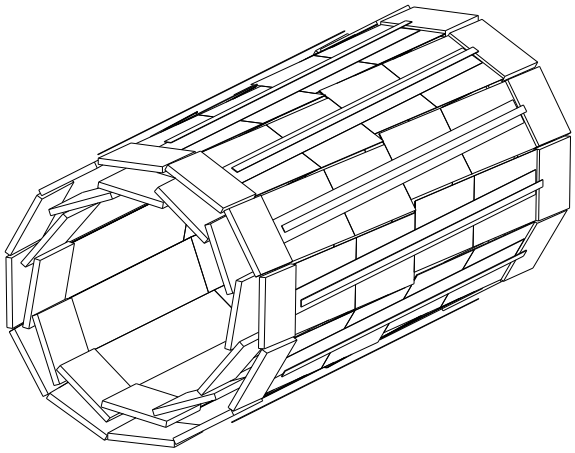

Figure 5.5: The silicon microvertex detector [9].

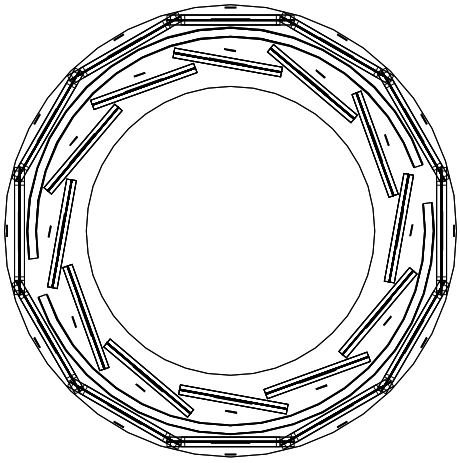

Figure 5.6: View in the $r - \phi$ plane of the SMD [9].

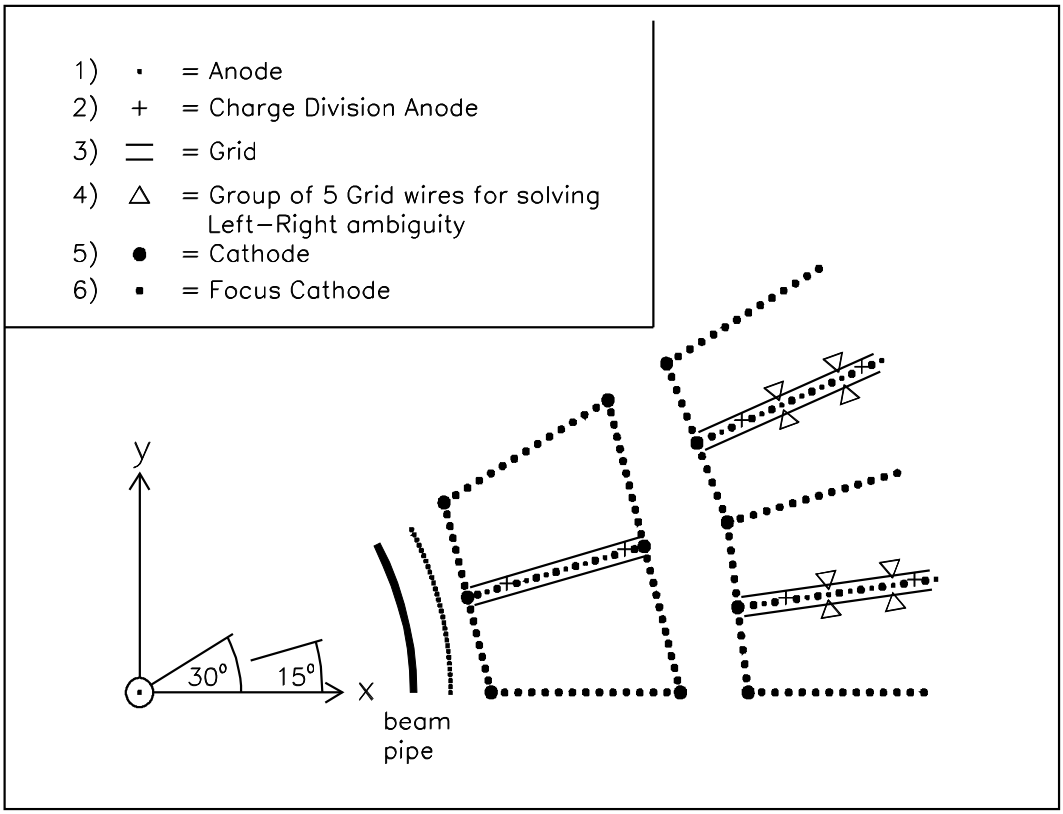

Figure 5.7: Wire configuration of a TEC cell geometry [9].

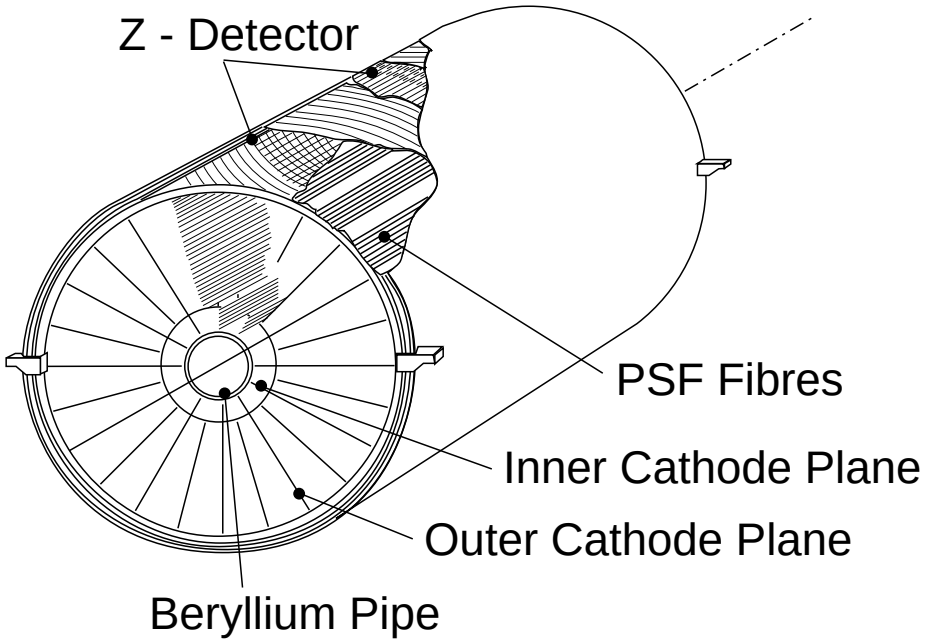

Figure 5.8: Perspective view of the L3 TEC [9].

5.2 Electromagnetic Calorimeter BGO

The electromagnetic calorimeter was designed to measure the energy and position of traversing electrons and photons. It was made out of $\approx 11,000$ crystals containing bismuth germanium oxide ($Be_4Ge_3O_{12} \rightarrow$ BGO). Each crystal was a truncated pyramid, with dimensions of $2 \times 2\,cm^2$ at top, $3 \times 3\,cm^2$ at base, and $24\,cm$ long.

The set of crystals were divided into two half barrels, with a total of 7680 crystals, and two endcaps with a total of 3045 crystals (Fig. 5.9). This arrangement provided a polar angular coverage of $|cos\,\theta| \leq 0.743$ for the barrels, and $0.788 \leq |cos\,\theta| \leq 0.978$ for the endcaps. All crystals were directed with their smaller face towards the primary vertex. A schematics of the components for an individual crystal can be seen in Fig. 5.10. The crystals were coated with a paint of high reflectivity in order to focus the light, provided by the showering particles in the medium. The focused light was then measured by a photodiode, which was glued at the backside of the crystal.

The BGO had a resolution of $\sim 5\%$ at a measured energy of 100 MeV, and 1.4% at higher energies [39].

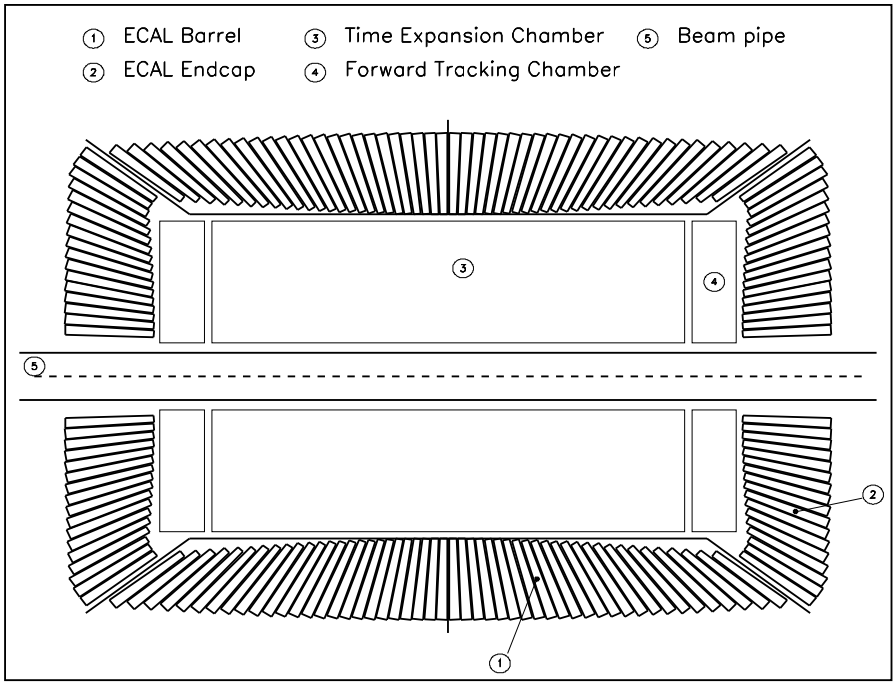

Figure 5.9: The barrels and endcaps of the L3 BGO in longitudinal cut view [9].

5.3 Scintillator Counter

Scintillator counters, made of plastics, were fast detectors for providing Time Of Flight (TOF) information [40]. They were situated between the BGO and HCAL. They covered $\sim 93\%$ of the azimuthal surface area within a polar angular range of $|cos\,\theta| \leq 0.91$. They were designed to support trigger decisions for hadronic events, as well as for discriminating dimuon events from cosmic muons,

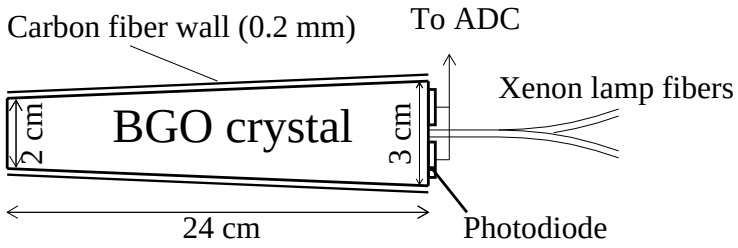

Figure 5.10: The BGO crystal with its main components [9].

which might have been passed near the primary vertex. The TOF difference for dimuons, which could have been traveling through the detector, would be almost zero, since they were supposed to be created in the primary vertex, thus traveling into opposite directions. Cosmic, single muons would have traveled through the detector along one direction, and showing a TOF difference of $\sim 6\,ns$.

5.4 Hadronic Calorimeter HCAL

The HCAL consisted, similar to the BGO, of two main parts, the barrel and the endcaps (Fig. 5.11). It was a gas sampling calorimeter, using towers of depleted uranium plates as absorber material. The signal was produced by means of

proportional wire chambers [41, 42].

The barrel calorimeter allowed to measure the energy of particles within a polar range of $|cos\,\theta| \leq 0.819$, the endcaps covered the range $0.819 \leq |cos\,\theta| \leq 0.995$. The central part of the HCAL contained nine rings with 16 modules. A total of 7968 chambers were placed in the barrel part. The two endcaps contained one outer and two inner ring. Each of the rings housed 12 modules.

The energy resolution was $\sim 13\%$ at 45 GeV.

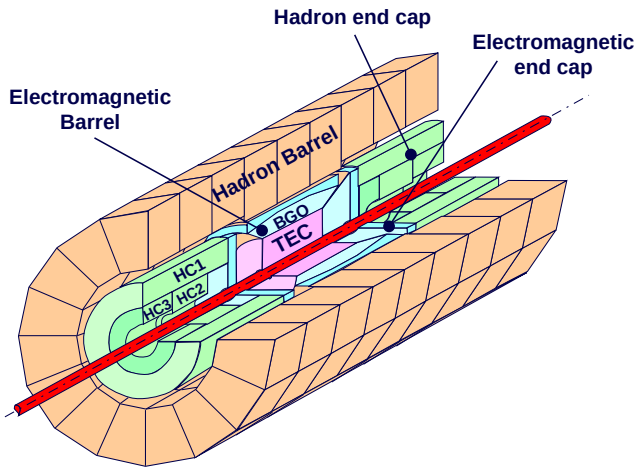

Figure 5.11: Perspective view of the HCAL modules [9].

5.5 Very Small Angle Tagger VSAT

For measurements of electrons and photons at very small angles, the VSAT detector was incorporated into the L3 detector in 1996 and began its operation during the 1997 run [43]. It consisted of four boxes with BGO crystals, two on each side of the vertex point, in the horizontal plane, Fig. 5.12. The BGO

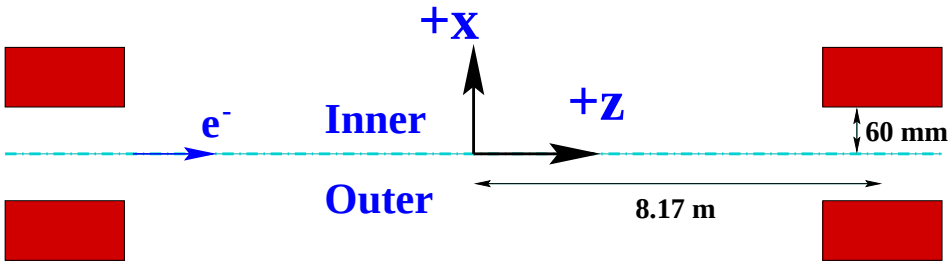

Figure 5.12: Top view of the distribution of the VSAT boxes along the beamline and its coordinate system [43].

crystals have been cut from spare EC barrel crystals to a size of $9 \times 18 \times 220\, mm^3$. At each side of the interaction point, the VSAT boxes were situated at 8.17 m, just behind the first quadrupole magnet (3.47 - 6.34 m). The quadrupole defocused the electron beams in the horizontal plane and focused in the vertical plane. Because of this magnet, the beampipe had the elliptical form and the VSAT boxes were only situated in the horizontal plane, but not in the vertical plane, Fig. 5.13. As a consequence, VSAT did only cover roughly half of the azimuthal angular range. In addition, the azimuthal angular acceptance is not

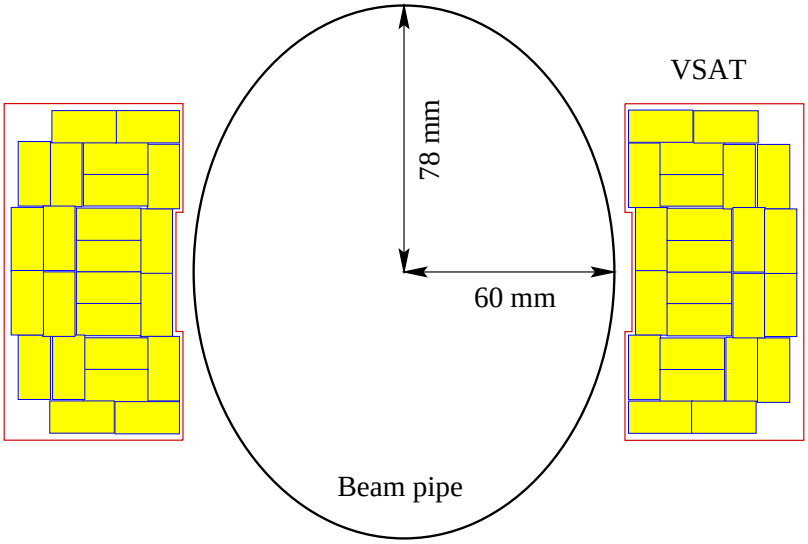

Figure 5.13: Vertical cut of the VSAT detector at one side of the vertex point [43].

linear in ϕ, but has a banana shaped form, in combination with materials in the path of particles to be detected, Fig. 5.14. The polar angular coverage was limited to 5 mrad $\leq \theta \leq$ 12 mrad respectively $\pi - 12$ mrad $\leq \theta \leq \pi - 5$ mrad.

5.6 Luminosity Monitor LUMI

The main purpose of the LUMI detector was to measure precisely the luminosity for L3 [44]. In addition, this detector could be used as a tagging device, as the VSAT.

The LUMI was a two side detector system, situated on each side of the vertex

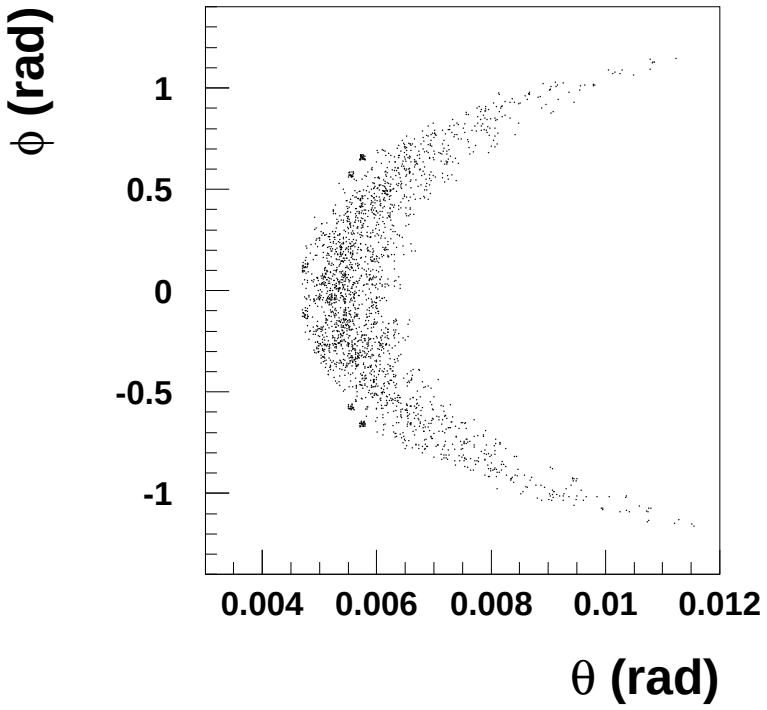

Figure 5.14: VSAT acceptance for charged particles [43].

point at a distance of about 2730 mm, see Fig. 5.15. Each calorimeter was rotation-symmetrically constructed and consisted similarly to the VSAT of a total of 304 BGO crystals. Each detector was parallel to the beam axis, covering 15 mm radially and arranged in eight rings. Azimuthally the calorimeters were divided into 16 sectors, each covering an angle of 22.4° (Fig. 5.16). In support for the luminosity measurement, the LUMI detector was complemented with a silicon strip detector (SLUM). This detector was mounted in front of the calorimeter. On each side the detector had three layers. Two layers of

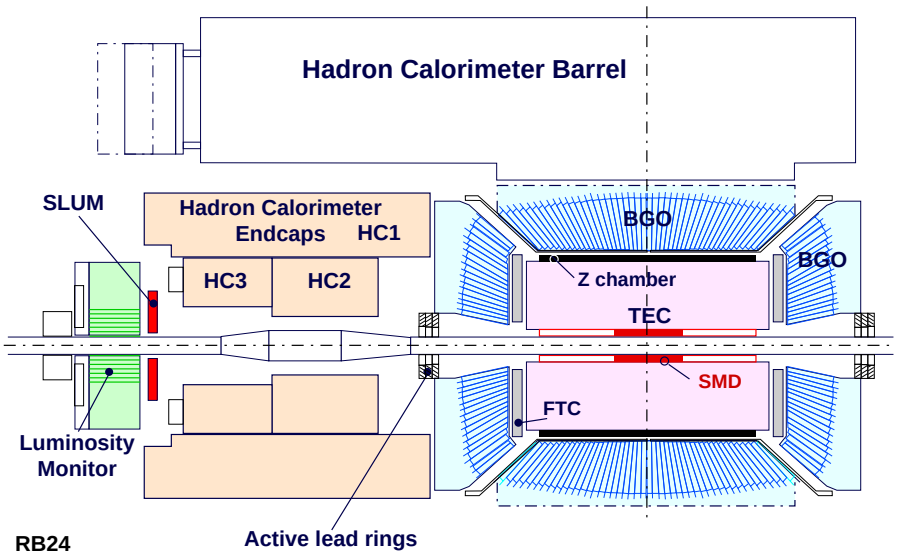

Figure 5.15: Side view of the central region of the L3 experiment on the $+z$ side, showing the beam pipe and the positions of the LUMI and SLUM detector [9].

strips were concentrically arranged with the beam axis, in order to measure the polar angle of the traversing particle. One layer of strips was arranged perpendicular to the beam axis for measuring the azimuthal angle. This allowed a determination of the absolute luminosity to a precision of 0.05%.

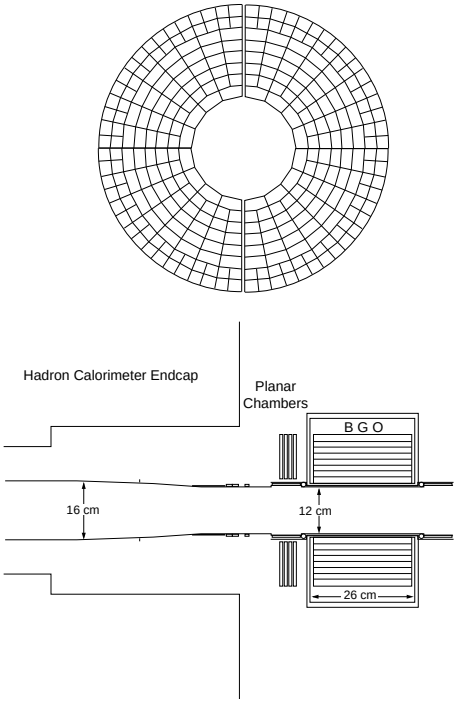

Figure 5.16: Schematic view of the LUMI detector arrangement. Upper: transverse sketch; Lower: longitudinal sketch, showing the LUMI detector around the beampipe with SLUM in front of it [9].

5.7 The Trigger System

It is quite inefficient and almost impossible to record every single event, that occurs during a collision. In order to select only events that are useful and worthwhile to process, one has to integrate a trigger system into the data acquisition system.

For the L3 detector a three-level trigger system had been implemented, and was distinguished by the simple naming scheme *level-1, level-2, level-3* [45, 46, 47]. This triggering scheme was able to reduce the event rate for a particle crossing rate of 45 kHz with a 4×4 bunch mode, or 90 kHz with an 8×8 bunch mode to several Hz for writing on tape.

The selection of a particular event was performed in three steps, each with an increasing level of information to be used.

Trigger Level 1

The trigger electronics decided with the help of the detector information, within a fraction of a second, if an interesting collision took place. If the decision was positive it started data acquisition and the trigger was said to be "fired". The trigger level-1 was a hard coded trigger, i.e. it was integrated in the detector hardware. It was a logical -OR- trigger, which means it accepted an event and started the data acquisition if ANY of the following sub-triggers responded:

- Energy Trigger: based on the amount of energy deposited in the BGO and/or HCAL. The trigger fired if the detection exceeded a certain threshold.
  - The threshold was 10 GeV for the BGO, 15 GeV in BGO and in the HCAL-barrel, or 20 GeV as the sum of all calorimeters.

  - On a single photon was triggered, if a BGO cluster was found, accounting for more than 80% of the total electromagnetic energy of the event. Since a photon is uncharged, no track should be found in coincidence with the BGO event.
  - A single tag trigger was fired, if an energy deposit of at least 30 GeV was detected in the LUMI detector. If no tracks were found, a prescaling factor 40 was used, else the factor was 1.

- Outer TEC Trigger: at least two tracks with a transverse momentum $p_T \geq 0.15$ GeV and a relative angle of $\phi > 60°$, originating from the vertex. The inner TEC trigger required at least two tracks with any configuration and operated complementary to the outer TEC trigger.

- Scintillator Trigger: at least 5 out of the 30 central scintillation counters, which had to be spatially separated, had to respond within ± 15 ns relative to the beam crossing period.

- Muon Trigger: at least one muon, detected with the muon spectrometer, with $p_T > 1.5$ GeV. In addition, a scintillator counter hit had to send a signal within ± 30 ns. This reduced the background of cosmic muons.

Trigger Level 2

Events that were preselected with the trigger level-1, underwent a more detailed analysis within the trigger level-2, based on crude information of the detector components. Energy deposits in the calorimeters were assigned crude θ/ϕ information and a fast three-dimensional analysis was performed. Another criteria was the transverse/longitudinal energy imbalances of the event. This helped to discriminate events that could have occurred due to interactions of beam particles with the beam pipe or residual gas molecules, or simply detector noise. More detailed information of the TEC, e.g. the distribution on the charge division wires could help to decide on vertex recognition.

The second level of the trigger system also recorded every 20th event, that it was supposed to reject, in order to estimate a trigger inefficiency at this level.

Trigger Level 3

The third trigger level had access to the complete set of digitized data. Based on sophisticated software algorithms, events were selected or rejected based on correlations of the energy deposits in the calorimeters, reconstruction of muon tracks, or reconstruction of the vertex.

Chapter 6

Data Analysis

The data sample, which was used for this analysis, was taken with the L3 detector between 1998 and 2000. Each year, the c.m.s. energy $\sqrt{s}$ was by and by increased. The integrated experimental luminosity was

$$\begin{aligned} \text{for the year 1998: } \mathcal{L} &= 170.3\,pb^{-1} \text{ with } \sqrt{s} = 189\,GeV. \\ \text{for the year 1999: } \mathcal{L} &= 219.4\,pb^{-1} \text{ with } \sqrt{s} = 192 - 202\,GeV. \\ \text{for the year 2000: } \mathcal{L} &= 210.5\,pb^{-1} \text{ with } \sqrt{s} = 205 - 208\,GeV. \end{aligned}$$

The total integrated luminosity for the data sample used, was $\mathcal{L} = 600.2\,pb^{-1}$. In order to compare experimental data and predictions for them, several MC samples were produced, both, for describing the data of interest and possible sources of background.

The generated MC samples were subject to reconstruction, i.e. they were passing through a full detector simulation. The reconstructed MC samples were then processed in the same manner as the experimental data, i.e. they were subdued identical selection criteria. Since the MC samples were produced according to a luminosity, which was a multiple of the integrated luminosity of the experimental data-sample, the MC-luminosity was afterwards normalized to that of the experimental.

Events, which were taken with the L3 detector as well as the reconstructed MC events were processed according to the process, sketched in Fig. 6.1.

This process for two-photon analyses was threefold:

1. Data acquisition (DAQ) → raw events.

2. Data reconstruction → `REL3`.

3. Physics analysis

   - Data reconstruction according to $\gamma\gamma$ reactions → `GGDVN`.
   - Data reconstruction according to selected analyses → individual routines, e.g. `EPTAG`.

The `REL3` reconstruction was performed in order to convert raw signals from DAQ into objects, that can be managed. This means, that raw data were

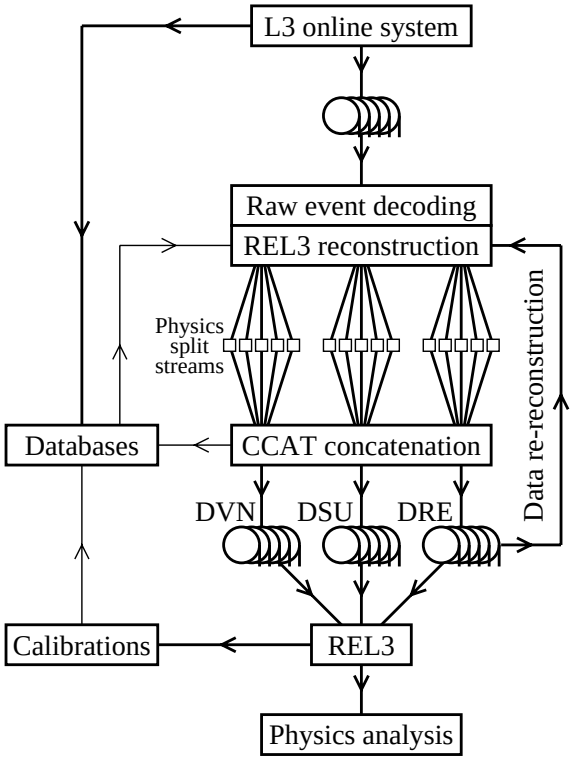

Figure 6.1: Schematic sketch of the data flow procedures in L3 [9].

reconstructed and processed into higher level objects, for instance,

- pulse heights of the BGO crystals were assigned an energy value using the absolute energy calibration of dedicated $Z^0 \rightarrow e^+e^-$ runs;

- a kinematic fit was used to derive the track momentum and direction from the hits of the central tracking detector.

These objects were stored in a Data "aVaNti[1]" format (DVN) [48]. This data type can be used for fast feasibility studies, but has to be processed further in order to perform more sophisticated analyses, since the data type is yet unhandy. Furthermore, the data set has to be reduced for selecting the interesting events, both, for experimental and MC data. Many events are still in a premature stage, since physical constraints, which determine the events to be selected, cannot be applied yet and the amount of data is too large to perform meaningful analyses.

The routine `GGDVN` (for Gamma-Gamma DVN) processed the objects into variables, that can be used for analyzing events onto an even higher level. The objects after this process were tailored for analyzing two-photon events and distributions of events can be easily uncovered, e.g. with the Physics Analysis Workstation (PAW) [49].

Preselections were performed in two steps, for determining single tag events with two tracks. These steps, performed with `GGDVN` and `EPTAG` [2] were

1. `GGDVN` $\rightarrow$ high level objects (`EPIO` format [50]) and preselections according to $\gamma\gamma$ events with at most four tracks in the final state and a total of particle objects, not exceeding 6. This preselection assured that almost

[1]Italian expression: 'go ahead'.

[2]Fortran routines, commonly used for tagged two-photon analyses with L3.

all of the dimuon events were selected and hadronic interactions were rejected.

2. `EPTAG` → detailed selections, with decisions on tagged events and two muons in the final state.

The criteria for preselecting single-tagged events, with dimuons in the final state were:

a) A limited total energy registered by the BGO calorimeter, E_{BGO}, and the HCAL calorimeter, E_{HCAL}

$$E_{BGO+HCAL} \leq 50\,GeV$$

b) A clean environment in the tracking chambers

$$\frac{N_{tracks}}{N_{raw\ tracks}} \geq 0.2$$

The former cut rejected faking signals due to Z-boson production, where two electrons with high energy deposit in the calorimeters could be observed.
The number of tracks in a premature selection state (raw) should not exceed a certain value. This reduces the background due to spurious tracks, mainly occurring because of beam-gas interactions and low energy events.

6.1 Event Selection

The calorimeter detector VSAT was used to recognize events in a very small kinematic region. The VSAT had a polar angular acceptance of $5\,mrad \leq \theta \leq 12\,mrad$, and accordingly for the other side of the vertex position. The range for the squared four-momentum transfer was

$$0.2\,GeV^2 \leq Q^2 \leq 0.85\,GeV^2$$

Since the VSAT was in the very vicinity of the beampipe, and additionally affected by the quadrupole magnet close to it (Sec. 5.5), the selections for VSAT were performed in a different way as compared to previous analyses with LUMI as the tagging detector [51].

The signature for dimuon events stemming from single tagged two-photon reactions is an energy deposit in one of the forward calorimeters and two well measured tracks, of which at least one has to identified as a muon.

After carefully selecting events with the proper signature, several corrections have to be applied. In an ideal case, each occurring physical event will be recorded. This requires the triggers to be working with an efficiency of 100%, i.e. the triggers should always "fire" if the produced particles are traversing the detectors. In reality this is not the case. Due to imperfections of the triggers on a time dependent basis the one or other event of interest will be lost. The

trigger efficiency has to be studied, in order to estimate the fraction of losses due to improper activation of the triggers.

Events that might fake the single-tagged two-photon events have to be treated as background. Although the selection cuts are rather tight, there is no guarantee that all selected events belong to the category of the events under consideration. A careful analysis of possible background sources has to be performed with appropriate MC generators, which produce events according to the possible background topology. These events will be handled in the same way as it was done for the MC generator of interest and data, i.e. they were passed through a full detector simulation and the same selection criteria were applied on them.

Eventually one obtains the distributions for the events under consideration with

$$N_{physical} = \frac{N_{data} - N_{background}}{\varepsilon_{trigger}}$$

where N_X is the number of events according to its physical nature and $\varepsilon_{trigger}$ is the estimated trigger efficiency.

6.1.1 VSAT Selections, Single Tag Events

For determining the single tag event, one of the beam particles has to be scattered such, that it will be detected with VSAT. This in turn means that exactly

one single-tag flag with $0.5 \times E_{beam} \leq E_{VSAT}$ has to be detected. This selection is necessary in order to discriminate events, where the detected, high energetic electron or photon[3] could stem from a Z^0 decay. Since the event under consideration is a single tagged event, no other high energetic electron had to be detected in one of the other calorimeters[4].

The VSAT detector was capable of tagging electrons in the kinematic range $0.2\,GeV^2 \leq Q^2 \leq 0.85\,GeV^2$. Since the VSAT did not perform well in energy measurements for the scattered electron, the energy and the quantity Q^2 was evaluated with the information of the tracks.

By measuring the electron and the two muons, the kinematics is constrained. Using the conservation of energy and longitudinal momentum, one can determine the energy of the tagged electron with

$$E_{tag} = \frac{p_{\mu^+\mu^-} \cos\theta_{\mu^+\mu^-} + (2E_{beam} - E_{\mu^+\mu^-}) \cdot (\pm 1)}{\pm 1 - \cos\theta_{tag}} \tag{6.1}$$

where $p_{\mu^+\mu^-} = |\vec{p_{\mu^+}} + \vec{p_{\mu^-}}|$ and $E_{\mu^+\mu^-} = E_{\mu^+} + E_{\mu^-}$. The factor ± 1 stems from the fact, that the second electron is considered to be scattered with $\theta \sim 0$, respectively $\theta \sim \pi \rightarrow \cos\theta_{untag} \sim \pm 1$.

[3]The central tracking devices were not in the angular acceptance region of the VSAT, so that no momentum information for the VSAT events were available.

[4]Due to the vicinity to the beampipe, off-momentum electrons could fake a single or even a double tagged event. However, due to the full kinematic information for the full event, it could be identified.

Since the momentum of the two muons was rather well measured with the TEC, the photon virtuality Q^2 and hence the Bjorken-x can be expressed with the track information of the two muons. The transverse momenta of the two tracks can be used to determine the squared four-momentum transfer to the highly virtual photon. With kinematics's considerations and conservation of momentum, one obtains the virtuality of the photon

$$Q^2 = (\vec{p}_{T,1} + \vec{p}_{T,2})^2 \tag{6.2}$$

where $\vec{p}_T$ is the transverse momentum, measured with tracks.

With this information and the measurement of the invariant mass of the dimuon event, one can determine the Bjorken-x variable according to

$$x = \frac{Q^2}{Q^2 + W_{\gamma\gamma}^2} \tag{6.3}$$

where $W_{\gamma\gamma} \equiv W_{\mu\mu}$. Since the squared four-momentum transfer to the target photon is assumed to be ~ 0, (6.3) differs from (2.11) only by the term P^2, because $P^2 \equiv 0$.

6.1.2 Dimuon Events

In order to select only events, which are having two muons in the final state, one has to account for events, which can be allocated to muons. This means, no photon or hadron has to be seen in the detectors. A photon is identified with

a BGO deposit, but without any associated track; a hadron is identified with BGO/HCAL deposit and associated track.

For selecting two muons in particular, the number of well measured tracks must be exactly two. Since the muon pair stems from a photon, which is not electrically charged, a requirement is $\Sigma q_{track} = 0$, where the charge q_{track} is determined from the curvature of the tracks. The muons, which will reach the more distant sub-detectors, need to have a minimum energy. In addition, a large background exists for low invariant masses, which is hard to distinguish from dimuon events. Thus only events with $1.7\,GeV \leq W_{\gamma\gamma}$ will be selected. From the two well mea-

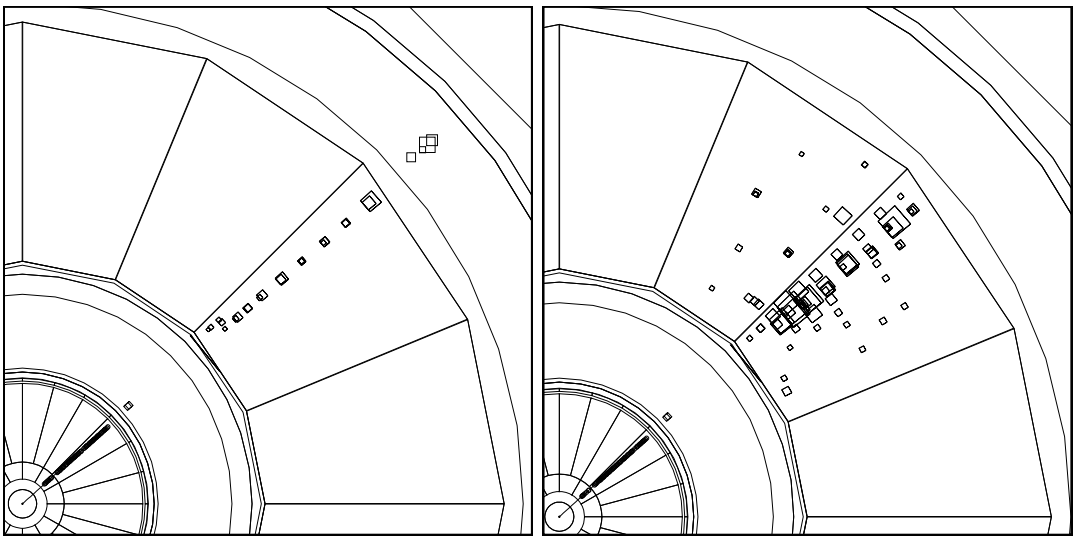

Figure 6.2: Cross-sectional view of an event display from L3. The left plot shows energy deposits in the TEC, BGO, and HCAL (from inner to outer), released by a muon. The right plot shows the same, but for a pion [9].

sured tracks at least one has to be identified as a muon. This relaxed cut ensures an efficient uniform selection in the angular range of dimuon events, since the tracking devices do not cover the whole solid angular range.

The identification receives difficulties since pions, which appear as minimum ionizing particles (MIP) in the BGO, have to be discriminated. This can be achieved with searches of activities in the BGO and HCAL and the following selection cuts:

1. $E_{BGO} \leq 0.4\,GeV$, since a muon is an MIP.

2. $E_t/p_t \leq 0.6$, with $E_t = E_{BGO} \cdot \sin\theta$ and p_t being the transverse momentum w.r.t. the beam direction. This selection cut discriminates against electrons, which will deposit most of their energy in the BGO. It will partially also discriminate against pions, which interact also due to strong forces, but behave as MIPs within the BGO.

3. $HCHIT \geq 0.5$, with HCHIT being the number of hits in the HCAL, normalized to the one expected for a MIP. This in turn means, the track has to have an associated hit with BGO and HCAL. Since the muon is a MIP also for HCAL, this selection will discriminate against pions, which most likely deposit all their energy within the HCAL. The latter selection can be illustrated with Fig. 6.2.

4. Acoplanarity angle: $\phi_{aco} = |\pi - (\overline{\phi}_{tracks} - \phi_{VSAT})| \leq 0.5\,rad$. The angle $\overline{\phi}$ indicates the resulting azimuthal angle, which is obtained from the two tracks, i.e. the two muons. This selection reduces most background due to coincidences with faked single tagged electrons and two leptons in the final state. Since transverse momentum is conserved, the tagged electron and the dimuon system will have directions of flight, which are opposite to each other in the azimuthal plane.

5. The acceptance of the tracking device is limited to $26^o \leq \theta_{track} \leq 154^o$, which corresponds to $|\cos\theta_{track}| \leq 0.9$.

The requirement for selection cut 1. can be seen in Fig. 6.3. The electron will deposit its full energy in the BGO, whereas the muons will release only a fraction of its energy in the BGO, according to an MIP. In the lower part of Fig. 6.3 the appearance of both type of particles in the data sample can be clearly seen.
The selection of events according to cut 1. and cut 2., and the fact that electrons will rarely reach the HCAL allows to effectively reject events with electrons as dileptons in the final state. Selection cut 2. can be illustrated with Fig. 6.4. In order to discriminate the pions from muons, the information of the HCAL were taken into account. A muon shows characteristics of an MIP in the BGO, as well as in the HCAL. The pion shows similar characteristics in

the BGO only, but most likely releases its remaining energy in the HCAL. This will lead to a broader shower appearance in the HCAL, which can be used in addition to the total detected energy in the HCAL. One can assign a probability (named *HCHIT*), if the detected particle has MIP characteristics. Fig. 6.5 shows the distributions for pions and muons. Pions were predominantly measured in a region of probability of < 0.5, whereas the major fraction of muons were measured with a probability of ≥ 0.5. This selection cut ensured that most of the pions were removed from the data sample.

Selection cut 4. is necessary in order to remove events due to fake signals, either as fake signals that are appearing as single tagged electrons in the VSAT or due to wrongly identified tracks. There must be, due to kinematic constraints a correlation between the azimuth of the measured VSAT event and the resulting azimuth of the tracks, see Fig. 6.6. Since the VSAT is so close to the beam-pipe, in conjunction with the close by quadrupole magnet a large unidentified background appeared in the VSAT detector, which was caused most likely by off-momentum beam electrons. Fig. 6.7 shows for data an overwhelming peak around $\phi \sim \pi$, which cannot be seen with the simulated events.

The tracking device was limited in polar angle acceptance. The limitation was worsened due to the correlation of tracks with BGO activity in the selection of events. The BGO had acceptance gaps between the barrel and endcap regions,

which covered the TEC region of $|\cos\theta| \sim 0.8$. Furthermore, the TEC was limited due to its edges in the region $|\cos\theta| \simeq 0.9$, which can be seen in Fig. 6.8. The selection cut 5. was introduced to account for that. The resulting distribution can be seen in Fig. 6.9.

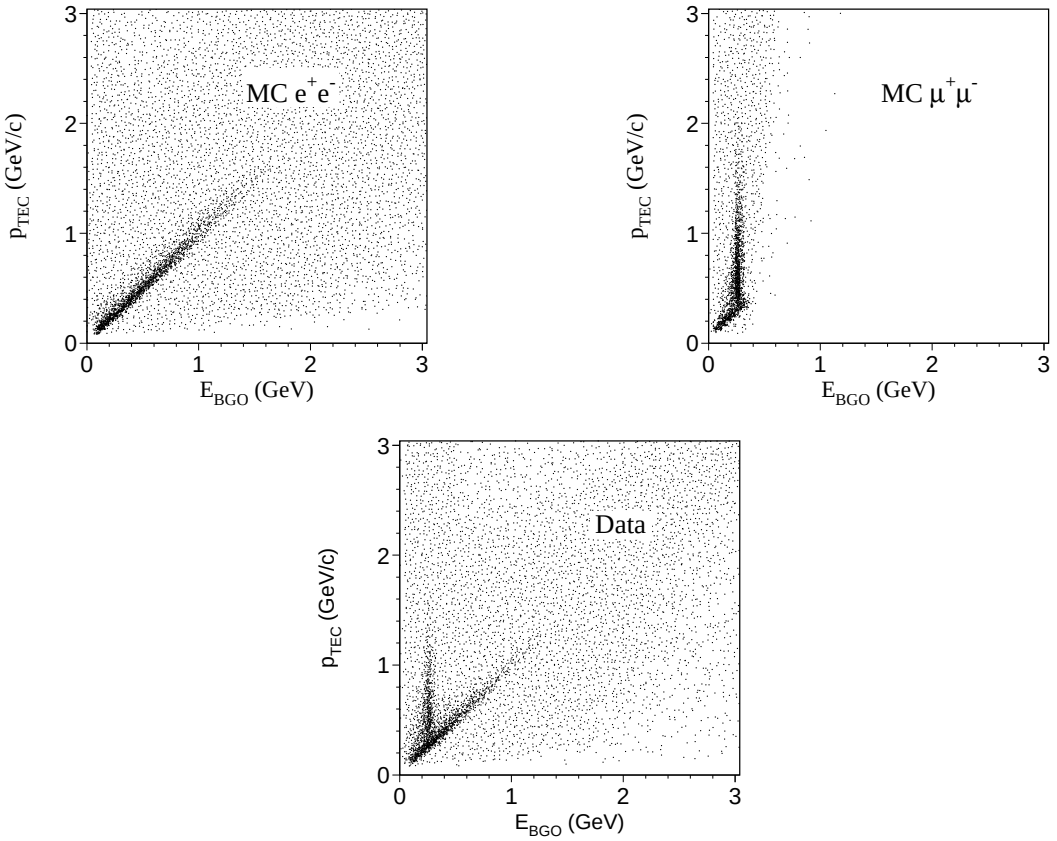

Figure 6.3: Correlation between the momentum measured with TEC and deposited energy in the BGO calorimeter. Upper left: for electrons; upper right: for muons; lower: for the data sample, which contains both, electrons and muons.

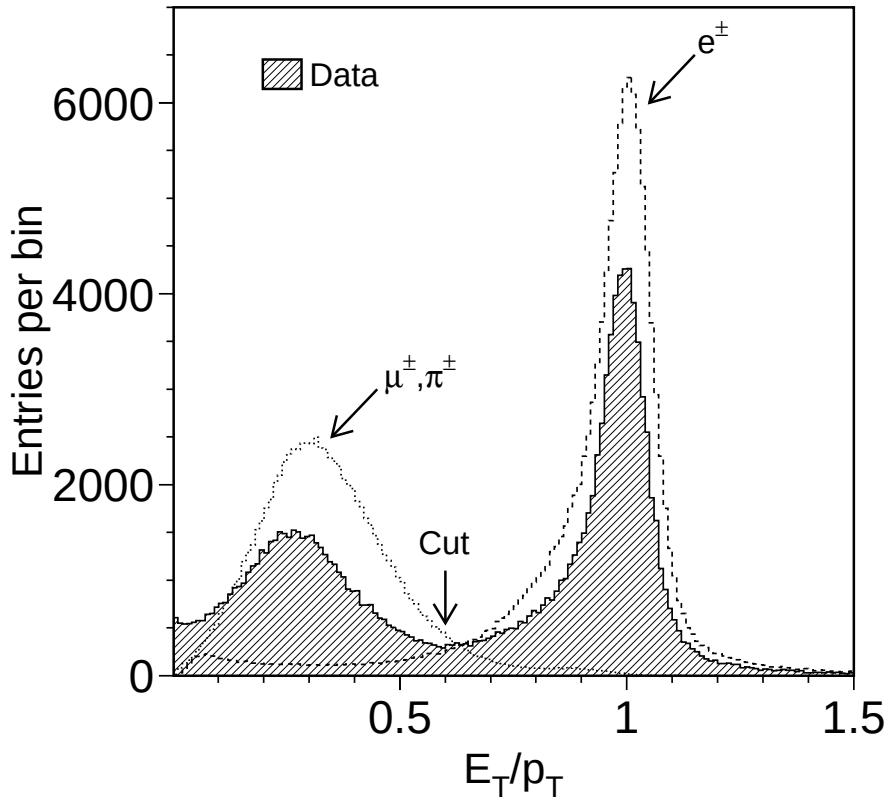

Figure 6.4: Ratio of the transverse energy, released in the BGO to the transverse momentum, measured with TEC.

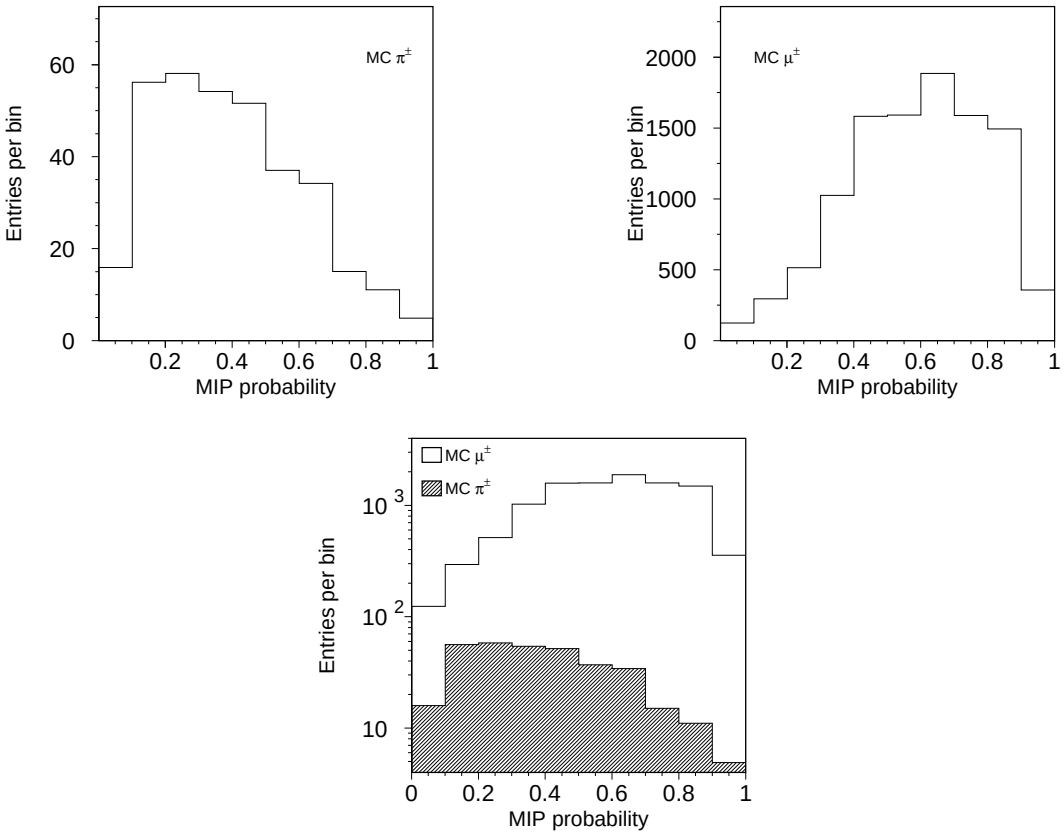

Figure 6.5: Probability of being an MIP, measured with the HCAL detector. Upper left: for pions; upper right: for muons; lower: superposition of pions and muons, normalized to the generated luminosity.

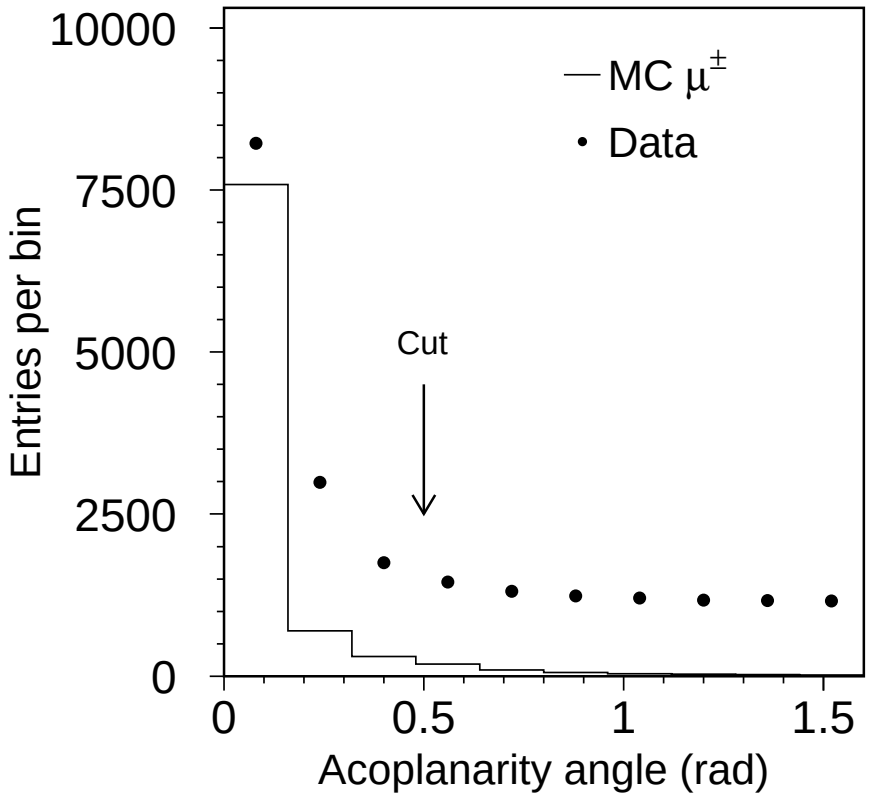

Figure 6.6: Acoplanarity angle, measured with VSAT and TEC.

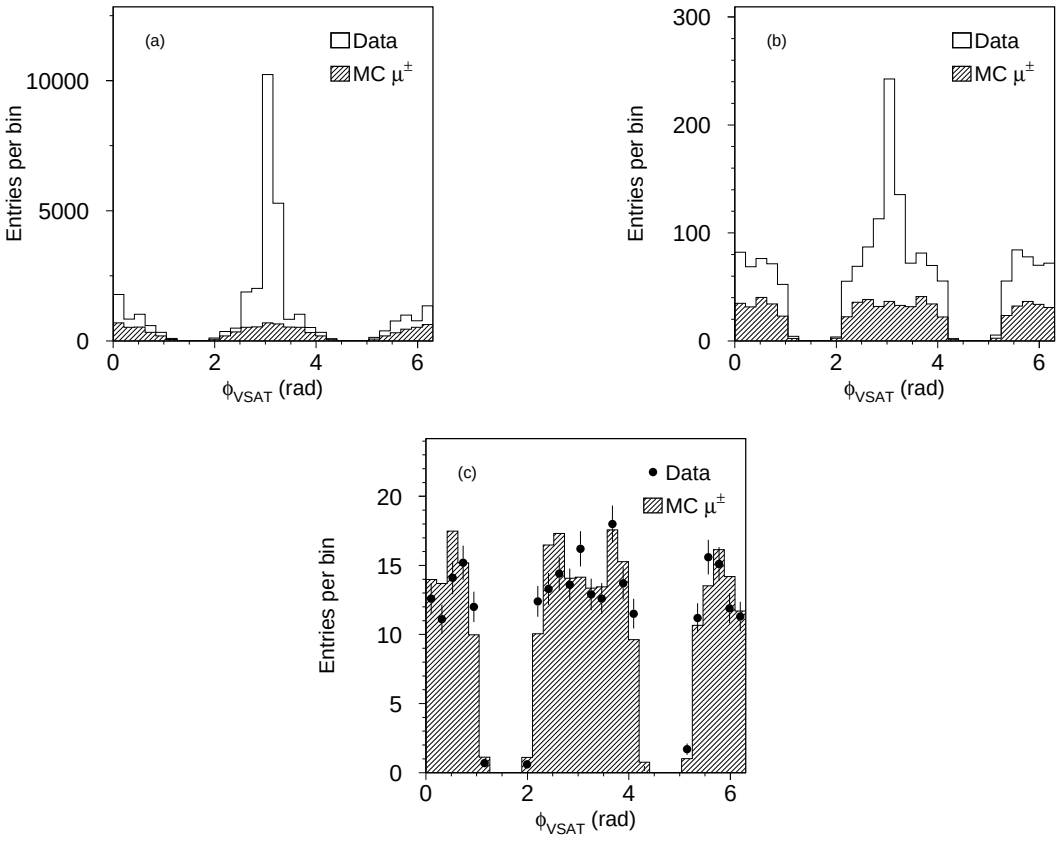

Figure 6.7: Azimuthal distribution as measured with the VSAT. (a) before selection cuts; (b) selection of $W_{\gamma\gamma} \geq 1.7\,GeV$; (c) selection of $\phi_{aco} \leq 0.5\,rad$.

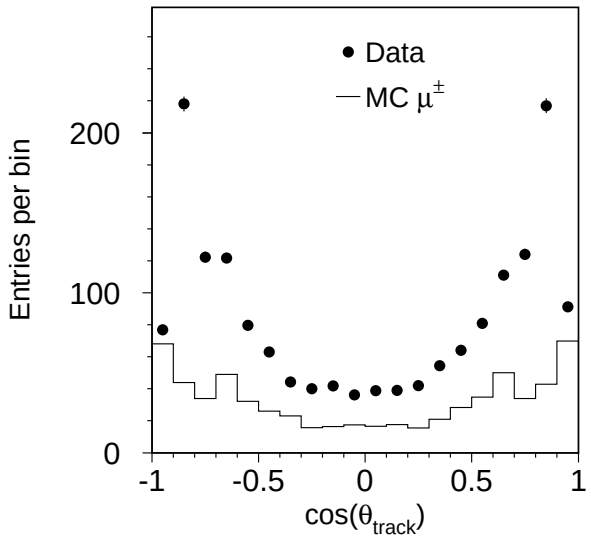

Figure 6.8: Polar angular distribution of tracks, measured with TEC.

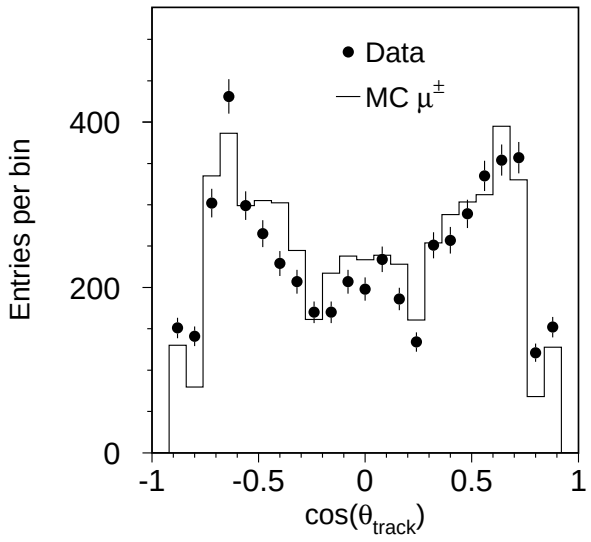

Figure 6.9: Polar angular distribution of tracks, after selection cuts.

6.2 Trigger Efficiency

The trigger system, which was used within the L3 experiment, was discussed in Section 5.7. In this section the application of the trigger bits, as they were recorded with the data will be discussed.

Every event has to be triggered at least by one of the triggers and the data were assigned the respective trigger bit(s). This means, that every event has the information, which of the triggers were "fired" and thus responsible for recording the event. The information was simply setting the corresponding trigger bit to one, if the trigger was active, else zero. Table 6.1 shows the available trigger bits.

Only a set of the available triggers were used and was dependent on the particular analysis. For the present work the trigger bits 2, 6, and 8 were the relevant triggers, which are supposed to be "fired". The events, having two tracks/muons in the final state, would require the tracking triggers and muon related triggers to become active. Since the trigger bit 7 required to identify a muon based on the muon chambers, this trigger was not relevant for this analysis. The trigger with code 2 was a complementary trigger to the TEC trigger.

For the ideal case, every trigger would become active if the corresponding requirement for activating the trigger becomes applicable. However, in practice

Bit Code	Trigger description
1	Level 0 muon trigger
2	Inner TEC trigger
3	Forward/Backward muon trigger
5	Prescaled LUMI (single tag)
6	Scintillator for muon trigger coincidence
7	Muon trigger
8	TEC trigger
9	Level 0 energy trigger
10	Fast lumi trigger , flagging only
11	LUMI trigger
12	Scintillator multiplicity trigger
13	Beam gate
14	Cosmic trigger
15	Energy trigger

Table 6.1: The various triggers, which were used to record data with L3 and their corresponding code.

no system works perfect, and so does the trigger system. Among others, dead times, noise, or faulty equipment in the worst case will influence the triggers to "fire" or not. The various triggers, which initiated recording an event, can be used to estimate the efficiency of these triggers.

The trigger efficiency can be estimated when comparing the number of events, where one particular trigger "fired" in comparison with another independent trigger, which might have "fired" or not:

$$\begin{aligned} \varepsilon_A &= \frac{N_A}{N_{selected}} \\ \varepsilon_B &= \frac{N_B}{N_{selected}} \\ \varepsilon &= \varepsilon_A \cdot \varepsilon_B \end{aligned}$$

where the index A, B indicates the independent trigger, and $N_{selected}$ corresponds to the total number of selected events.

The trigger efficiency can be also expressed in a more convenient way, which solely use the trigger information itself:

$$\begin{aligned} \varepsilon_A &= \frac{N_{both}}{N_{both} + N_B} \\ \varepsilon_B &= \frac{N_{both}}{N_{both} + N_A} \\ \varepsilon &= \varepsilon_A \cdot \varepsilon_B \end{aligned} \tag{6.4}$$

The term N_{both} indicates the number of events, where both triggers were "fired" simultaneously. One can see that the efficiencies will become 1 if only the cor-

responding trigger contributes to the selection of the events. If the concurrent trigger contributes to the selection, the efficiency will drop down. This kind of estimation allows to perform a more detailed trigger study, based upon the information of a set of trigger bits only. The procedure can be enhanced to more than two independent triggers, by means of accumulating the various trigger bits and treating them according to (6.4).

Channel	Trigger Bit	Fraction in %
$ee \rightarrow ee\mu\mu$	1	18.5
	2	55.2
	3	5.2
	6	96.8
	7	14.6
	8	80.8
	15	2.8

Table 6.2: Fraction of events that were recorded due to the various triggers. All other triggers had negligible contributions to the event recording. The most abundant triggers, Bit 2, 6, 8 were used to estimate the trigger efficiency.

The contribution of the various triggers can be seen in Figs.6.10 and 6.11. During the runtime of L3, several time slots occurred, where detectors and triggers

showed instabilities. These time slots were identified and data taken during these slots were excluded from the analyzed data sample. The mean trigger efficiency for the years 1998 to 2000 was found to be $\varepsilon = 96.5 \pm 0.1\%$. For

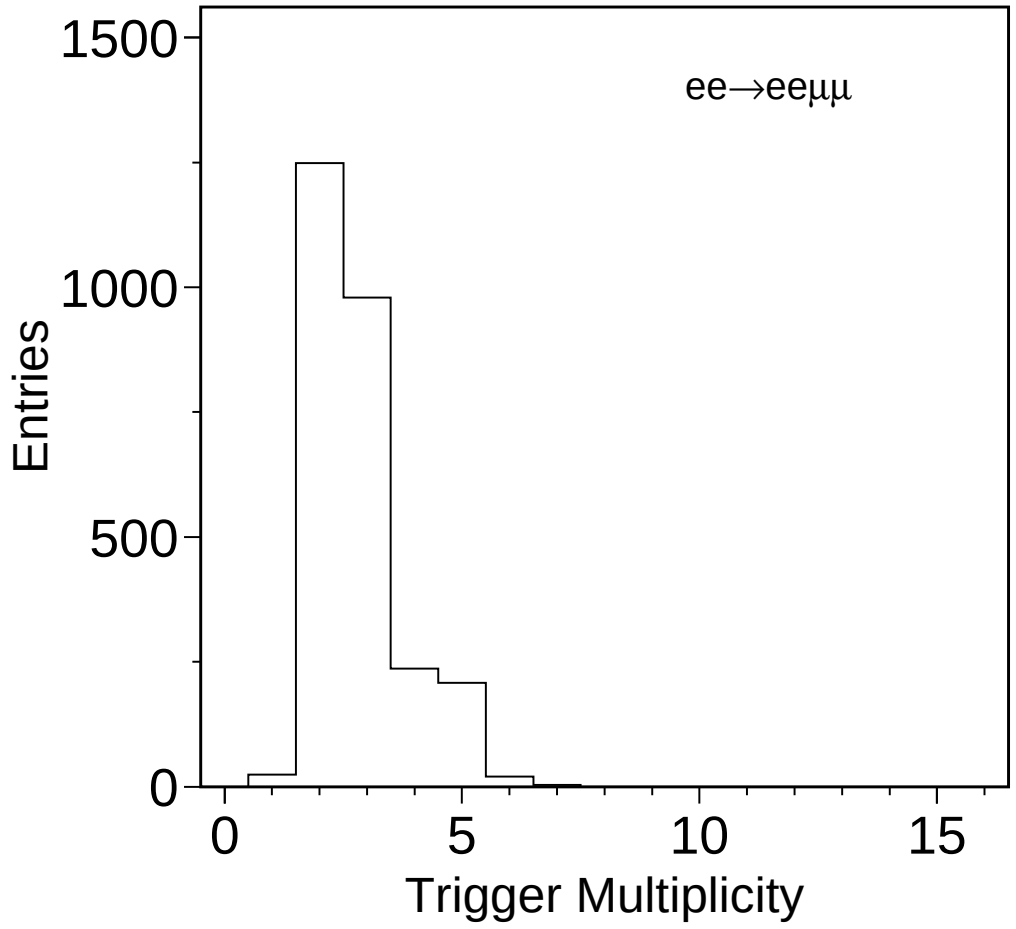

Figure 6.10: The contribution of simultaneous trigger hits for recorded events.

the MC sample no simulation of the trigger was attempted, so its efficiency was

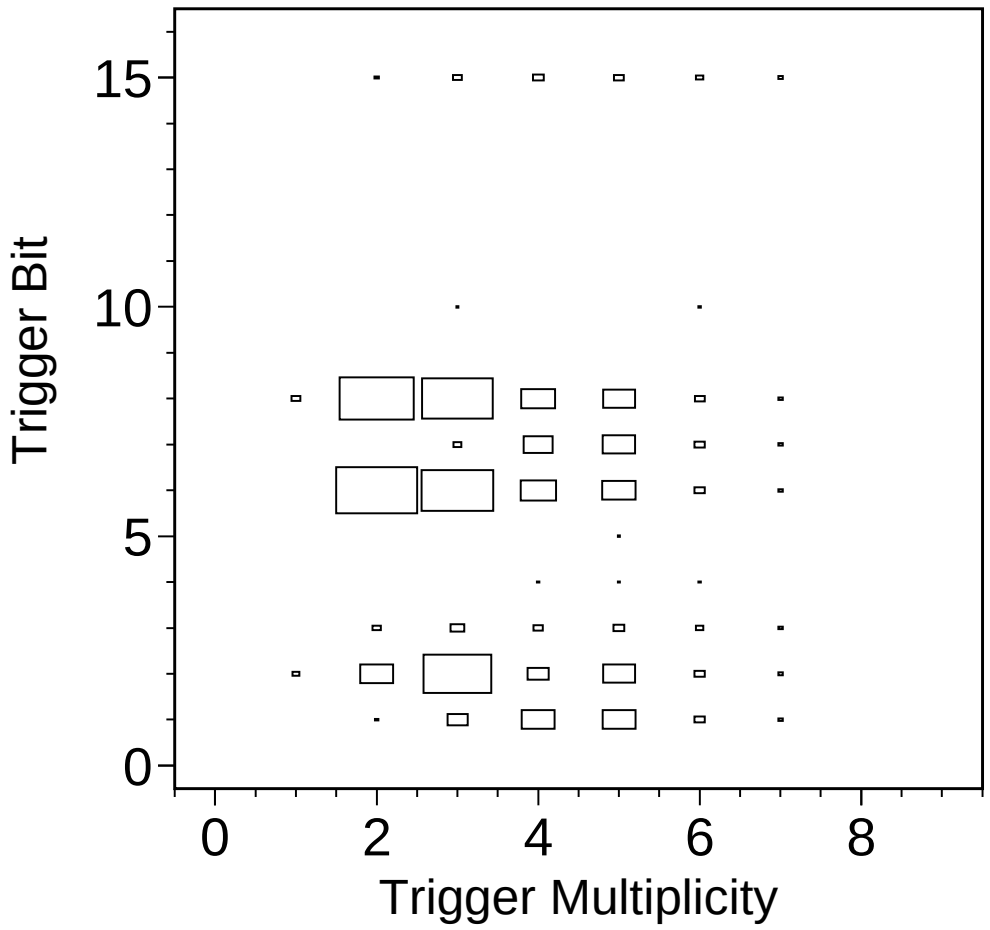

Figure 6.11: The contribution of various trigger combinations for recorded events.

100%.

In addition to the trigger level 1, there existed two additional trigger levels, which used more sophisticated analysis algorithms in order to preselect interesting events on a higher level.

The trigger level 2 kept every 20th events (i.e. 5%), which it was supposed to reject. This was done in order to estimate possible trigger losses and thus trigger inefficiencies on the second level.

For the selected data sample the number of those preselected events was zero, so that the trigger inefficiency on the second level can be assumed to be 100%. The same procedure and outcome applied to the third trigger level.

6.3 Background in Selected Events

Several sources of physical events, which are not connected to the topology under consideration, may introduce a background in the event selection. These sources have to be identified and have to be subtracted. Mainly the following sources are prone to contribute as background:

1. $e^+e^- \rightarrow e^+e^-l^+l^-$ $(l = e, \mu)$, which are originating from processes other than the multiperipheral process: bremsstrahlung, annihilation, and conversion (see Fig. 3.1).

2. $e^+e^- \rightarrow e^+e^-q\bar{q} \rightarrow hadrons$ (mainly pions).

3. $e^+e^- \rightarrow e^+e^-e^+e^-$.

4. $e^+e^- \rightarrow e^+e^-\tau^+\tau^-$.

Different dedicated MC generators have been used in order to simulate those background events.

The processes for background source 1. were generated and the cross-section was estimated to be $\sigma = (0.736 \pm 0.018) \times 10^{-3}\, nb$. In addition to the very small cross-section, the tag conditions highly suppressed the background due to bremsstrahlung, annihilation, and conversion, so that effectively no event survived the selection cuts.

On the preselection stage, only events with at most four tracks and a total number of particle objects, not exceeding 6 were required to select $\gamma\gamma$ events. The preselection allowed only $\sim 0.15\%$ of events according to background source 2. to pass through the filter. With the further selection steps applied, no event survived.

The selection cut $E_t/p_t \leq 0.6$ and the requirement of recorded activities in the HCAL were responsible for effectively inhibiting events, where the muon in the final state could be misidentified due to an electron. Since the major fraction of electrons are distributed according to $E_t/p_t > 0.6$ (see Fig. 6.4) and rarely make it to the HCAL, no event survived the selection cuts.

The background source 4. contributed a fraction of $\sim 0.3\%$ w.r.t. the data sample. τ-leptons decay after a very short time period $\sim 0.3\,ps$ into a large variety of particles. The hadronic decay modes are strongly suppressed in the same way as described above for background 1. For the leptonic decay modes, where the τ's are decaying into electrons and neutrinos, are inhibited in the same way as described above for background source 2. The estimated generated cross-section was $(4.731 \pm 0.097) \times 10^{-1} nb$. After applying the preselection cuts for limited total energy registered with the calorimeters and selecting single tags with VSAT and two tracks, $\sim 2\%$ of the τ-background sample events were left. The selection due to the acoplanarity angle removed a further large fraction

of this background. This happens mainly because of momentum conservation, since the decay is accompanied by particles, which can not be detected within the detector volume: neutrinos. Since those particle carry a fraction of the momentum of the τ-leptons, the momentum conservation cannot be observed for dilepton events. Figs. 6.12, 6.13 show the effect of the reduction steps and the background fraction w.r.t. the data sample.

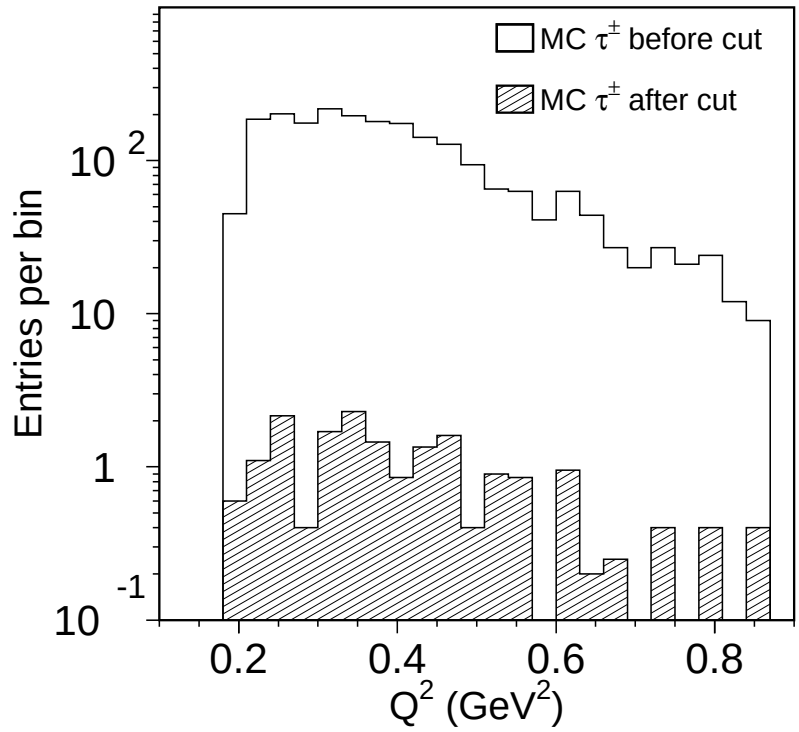

Figure 6.12: The effect of selection cuts for the background due to $e^+e^- \rightarrow e^+e^-\tau^+\tau^-$.

Due to the stringent cuts applied for the selection of events, none of the above mentioned background sources give a significant contribution to the event selection. Mainly the selection cuts for identifying muons leave no space for electrons or hadrons to be misidentified as muons.

After investigating the background sources, no event "survived" the selection rules for 1., 2., 3., and only 7 events for cut 4. remained. This corresponds to a fraction of $0.24 \pm 0.09\%$ of the selected events.

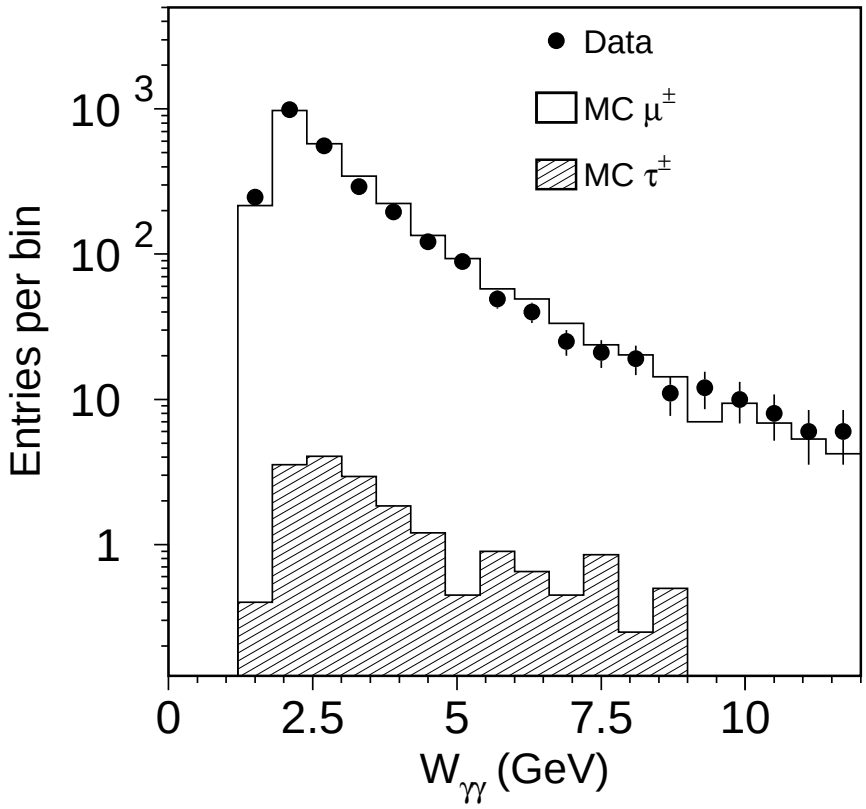

Figure 6.13: Background contribution due to $e^+e^- \to e^+e^-\tau^+\tau^-$. The τ-sample is normalized to the data luminosity.

6.4 Radiative Corrections

Another source, which has to be considered as background, but directly stems from the physical nature of the events under consideration, is final-state radiation (FSR):

$$e^+e^- \rightarrow e^+e^-\mu^+\mu^-(\gamma)$$

The production of single-tagged dimuon events from the multiperipheral contribution can be accompanied by photons as final-state radiation. This means that the highly scattered electron, which gives a tag-signature can be emitting a real photon in the final state. This topology will change the production cross-section and is not included in the formalism of two-photon physics. In addition, the experimental identification of such events is very difficult, if not impossible, since the radiated photons are either scattered out of the acceptance of the detector or will be detected together with the tagged electron. However, for the latter case the resolution of the tagging detectors is in general not sufficient in order to separate the electron from the photon. This means that the tag will be seen as one event.

An extended version of the BDK-generator (see Sec. 3.2, [27]), which includes the effect of final-state radiation from multiperipheral production was used to estimate the contribution of the effects of photons. The event generation was

divided according to the different beam-energies for the different years and a comparison was made to estimate the fraction of radiative events w.r.t. the total number events, stemming from multiperipheral production. Figs. 6.14-6.18 show the relative contribution of radiative events to the important distributions for this analysis: for the invariant mass $W_{\mu\mu}$, the squared four-momentum transfer Q^2, and for the relative momentum transfer x. The ratio in the figures depicts the number of events with final-state radiation compared to the total number of events for the process $e^+e^- \rightarrow e^+e^-\mu^+\mu^-(\gamma)$. It is apparent that all contributions are well below 1% (on average 0.2%), and they can be considered negligible for this background estimation.

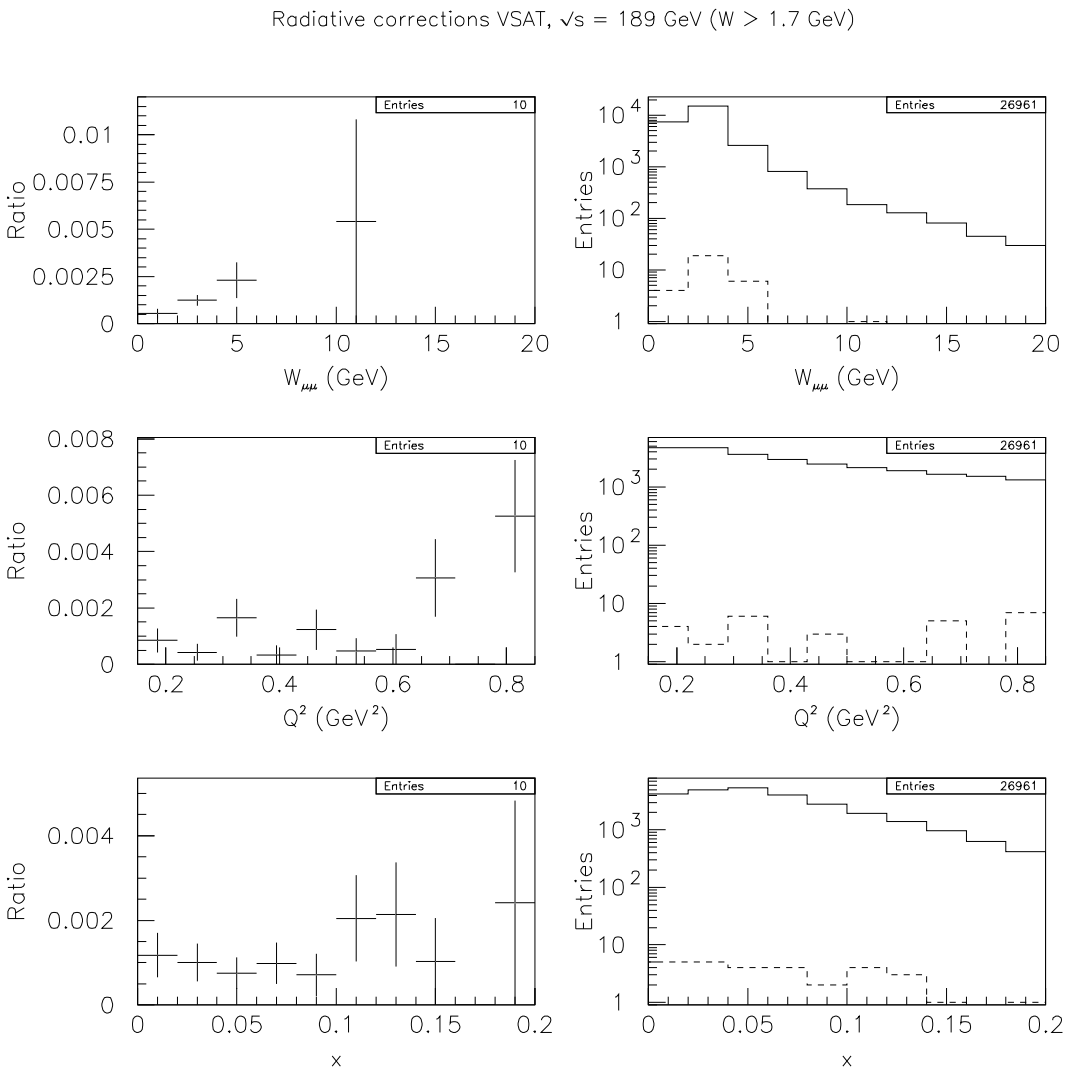

Figure 6.14: Radiative corrections for beam energy $\sqrt{s} = 189$ GeV.

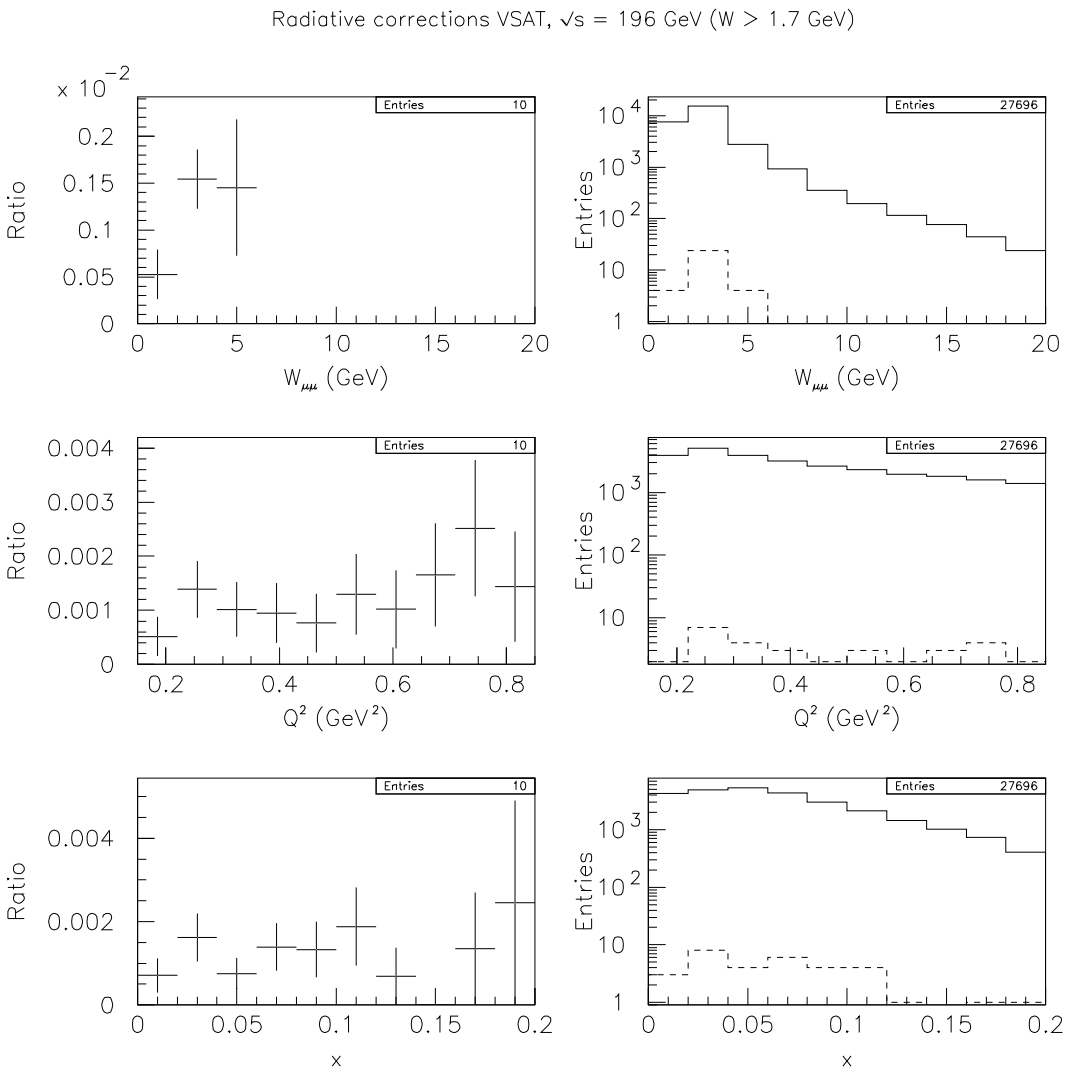

Figure 6.15: Radiative corrections for beam energy $\sqrt{s} = 196$ GeV.

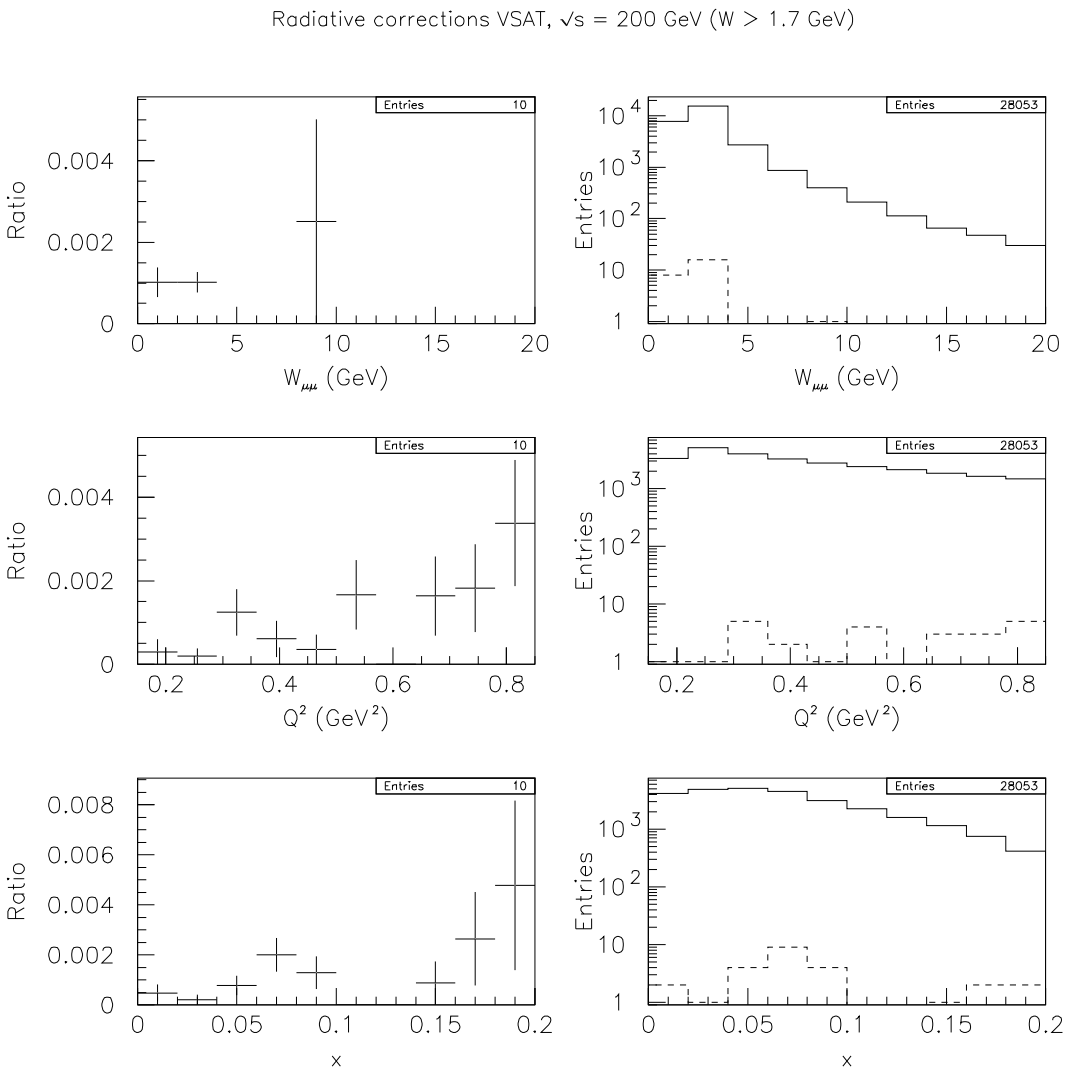

Figure 6.16: Radiative corrections for beam energy $\sqrt{s} = 200$ GeV.

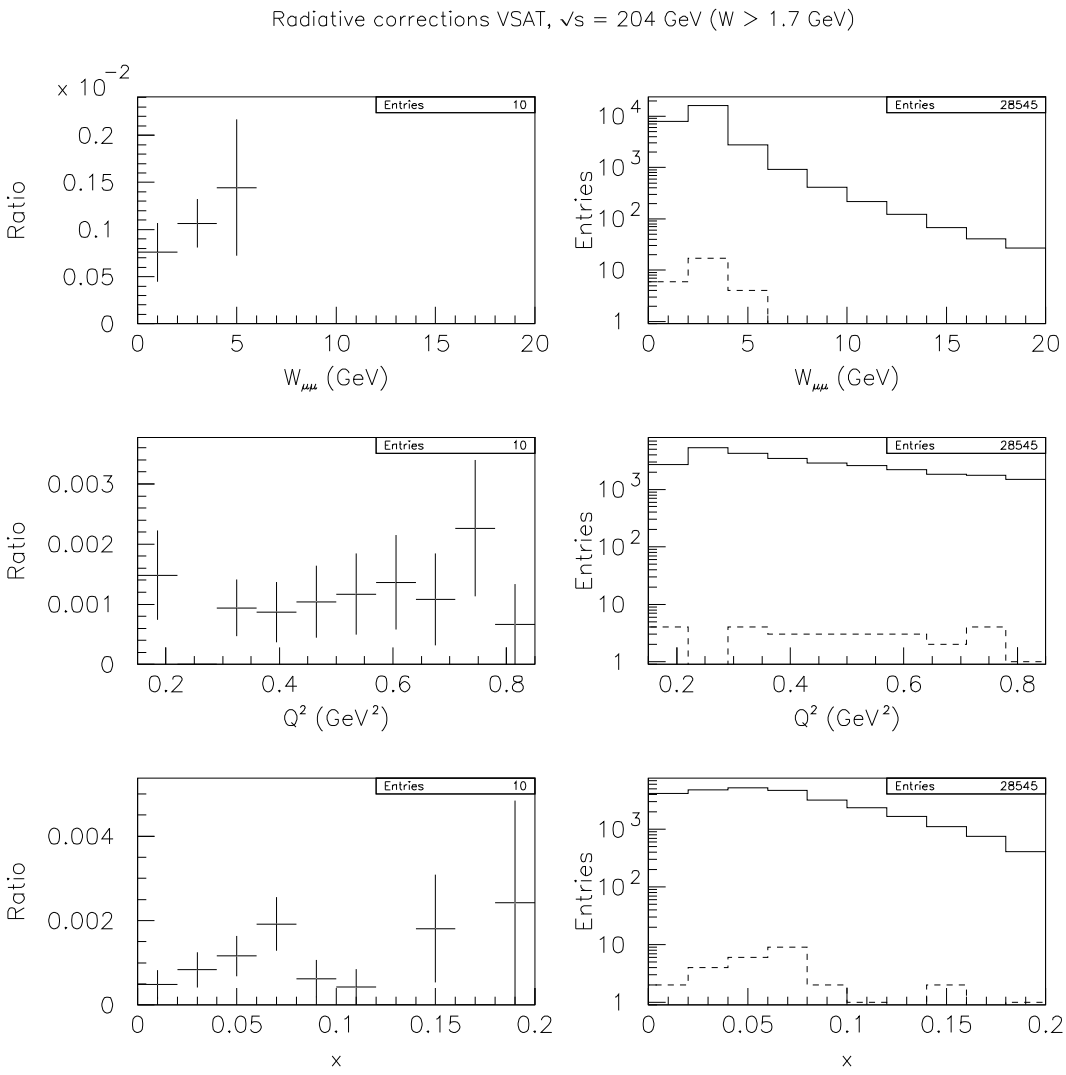

Figure 6.17: Radiative corrections for beam energy $\sqrt{s} = 204$ GeV.

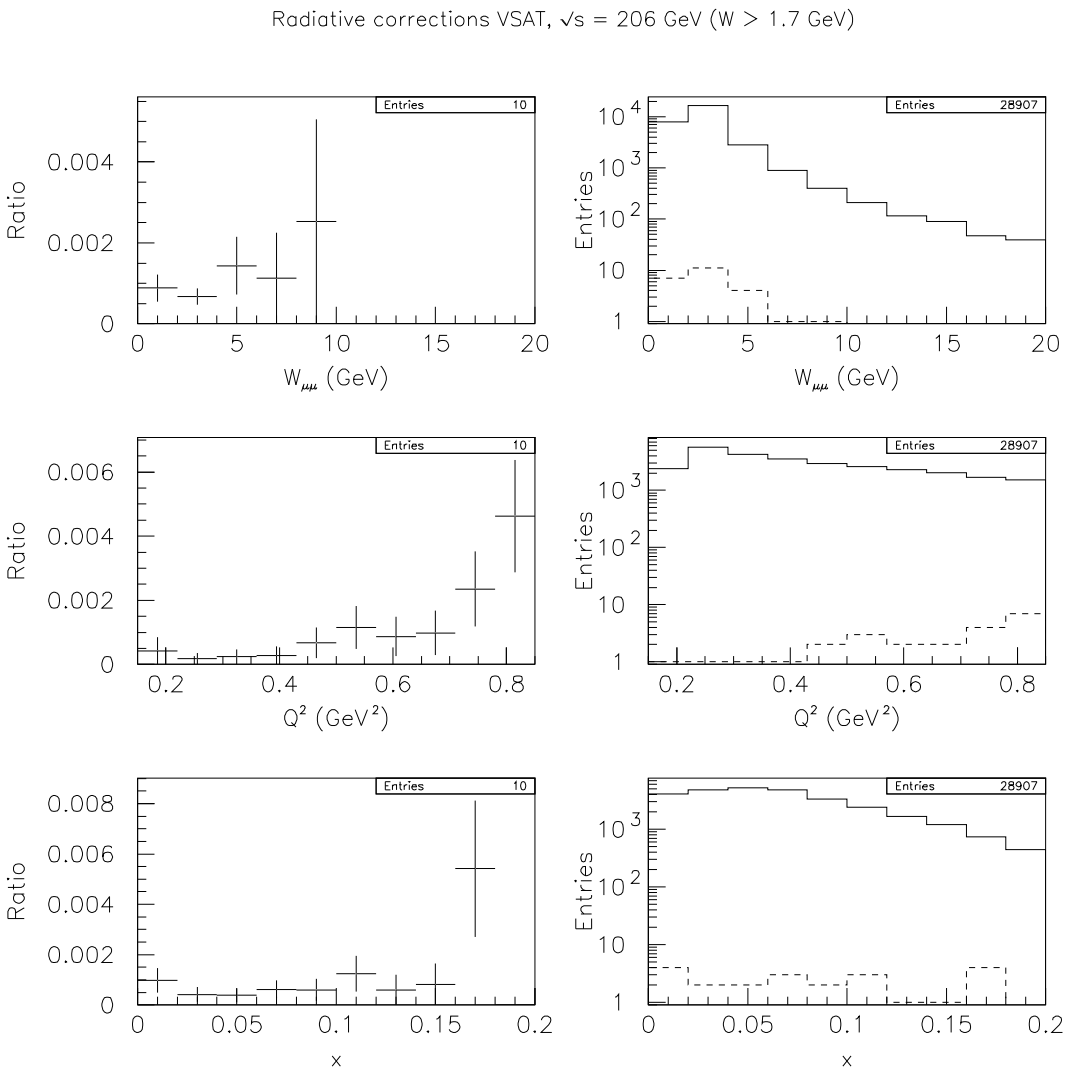

Figure 6.18: Radiative corrections for beam energy $\sqrt{s} = 206$ GeV.

6.5 Systematic Error Estimation

The ultimate goal of this analysis is the estimation of differential cross-sections. It is based on the selection of data events, which are prone to several sources of error. Statistical errors are well understood and can be easily included into the data analysis.

An additional source of error stems from systematic uncertainties. A systematic uncertainty can be in general defined as the uncertainty that makes results different from the true ones with reproducible discrepancies [21]. Systematic uncertainties must be obtained by means of analyzing experimental conditions and techniques.

The sources of systematic errors that might play a role in the present analysis stem from

1. The determination of luminosities, both for data and generated MC samples.

2. The background sources.

3. The trigger efficiencies.

4. The selection criteria.

5. The comparison between `VERMASEREN` and `GALUGA` generated events.

The luminosity measurements with the L3 detector were estimated to be precise within an averaged error margin of 0.06%.

The analysis and determination of the distributions is based on the comparison between data and generated/reconstructed MC events. The MC samples were produced with high statistics and had to be normalized to the luminosity of the data sample. The cross-sections of the generated `VERMASEREN` samples were estimated with an average uncertainty of 0.9%. Since the luminosity can be obtained with

$$\mathcal{L} = \frac{N_{generated}}{d\sigma},$$

the uncertainty of the cross-sections can be directly applied to the luminosity determination of the MC-sample.

The statistical error on the number of selected background events will contribute to a systematic error of the selected data events, after subtraction of the background events. This error was estimated to be 0.09%.

The subtraction of radiative events, which can be also considered as background introduced an additional systematic uncertainty. This uncertainty was estimated to be 0.2%.

The trigger efficiencies were estimated on the combinations of three trigger bits, which were accumulating events. As described in Sec. 6.2, the uncertainty was estimated to be 0.1%.

The event selection procedure, as described in Sec. 6.1 is not necessarily the ultimate tool to select events. The procedure is based upon the physical requirements for the events under consideration and are subject to errors due to resolution effects of the detector. This must be considered as a contribution to the systematic error in the measurement. The variation of a measured value, observed by varying the selection cuts, can be used to identify a systematic error associated with the selection procedure. To estimate these systematic errors, the relative variation of the ratio $R = N^{Data}/N^{MC}$ as a function of the magnitude of a given selection cut can be studied. The procedure is to vary the selection cut by a certain amount and investigate the ratio

$$\frac{\Delta R}{R_0} \pm \delta\left(\frac{\Delta R}{R_0}\right) = \frac{R_i - R_0}{R_0} \pm \delta\left(\frac{\Delta R}{R_0}\right) \tag{6.5}$$

with

$$\delta\left(\frac{\Delta R}{R_0}\right) = \frac{\sqrt{|N_0 - N_i|}}{N_0}$$

The quantity R_0 corresponds to the ratio at the nominal cuts, with N_0 selected events, and the index "i" corresponds to the values when varying the selection cuts.

The leading selection cuts were varied by $\pm 5\%$ around their nominal cut. Figs. 6.19, 6.20 show the effect of these variations. The variation of the selection cuts other than the above mentioned, for instance Q^2 see Fig. 6.21, had only a minor

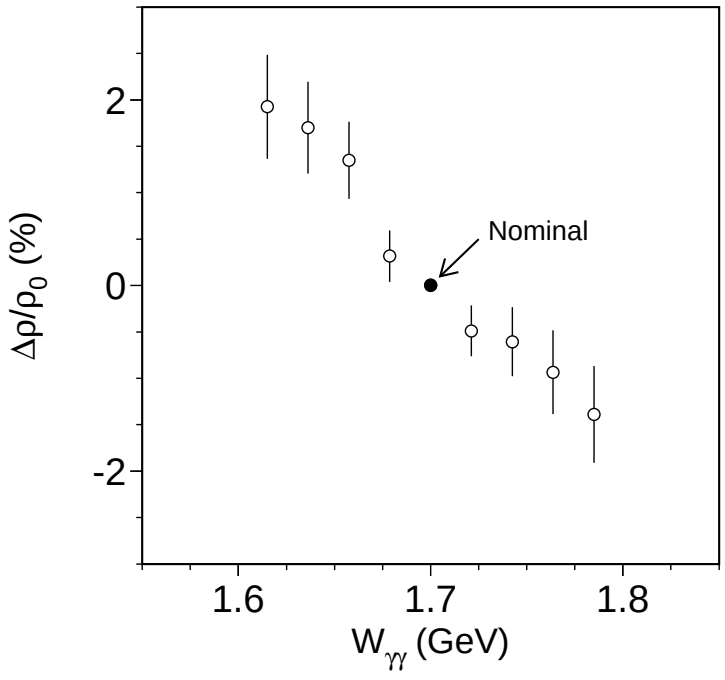

Figure 6.19: Variation of the invariant mass W and its influence on the number of selected events.

influence on the change of the ratio $\Delta R/R_0$. The systematic uncertainty of the leading cut variations was estimated to be 2.36%.

A further systematic uncertainty was obtained due to the comparison between the generated distribution with `GALUGA` and `VERMASEREN` (see Sec. 7.2). Since the evaluation of the cross-section and the structure function F_2 is based upon an estimation of the maximum polar angle of the untagged electron, the differences between the two generators will contribute to the systematic uncertainty

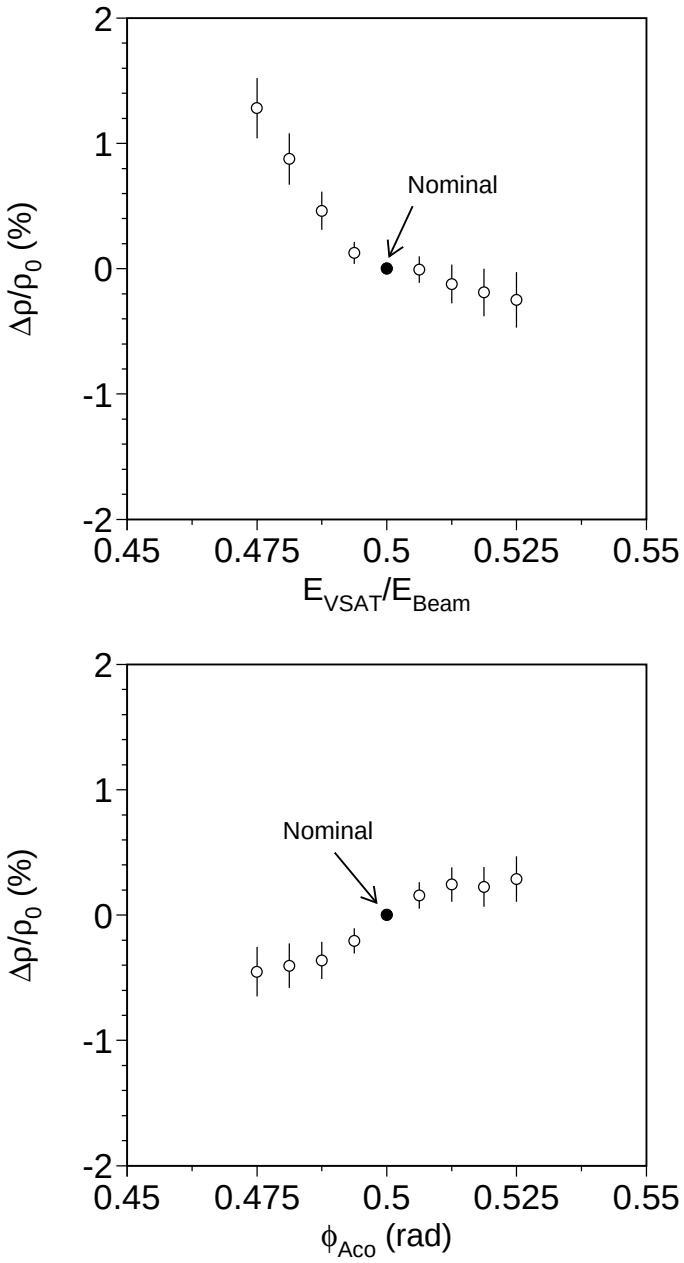

Figure 6.20: Upper: Variation of the tag-energy for VSAT, relative to the beam energy; lower: variation of the acoplanarity angle, and their influence on the number of selected events.

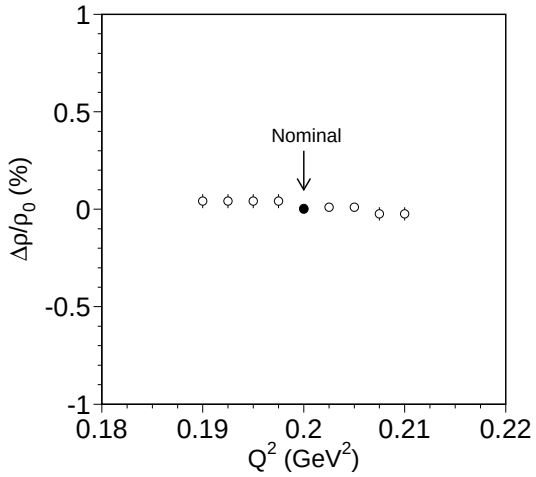

Figure 6.21: Variation of the squared four-momentum transfer and its influence on the number of selected events.

of the measurements and was estimated to be 2.16%.

The estimation of the individual systematic errors gives the estimation of an overall systematic error in the measurement. The overall systematic error calculates as $\epsilon = \sqrt{\Sigma_i \epsilon_i^2}$, where the index i runs over all individual error sources. This leads to a total systematic error of 3.3%. A summary of the systematic uncertainties are shown in Tab. 6.3.

Error source	Error contribution (in %)
Luminosity Data	0.06
Luminosity MC	0.90
Background	0.09
Radiative events	0.20
Trigger efficiency	0.12
Selection criteria	2.36
GALUGA	2.16
Total	3.33

Table 6.3: Sources of systematic uncertainties for the estimation of cross-sections and their contribution to the total systematic error.

6.6 Summary

Data were selected with the L3 detector in the years 1998-2000, at c.m.s. energies of $\sqrt{s}$ = 189 - 206 GeV and with an integrated luminosity of $\mathcal{L}$ = 600.2 pb^{-1}. The data were compared to a MC sample, which was produced with the `VERMASEREN` generator. The reconstructed MC sample was treated in the same way as for the data, so that a direct comparison was applicable. The data were corrected for trigger inefficiencies, whereas the MC sample a full trigger efficiency of 100%.

Process	Selected events from data	Expected events from MC	Ratio	Expected Background	Systematic Uncertainty
$ee \to ee\mu\mu$	2817±53	2819±53	0.999	0.30%	3.33%

Table 6.4: Selection results after all applied cuts. The trigger efficiency ε = 96.5% was taken into account for data.

The selection of single tagged dimuon events leads to distributions of events for data as well as reconstructed MC events, which agreed, in shapes as well as in

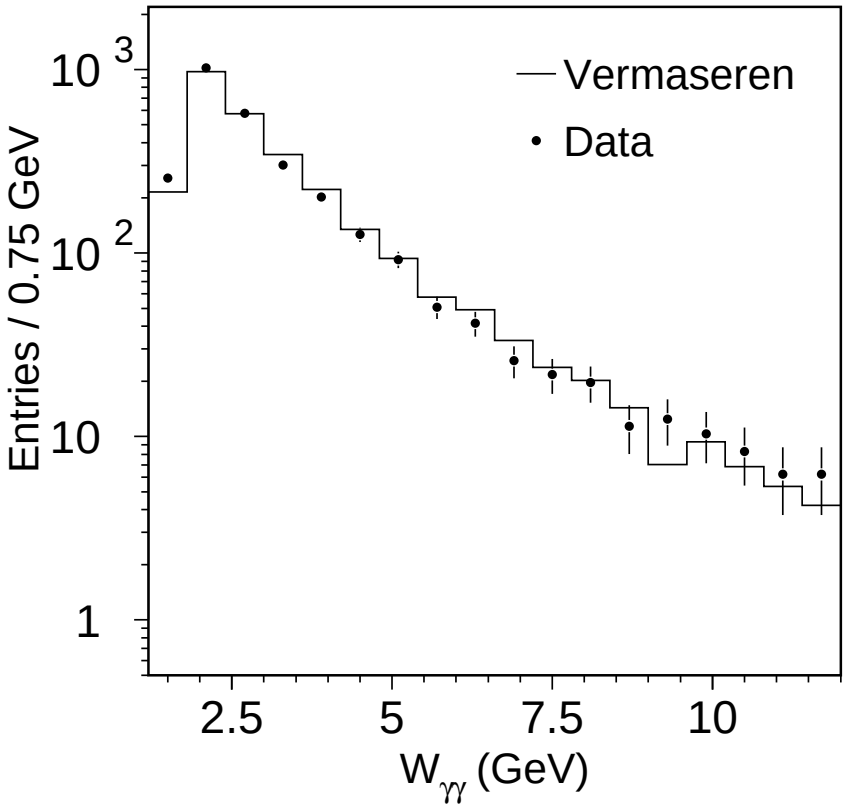

Figure 6.22: Invariant mass of the two muons in the final state.

total numbers and can be seen in Figs. 6.22, 6.23, and 6.24, as well as from Tab. 6.4. Slight discrepancies can be seen for low invariant masses $W_{\gamma\gamma}$ in Fig. 6.22: at low masses the contribution of background events, e.g. two-pions may be still present; the Q^2-distribution for experimental data (Fig. 6.23) shows a narrower peak as compared to MC data. This might be explained with the usage of the tracks for the dimuon event. The squared four-momentum transfer is

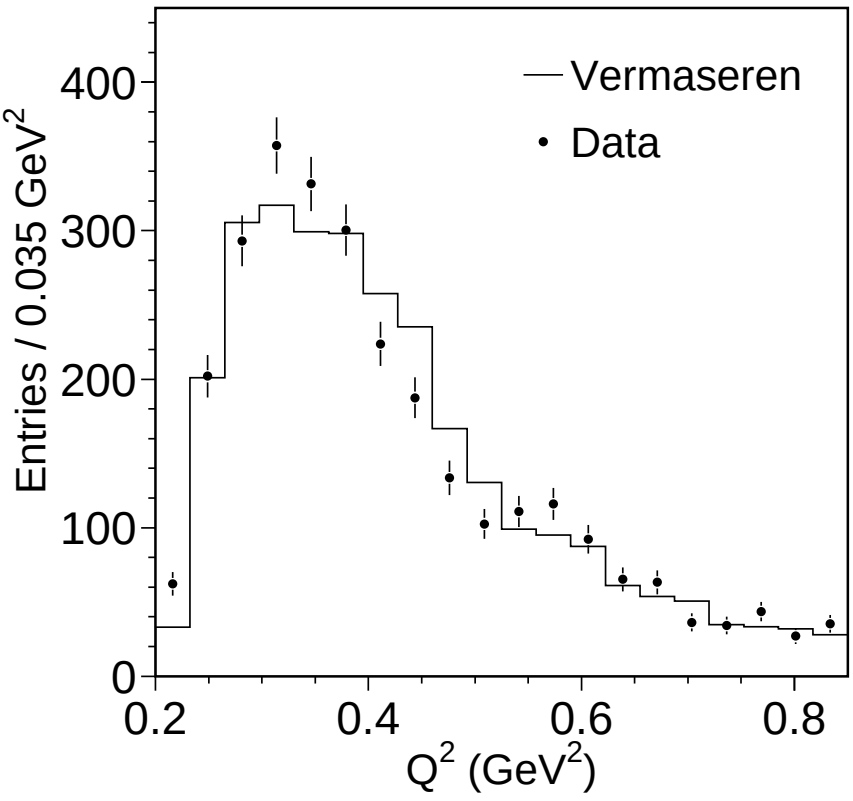

Figure 6.23: Squared four-momentum transfer to the highly virtual photon.

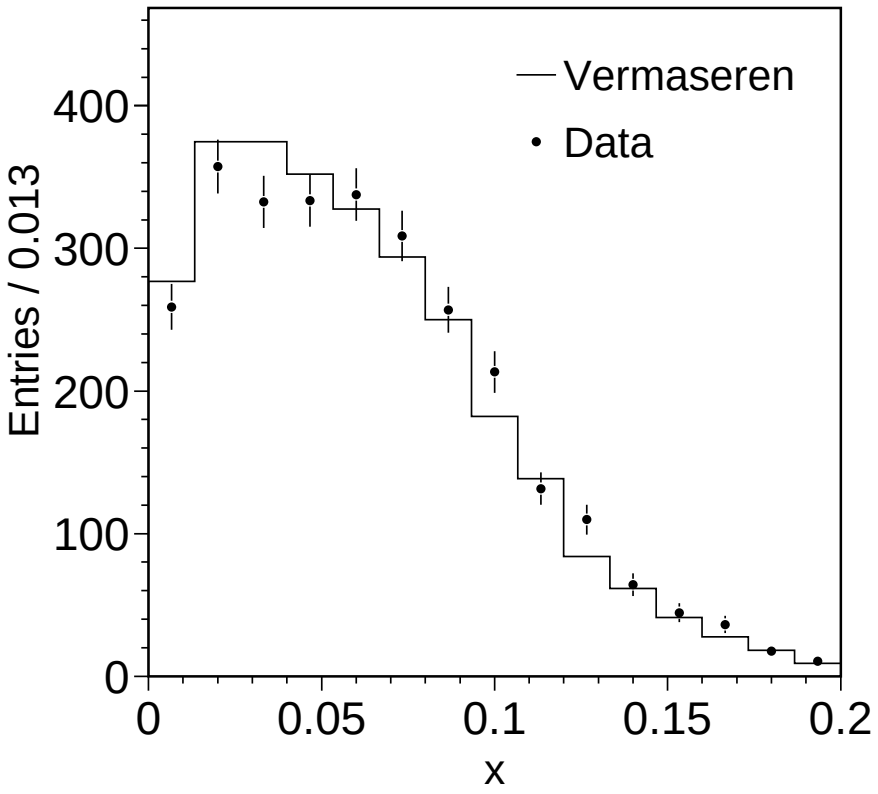

Figure 6.24: Fraction of momentum of the highly virtual photon.

determined with $Q^2 = (\vec{p}_{T,1} + \vec{p}_{T,2})^2$. The reconstructed momenta of the tracks are slightly different as compared to data, however, still within statistical limits: the depicted MC distribution can be assigned similar error bars as seen from data.

The distributions of interest are for $W_{\mu\mu}$ and for Q^2, which can be accessed directly from data. The distribution for the relative momentum fraction x, which can be derived from $W_{\mu\mu}$ and from Q^2 is the variable of interest in order to determine the structure function F_2^γ.

Chapter 7

Results

The physics topic of interest for this work is the determination of the differential cross-section $d\sigma/dQ^2$ for the production of dimuons stemming from two-photon collisions. Furthermore, the interest is second the determination of the double differential cross-section, $d^2\sigma/dQ^2dx$, which can be used to investigate the structure of photons by means of the structure function F_2^γ.

Since the underlying theoretical physical description is based on QED, one can use mostly analytical predictions to compare the results with theoretical expectations.

7.1 The Differential Cross-Section $d\sigma/dQ^2$

Starting in the early 1970's [8], the measurement of the differential cross-section $d\sigma/dQ^2$ of dimuon production in tagged $\gamma\gamma$ collisions was the focus of several experiments, see e.g. [16, 51, 52, 53, 54]. The experiments were determining the differential cross-section over a wide kinematic range. The measurement is essential for defining the quality of selection procedures and the feasibility of applying the procedures to a different field in physics, namely QCD.

The data selection was the first step on the way to determine the differential cross-sections. The second step included background subtraction and applying trigger efficiency procedures on the selected data sample. A further step is necessary in order to extract quantities from the data sample that can be compared with theoretical predictions.

Theoretical descriptions are MC samples by means of generating events according to certain cross-sections. On the generator level one does not account for detector effects. These effects can be mainly described by limited detection acceptances and efficiencies. Data have to be corrected for these effects and are then ready to be used for calculating the quantities of interest.

The procedure, which was used, is to compare the reconstructed MC-sample after selections and compare them to the MC sample on the generator level.

This allows to estimate and correct for the above mentioned effects according to

$$\frac{d\sigma}{dQ^2} = \frac{N_{data}}{\Delta Q^2 \cdot \mathcal{A} \cdot \varepsilon \cdot \mathcal{L}} \tag{7.1}$$

The quantities in (7.1) are

- $\mathcal{A}$: the geometrical acceptance of the detector complex. It is defined by the ratio of the MC distribution, which can be in principle detected by the detector complex, to the MC sample at the generator level.

- ε: the detector and selection efficiency, which can be defined as the ratio of the MC sample, selected according to the selection criteria, to the full MC sample in the reconstructed stage.

- $\mathcal{L}$: the integrated luminosity of the data sample.

One difficulty arises from the determination of the geometrical acceptance $\mathcal{A}$. It is necessary to have a precise knowledge of the geometrical parameters of the detector complex. This difficulty can be circumvented if one considers a convolution of $\mathcal{A}$ and the detector and selection efficiency ε. This is reasonable, since on the level of reconstruction all the needed information are already included in the appropriate software packages, like `GEANT` and `GEISHA`. The correction factor can then be obtained by using the ratio of the distribution, as selected in the same way as the final data set, to the distribution on the generator level.

The theoretical prediction was calculated with the MC generator GALUGA. A series of differential cross-sections $d\sigma/dQ^2$ was calculated for a subdivision of Q^2-ranges within the range $0.2\,GeV^2 \leq Q^2 \leq 0.85\,GeV^2$. The crucial parameter used in GALUGA was the maximum polar angular range, in which the untagged electron can be scattered. This angle was determined as described in Sec. 7.2. Fig. 7.1 shows a good agreement between data and the QED prediction (see also Tab. 7.1). The average Q^2 (center of gravity: c.o.g.) for each bin was calculated and the data points are depicted accordingly.

$< Q^2 >$ (GeV^2)	$d\sigma/dQ^2$ (nb/GeV^2)	σ_{stat} (nb/GeV^2)	σ_{syst} (nb/GeV^2)	σ_{tot} (nb/GeV^2)
0.257	6.467	0.279	0.215	0.352
0.324	4.102	0.219	0.137	0.258
0.375	3.178	0.179	0.106	0.208
0.423	2.355	0.145	0.078	0.165
0.473	1.787	0.127	0.060	0.141
0.543	1.566	0.087	0.052	0.101
0.646	1.069	0.079	0.036	0.087
0.771	0.702	0.057	0.023	0.062

Table 7.1: Measured differential cross-section as a function of Q^2 and estimated uncertainties.

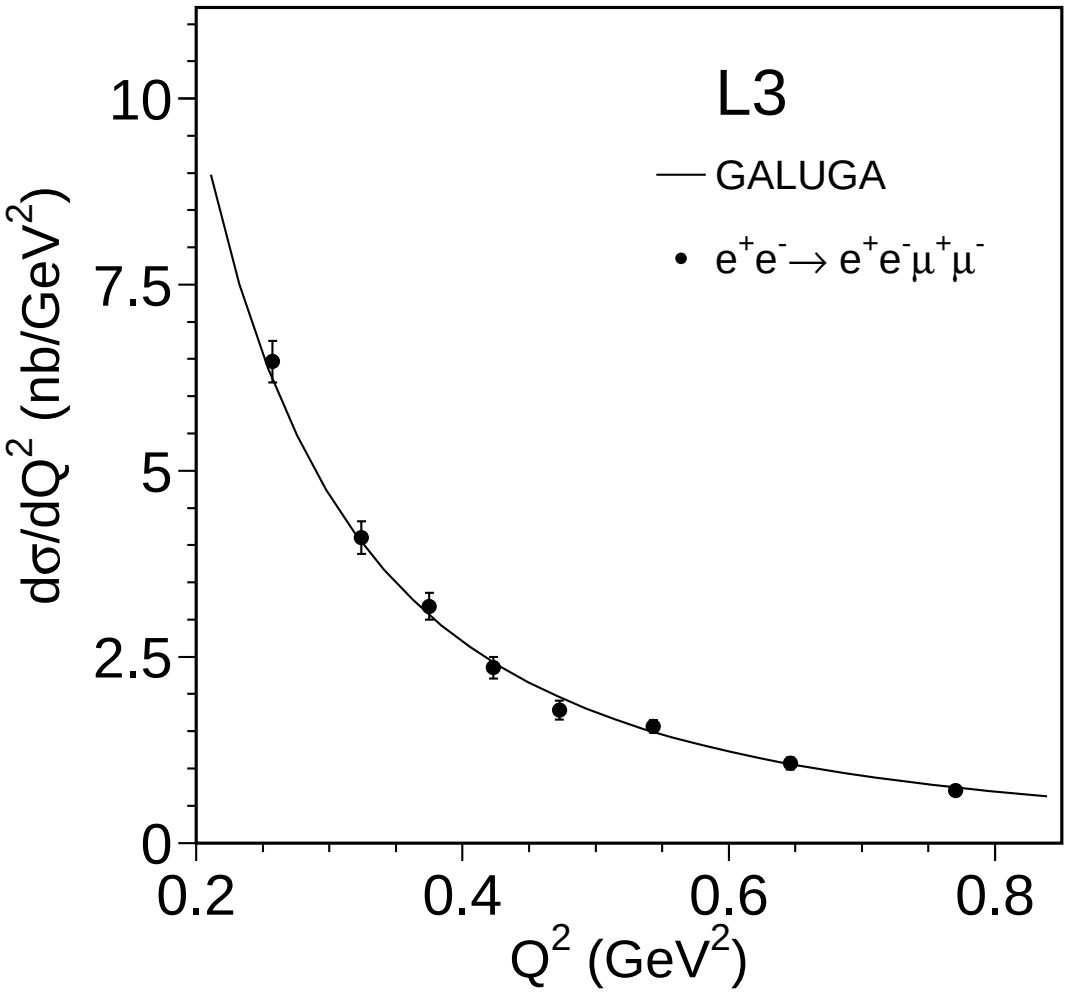

Figure 7.1: The differential cross-section as a function of Q^2 from the reaction $e^+e^- \rightarrow e^+e^-\mu^+\mu^-$. The QED curve has been obtained with the generator `GALUGA`. Only statistical errors are drawn.

7.2 The Structure Function F_2^γ

The parameter x, which the structure function depends upon, is limited in its maximum to $x = 0.2$ (Fig. 6.24). This stems from the fact that the Q^2-range for the single-tagged events with VSAT is very small in magnitude ($0.2\,GeV^2 \leq Q^2 \leq 0.85\,GeV^2$) and the invariant mass $W_{\mu\mu}$ is limited in its minimum to $1.7\,GeV \leq W_{\mu\mu}$. The Bjorken-x is obtained via $x = \frac{Q^2}{Q^2+W_{\mu\mu}^2}$. Consequently, larger x are not accessible for this analysis.

The procedure to extract the structure function F_2^γ from data can be seen from Eq. (2.22). In order to get the proper working points for `GALUGA`, the crucial parameter for this generator in form of the maximum polar angle for the unscattered electron θ_{unt} has to be determined. This angle was determined with a χ^2-minimization procedure (least-mean-square fit) for the difference in magnitude, between the cross-sections as calculated with the `VERMASEREN` generator and `GALUGA`:

$$\chi^2 = \Sigma_i \frac{s_i - \bar{s}_i}{\sigma_i}\,, \tag{7.2}$$

where s_i corresponds to the cross-section for different bins x_i and $\bar{s}_i$ was taken as the value of the cross-section for each bin from `VERMASEREN`. The quantity σ_i is the statistical uncertainty in each bin from `GALUGA`, i.e. plays the role of a weight and can be reduced by increasing the number of events in the event

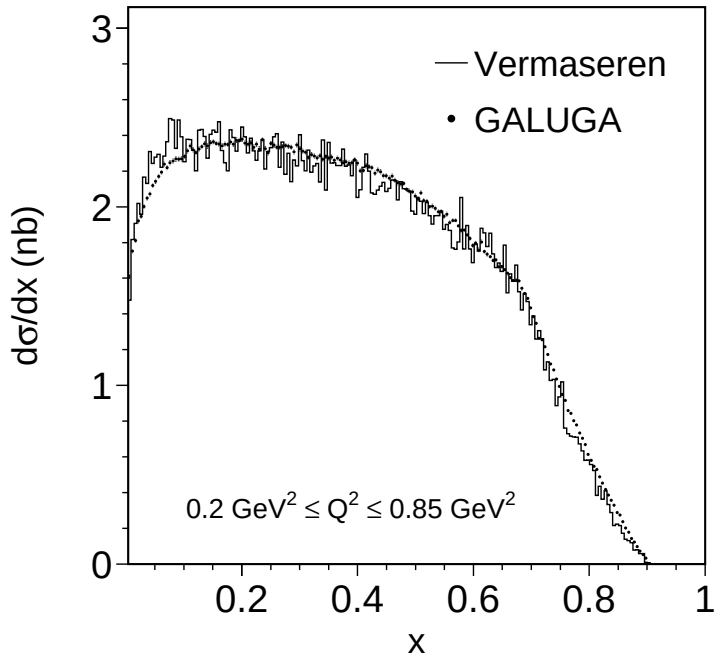

Figure 7.2: The differential cross-section as a function of x, generated with the `VERMASEREN` and the `GALUGA` generator.

production. The distributions between the two generated MC samples are in good agreement as can be seen in Fig. 7.2.

The measured structure function F_2^γ can be seen in Fig. 7.4 and in Tab. 7.2. The average values for the x-bins were calculated and are depicted as their c.o.g. in Fig. 7.4. There is a good agreement between the data and the prediction, based on Eq. (2.7). The structure function is suppressed as compared to non-vanishing virtualities of the probe photon. Although the effect of a non-zero

virtuality of the target photon is not very significant at low x, the data suggest that $P^2 > 0\,GeV^2$. The average value of $P^2 = 0.031 \pm 0.001\,GeV^2$ was obtained from a χ^2-fit procedure as described above (Eq. (7.2)). However, the confidence level for the obtained value is very low, $P \sim 2 \times 10^{-9}$. The result of the χ^2-fit can be seen in Fig. 7.3.

A mean value of $P^2 = 0.019 \pm 0.001\,GeV^2$ was obtained from the reconstructed MC sample.

The total systematic uncertainty was determined to be $\sigma_{sys} = 3.3\%$. In conjunction with reasonable statistical errors, this work depicts a precise measurement of the differential cross section $d\sigma/dQ^2$ in the range $0.2\,GeV^2 \leq Q^2 \leq 0.85\,GeV^2$, as well as the leptonic structure function $F^{\gamma}_{2,QED}(x, Q^2)$ in the range $0 < x \leq 0.2$.

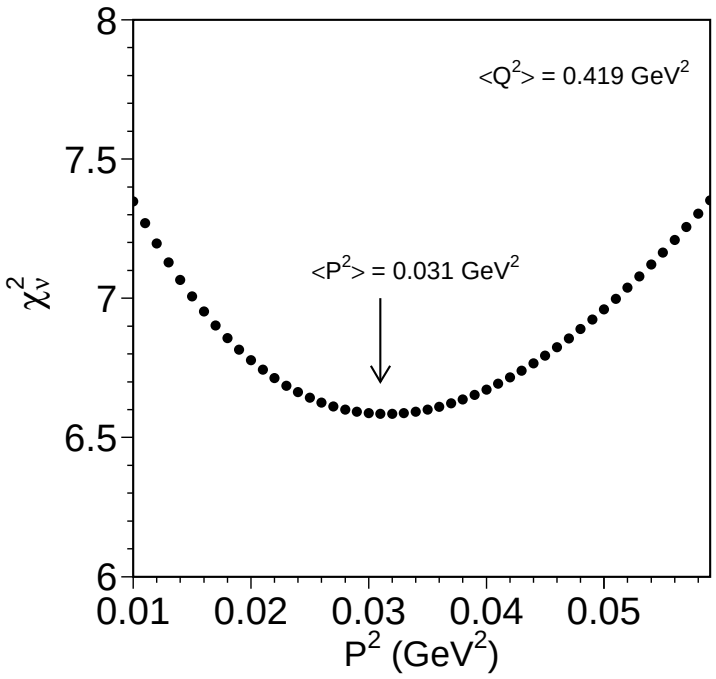

Figure 7.3: Least-mean-square fit for obtaining the average P^2 for the structure function F_2^γ. The value at the vertical axis depicts the reduced χ^2, i.e. χ^2/n_{dof}.

$< Q^2 > (GeV^2)$	$< x >$	$F^{\gamma}_{2,QED}/\alpha$	σ_{stat}	σ_{syst}	σ_{tot}
0.4190	0.0046	0.0088	0.0009	0.0003	0.0010
	0.0099	0.0198	0.0018	0.0007	0.0019
	0.0187	0.0300	0.0017	0.0010	0.0020
	0.0295	0.0443	0.0028	0.0015	0.0032
	0.0401	0.0590	0.0036	0.0020	0.0041
	0.0521	0.0777	0.0042	0.0026	0.0049
	0.0666	0.0972	0.0054	0.0032	0.0063
	0.0867	0.1291	0.0076	0.0043	0.0087
	0.1135	0.1523	0.0072	0.0051	0.0088
	0.1542	0.1796	0.0123	0.0060	0.0137

Table 7.2: Measured leptonic structure function as a function of x with a mean squared four momentum transfer of the untagged electron $< P^2 >= 0.019\, GeV^2$, and estimated uncertainties.

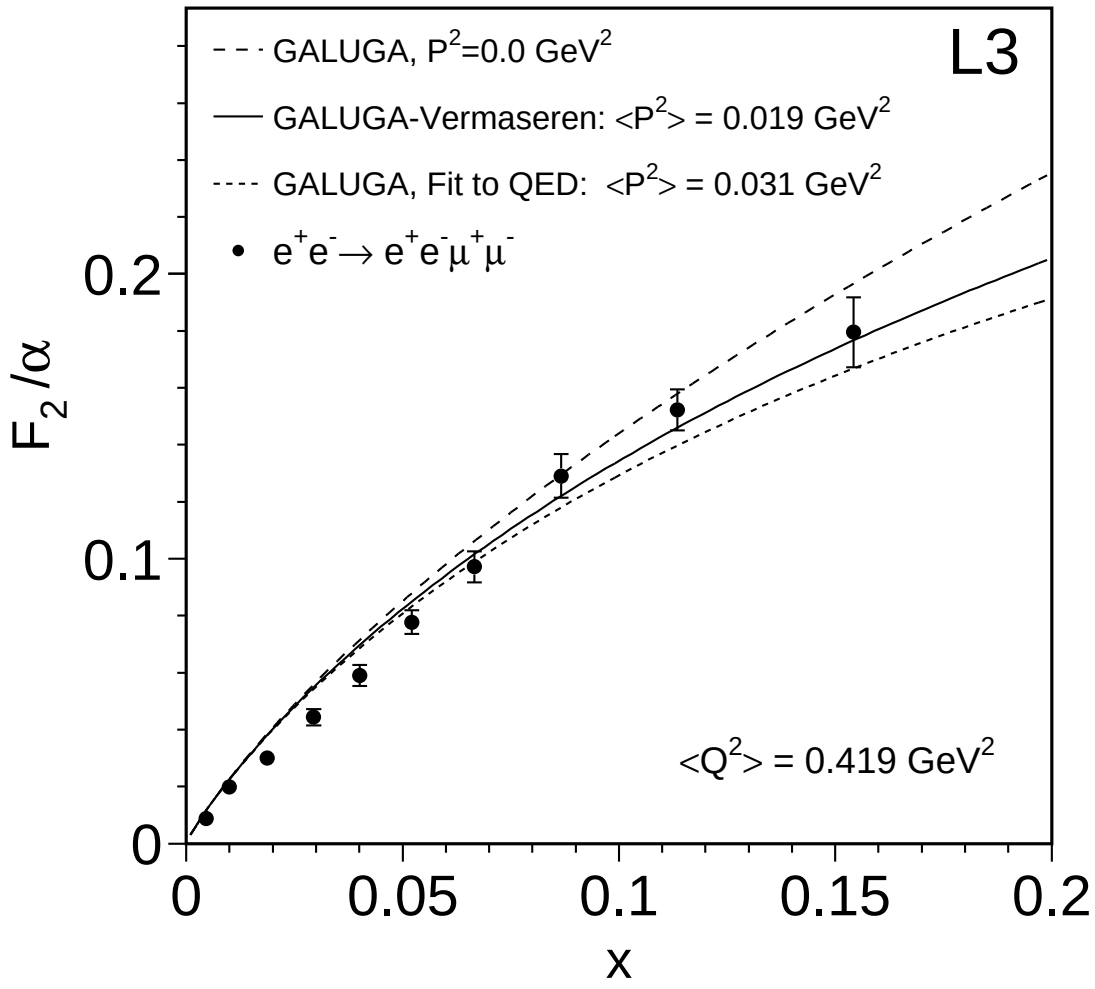

Figure 7.4: The structure function F_2^γ as a function of x from the reaction $e^+e^- \to e^+e^-\mu^+\mu^-$. The QED curves have been obtained with Eq. (2.7) and a mean virtuality of $P^2 = 0\,GeV^2$ (dashed line), $P^2 = 0.019\,GeV^2$ (solid line, MC), and $P^2 = 0.031\,GeV^2$ (dotted line, fit) for the target photon, respectively. The data suggest that a non-zero virtuality should be used. Only statistical errors are drawn.

Chapter 8

Conclusion

A data set, taken with the L3 detector at the Large Electron Positron Collider LEP, between the years 1998 and 2000 was analyzed according to the reaction $e^+e^- \rightarrow e^+e^-\gamma^*\gamma^* \rightarrow e^+e^-\mu^+\mu^-$, which is a QED process of the order $\mathcal{O}(\alpha^4)$. The data sample corresponded to an integrated luminosity of $\mathcal{L} = 600.2\,pb^{-1}$, with different beam energies in the range $189\,GeV \leq \sqrt{s} \leq 206\,GeV$.

For the first time, a measurement in the very low kinematic region $0.2\,GeV^2 \leq Q^2 \leq 0.85\,GeV^2$ of this channel was performed, in conjunction with the very high beam energies, provided by LEP.

The measurement of the differential cross-section $d\sigma/dQ^2$ was performed and good agreement between data and the QED prediction was found. The measurement improves on up-to-date measurements of this cross-section from other

experiments.

In addition, the differential cross-section $d^2\sigma/dxdQ^2$ was measured and the leptonic structure function $F^{\gamma}_{2,QED}$ was extracted from this measurement. The measurement was restricted to a maximum value of the Bjorken-x of $x = 0.2$ due to the low region of the squared four-momentum transfer and a limited accessibility of the invariant masses of the dimuon-system, $1.7\,GeV \leq W_{\mu\mu}$ in this measurement.

However, conversely the limitation allowed a detailed measurement of the structure function, down to very low values in x.

The measurement of the structure function $F^{\gamma}_{2,QED}$ shows good agreement if the squared four-momentum transfer P^2 to the probe photon is not assumed to be vanishing. It was found, that an average virtuality of $P^2 = 0.019 \pm 0.001\,GeV^2$ describes the data. This non-zero virtuality is an established fact, investigated with earlier measurements. This measurement supports this statement down to very low Q^2.

A compilation of several measurements, with different experiments and at different Q^2-ranges can be seen in Fig. 8.1. For comparison, the measurement of the structure function $F^{\gamma}_{2,QED}$ from this work is shown at the top.

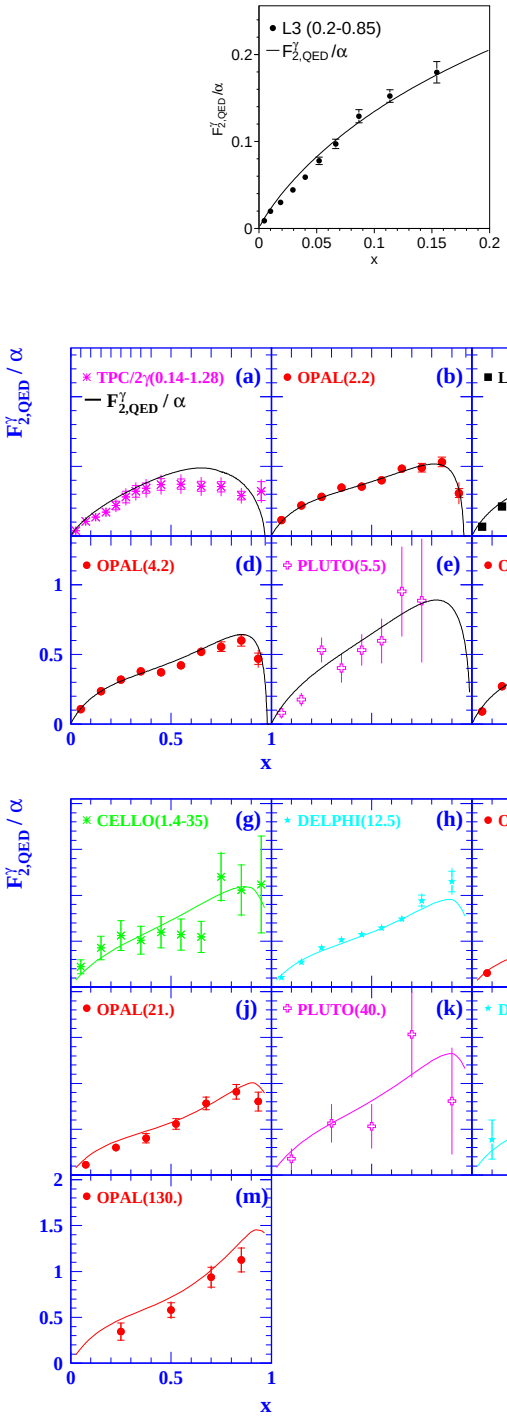

Figure 8.1: Compilation of measurements of the leptonic structure function $F^{\gamma}_{2,QED}$ as a function of x, for different Q^2 ranges [55].

Bibliography

[1] L.D. Landau and E.M. Lifshitz. Sov. Phys. **6** (1934) 244.

[2] V.M. Budnev, I.F. Ginzburg, G.V. Meledin and V.G. Serbo. Phys. Lett. **39B** (1972) 526; Nucl. Phys. **63B** (1973) 519.

[3] P. Achard et al. Phys. Lett. **623B** (2005) 26.

[4] G. Abbiendi et al. Eur. Phys. J. C.**45** (2006) 1.

[5] R.P. Feynman, Notes taken by A.R. Hibbs. "Quantum Electrodynamics: A Lecture Note and Reprint Volume." Frontiers in Physics, A Lecture Note and Reprint Series. W. A. Benjamin, Inc., New York 1962

[6] F. Halzen, A.D. Martin. Quarks & Leptons: "An Introductory Course in Modern Particle Physics." John Wiley & Sons, Inc., 1984.

[7] P. Schmüser. "Feynman-Graphen und Eichtheorien für Experimentalphysiker." Springer Verlag, 1995 (in German).

[8] V.E. Balakin et al. Phys. Lett. **34B** (1971) 663.

[9] G. Susinno. Internal Report, L3 note 2193, 1997.

[10] J.H. Field. "Lecture Notes in Physics: Photon Photon Collisions", v. **191** (1983) 270.

[11] M. R. Whalley. J. Phys. G: Nucl. Part. Phys. **27** A1, 2001.

[12] M. Krawczyk, M. Staszel, A. Zembrzuski. Phys. Rep. **345** (2001) 265.

[13] V.M. Budnev, I.F. Ginzburg, G.V. Meledin and V.G. Serbo. Phys. Rep. **15**, (1975) 181.

[14] Ch. Berger and W. Wagner. Phys. Rep. **146**, (1987) 1.

[15] J.D. Bjorken. Phys. Rev. **163** (1967) 1767.

[16] H. Behrend et al. Phys. Lett. **126B** (1983) 384.

[17] K. Wille. "Physik der Teilchenbeschleuniger in Synchrotronstrahlungsquellen." Stuttgart: Teubner 1992 (in German).

[18] G. Montagna, O. Nicrosini and F. Piccinini. "Precision Physics at LEP." Rivista del Nuovo Cimento **21** n. 9 (1998) 1.

[19] G. A. Schuler. Comp. Phys. Comm. **108** (1998) 279.

[20] G. Cowan. "Statistical Data Analysis." Oxford University Press Inc., 1998.

[21] P.R. Bevington, D.K. Robinson. "Data Reduction and Error Analysis for the Physical Sciences." 3rd Ed., The McGraw-Hill Companies, Inc., 2003.

[22] S. Jadach. "Practical Guide to Monte Carlo." eprint arXiv:physics/9906056, 1999.

[23] J.A.M. Vermaseren. Nucl. Phys. **B229** (1983) 347.

[24] G.P. Lepage. J. Comp. Phys. **27** (1978) 192.

[25] F.A. Berends, P.H. Daverfeldt and R. Kleiss. Nucl. Phys. **B253** (1985) 441;Comp. Phys. Comm. **40** (1986) 285.

[26] F.A. Berends, P.H. Daverfeldt and R. Kleiss. Comp. Phys. Comm. **40** (1986) 309.

[27] F.A. Berends, P.H. Daverfeldt and R. Kleiss. Nucl. Phys. **B253** (1985) 421;Comp. Phys. Comm. **40** (1986) 271.

[28] R. Brun et al. GEANT 3.21 preprint CERN DD/EE/84-1 (1984), revised 1987.

[29] H. Fesefeldt. RWTH Aachen report PITHA 85/2 (1985).

[30] J. Adams. Annual Report to the CERN Council, 1979.

[31] D. Decamp et al. Nucl. Inst. Meth. **A294** (1990) 121.

[32] P. Abreu et al. Nucl. Inst. Meth. **A303** (1991) 233.

[33] B. Adeva et al. Nucl. Inst. Meth. **A289** (1990) 35.

[34] K. Ahmet et al. Nucl. Inst. Meth. **A305** (1991) 275.

[35] J. S. Kapustinsky et al. IEEE Trans. Nucl. Sci. **41** (1994) 772.

[36] M. Acciarri et al. Nucl. Inst. Meth. **A289** (1994) 300.

[37] F. Beissel et al. Nucl. Inst. and Meth. **A332** (1993) 33.

[38] A. H. Walenta. IEEE Trans. Nucl. Sci. NS. **26,1** (1979) 73.

[39] W. R. J. Wenninger. Internal Report, L3 note 766, 1990.

[40] U. Uwer. Internal Report, L3 note 1400, 1993.

[41] Yu. Galaktionov et al. Nucl. Inst. Meth. **A251** (1986) 258.

[42] A. Areiev et al. Nucl. Inst. Meth. **A285** (1989) 403.

[43] F. Filthaut, F. Linde, T. van Rhee. Internal Report, L3 note 2117, 1997.

[44] I. C. Brock et al. Nucl. Inst. Meth. **A381** (1996) 236.

[45] P. Bene, M. Bourquin, J. H. Field, G. Forconi, A. Leger, J. Perrier, N. Produit, and J-P. Richeux. Nucl. Instr. Meth. **A306** (1991) 150.

[46] Y. Bertsch et al. Nucl. Inst. Meth. **A340** (1994) 309.

[47] C. Dionisi et al. Nucl. Inst. Meth. **A336** (1993) 78.

[48] J. Swain, L. Taylor. "L3 Computing Guide." Preprint NUB-3065 (1993), Northeastern University Boston, Mass.,USA.

[49] R. Brun, O. Couet, N. Cremel, A. Nathaniel, A. Rademakers, C. Vandoni. "PAW Physics Analysis Workstation, User's guide." CERN Program Library entry Q121.

[50] H. Grote, I. McLaren. "EPIO Experimental Physics Input Output Package, User's guide." CERN Program Library entry I101.

[51] M. Acciarri et al. Phys. Lett. **B438** (1998) 363.

[52] M. Cain et al. Phys. Lett. **B147** (1984) 232.

[53] C. Berger et al. Z. Phys. **C27** (1985) 249.

[54] B. Adeva et al. Phys. Rev. **D38** (1988) 2665.

[55] R. Nisius. Physics Reports **332** (2000) 165.